Aalto University
School of Science
Degree Programme in Engineering Physics and Mathematics

Toni Mäkelä

Flavour-dependent jet energy corrections and top quark mass

Master's thesis
Espoo, May 24, 2019

Supervisor: Professor Mikko Alava
Advisors: Associate Professor Mikko Voutilainen,
M.Sc. (Tech.) Hannu Siikonen

Aalto University
School of Science
Degree Programme in Engineering Physics and Mathematics

ABSTRACT OF
MASTER'S THESIS

Author: Toni Mäkelä

Title:

Flavour-dependent jet energy corrections and top quark mass

Date:	May 24, 2019	**Pages:**	10+53
Major:	Engineering physics	**Code:**	SCI3056
Supervisor:	Prof. Mikko Alava		
Advisors:	Assoc. Prof. Mikko Voutilainen, M.Sc. (Tech.) Hannu Siikonen		

The top quark is the heaviest elementary particle in the standard model of particle physics. Its substantial mass indicates it may introduce significant corrections to the Higgs potential. Assuming no new physics below the Planck scale and that the interpretation of theory and measurements is right, these corrections and current experimental results imply that the electroweak vacuum lies in a metastable state. It is therefore important to examine how sound the measurements are.

The most accurate single measurements of the top quark mass m_t performed by the CMS and ATLAS collaborations at the LHC differ from a similarly precise result of the DØ experiment at the Tevatron by approximately 2.5 GeV. This amounts to almost 3 standard deviations, so that the DØ result lifts the world average top mass value to $m_t \approx 173.3$ GeV.

Since the top quark decays almost exclusively into a bottom quark b and a W boson, many top mass measurement channels depend on the reconstruction of b-jets, sprays of particles originating from bottom quarks. The very high accuracy of the DØ is based on a unique and very precise calibration of the flavour-dependent jet energy scale corrections. In particular, the DØ correction factor for b-jets is notably different from those used by the ATLAS, CDF and CMS collaborations. An accurate reproduction of the DØ b-jet energy scale corrections is performed using standalone Monte Carlo simulations. We investigate the sensitivity of the b-jet correction to various assumptions, suggest improvements to the method and discuss the results' implications to top mass measurements.

Keywords: Higgs, top, quark, flavour, jet, energy, scale, correction, calibration, Standard Model, DØ experiment

Language: English

Aalto-Yliopisto
Perustieteiden korkeakoulu
Teknillisen fysiikan ja matematiikan koulutusohjelma

DIPLOMITYÖN TIIVISTELMÄ

Tekijä: Toni Mäkelä

Työn nimi:
Makuriippuvat energiakorjaukset ja huippukvarkin massa

Päiväys:	Toukokuu 24, 2019	**Sivumäärä:**	10+53
Pääaine:	Teknillinen fysiikka	**Koodi:**	SCI3056
Valvoja:	Prof. Mikko Alava		
Ohjaaja:	Apul.prof. Mikko Voutilainen, DI Hannu Siikonen		

Huippukvarkki on hiukkasfysiikan standardimallin raskain alkeishiukkanen. Se saattaa suuren massansa vuoksi aiheuttaa huomattavia korjauksia Higgsin potentiaaliin. Mikäli Planckin skaalan alapuolella ei ole uutta fysiikka ja jos teoria ja kokeelliset tulokset on tulkittu oikein, nämä korjaukset ja mittausten maailmankeskiarvot kertovat sähköheikon tyhjiön olevan metastabiili. On siis tärkeää selvittää miten vakaalla pohjalla mittausmenetelmät ovat.

Tarkimmat yksittäiset LHC:n CMS ja ATLAS -kokeiden mittaukset huippukvarkin massalle eroavat noin 2.5 GeV vastaavaan tarkkuuteen yltäneen Tevatronin DØ kokeen tuloksesta. Tämä tarkoittaa melkein kolmea standardipoikkeamaa, joten DØ:n ansiosta maailmankeskiarvo nousee noin lukemaan 173.3 GeV.

Huippukvarkki hajoaa pääsääntöisesti b- eli pohjakvarkiksi ja W-bosoniksi. Useat huippukvarkin massan mittausmenetelmät vaativat b-jetin rekonstruointia, joka on pohjakvarkin hajoamistuotteista syntyvä hiukkassuihku. DØ:n suuri tarkkuus perustuu ainutlaatuiseen ja täsmälliseen jettien kvarkkimakuriippuvien energiaskaalakorjausten kalibrointiin. Erityisesti DØ:n b-jeteille käyttämä korjauskerroin eroaa huomattavasti ATLAS, CDF ja CMS -kokeiden menetelmistä. Toistamme DØ:n menetelmän täsmällisesti käyttäen riippumattomia Monte Carlo simulaatioita. Tutkimme b-jettien korjauskertoimen muutosherkkyyttä suhteessa tiettyihin oletuksiin, ehdotamme parannuksia käytettyihin menetelmiin ja käsittelemme tulosten vaikutusta huippukvarkin massamittauksiin.

Asiasanat: Higgs, huippu, kvarkki, maku, jetti, energia, korjaus, kalibraatio, standardimalli, DØ -koe

Kieli: Englanti

"We have to remember that what we observe is not nature itself, but nature exposed to our method of questioning."

–Werner Heisenberg

Foreword

I wish to thank associate professor Mikko Voutilainen for giving me the chance to work with his group at the Helsinki Institute of Physics and trusting me with such an important project. It was a privilege to receive the guidance of such a dedicated professor! I also thank M.Sc. (Tech.) Hannu Siikonen for all the advice, assistance and feedback that helped me in the shaping of this thesis and the analysis it describes. Further, I acknowledge Hannu's gen_handle software package, which served as the basis upon which I built my further analysis codes for the DØ studies presented herein. Thanks to Hannu as well for performing the top mass analysis on the basis of this work for a future publication. Performing both the jet energy corrections and a full top mass analysis in finite time would undoubtedly have been an insurmountable task for any single person. Thanks also to professor Mikko Alava of Aalto University for the supervision of this thesis and all the smooth cooperation.

I acknowledge and am very grateful for the help of the DØ veterans without whom the work would not have been possible. Most notably Liu Huanzhao, who provided me with the most relevant internal DØ analysis notes, and Andreas Jung along with Jan Stark for all the insight they provided as well as sharing their understanding of the DØ detector and methods. I would also like to thank all those taking interest in the progress.

As someone originating from a university of technology but becoming interested in high-energy physics, I have spent the last couple of years oscillating between the two campuses of Otaniemi and Kumpula. Therefore, I would like to thank the people making my study path possible in the first place. In particular, thanks to the lovely people coordinating the TFM study programme and prof. Adam Foster for granting the needed permissions along with prof. Alava. As is however evident by now, my two-level system eventually collapsed into having a desk at Helsinki for this thesis work. Hence, thanks to the fellow office inhabitants and other group members for the good times and company. In particular I thank Dr. Henning Kirschenmann who was also helping me out with some future directions.

There are also some academic people not involved with this thesis but who have lent me their guiding hand somewhere along the years. I feel especially indebted to Dr. Jouko Lahtinen, Dr. Jani-Petri Martikainen, Dr. Kirsi Peltonen and Dr. Emppu Salonen – thanks for placing your faith in me when I needed it the most. Thanks also to Dr. Olli

Heikkinen and M.Sc. (Tech.) Mikael Mieskolainen for their support once upon a time.

At this point it should be in order to present a near-sufficient yet non-exhaustive list of thanks and apologizations to my dear friends, often sharing their thoughts on whichever matter (or constitutes thereof). Thanks to Ameir, Tony and Ville for being true fellow physicists. The latter two I'd also like to thank for a particular occasion of "telling me so" and all that jazz. In some sense a physicist ought to be a natural philosopher, and I admit to have been equally delighted by the moments of talking physics as well as the occasions of prepending it with "meta" with you all. I remain grateful to Maaria, Jape, Liinu and Olli for bearing the blues and doing some heavy lifting. I'm thankful to Antti and Laura for their constructiveness and going through certain important paths in life. Furthermore, student life would have missed a lot without Ilkka & The Boys getting together, all the musical collaborations and the people in the guilds and student organizations.

Every story needs a beginning, and where wheels are set in motion, someone or something is usually involved. Even if it was long ago, I acknowledge that having I. Hyvärinen, K. Mäkinen and M. Vihla there was essential for me to ever set foot on the path of science and consequently finding a sense of purpose there.

My gratitude to my parents and my brother far exceeds what I could possibly express. After all, you gave me everything and were always there, able to take the good and the bad of my times.

Lastly, along the lines of Marillion, thank you whoever you are – albeit I should also like to add where- and whenever. While appreciating the act of picking this thesis up, I nonetheless hope it wasn't solely for obligation under some (perhaps educational) circumstances. I hope you get the do what fuels your passion and feels meaningful. Though why bother giving such a comment, you may ask. Ask ahead.

This one's for You who are yourself.

Helsinki, May 24, 2019

Toni Mäkelä

Toni Mäkelä

Contents

1 Introduction **1**

2 Theoretical background **3**
2.1 Conventions for notation and relativistic kinematics 3
2.2 The Standard Model 5
2.3 The metastability of the electroweak vacuum 8
2.3.1 The Higgs mechanism 8
2.3.2 Radiative corrections to the Higgs field 9
2.4 The mass of the top quark 11
2.4.1 Interpretation of quark masses 12
2.4.2 Top quark mass measurements 13

3 Physics at hadron collider experiments **16**
3.1 Concepts in experimental high-energy physics 16
3.2 Monte Carlo event generation 17
3.2.1 Phenomenological models of parton showering and hadronization . 18
3.3 Jets 19
3.4 The Tevatron 20
3.5 The DØ experiment 21
3.5.1 The DØ run II iterative midpoint algorithm 22

4 Methodology of jet energy scale determination **23**
4.1 The p_{T}-balance method 23
4.2 Samples and simulation setup 23
4.2.1 γ + jet events 24
4.2.2 EM+jet events 24
4.2.3 Event selection 26
4.3 Jet energy scale determination 27
4.3.1 Single-particle response functions 27
4.3.2 Flavour-dependent jet energy corrections 31
4.3.3 The binning variable of F profiles and shifting to reconstructed jet p_{T} level 32
4.3.4 Fitting MC simulation to detector data 34

5 Results **35**
5.1 Probe jet particle composition 35
5.2 Flavour fractions 36
5.3 JES determination via the p_{T}-balance method 37
5.3.1 Reproducing the DØ p_{T}-balance results 38
5.3.2 Our p_{T}-balance fits 41
5.4 Flavour-dependent jet energy corrections 45
5.4.1 Reproduced DØ results 45
5.4.2 Flavour-dependent jet energy corrections resulting from our fit . . 46

6 Discussion **48**
6.1 Differences between our F_{corr} determination and DØ 49
6.2 Propagating the corrections to top mass analyses 49

7 Conclusions **52**

Appendices

Appendix A DØ response parameters **55**

Appendix B Notes on fitting **77**
B.1 The Gauss-Newton method 78
B.2 Fit convergence and degrees of freedom 79
B.3 Propagating the fit parameter uncertainties 80

Appendix C Details on probe jet particle composition **81**

Appendix D Additional p_{T}-balance plots **88**

Appendix E Additional plots on reproducing the DØ F and F_{corr} **94**

Common symbols and abbreviations

Symbols

A, B, C	Fit parameters for hadron response
∂_A	Partial derivative with respect to a variable A
b-jet	A jet originating from a bottom quark
x^μ	Contravariant four-vector components
x_μ	Covariant four-vector components
∂_μ	Partial derivative with respect to x^μ
E	Particle or jet energy
E'	Jet energy estimator $p_{\mathrm{T}}^{\mathrm{tag}} \cosh(\eta^{\mathrm{probe}})$
E_{T}	Transverse energy
$\not{E}_T$	Missing transverse energy
F	Jet correction factor
F_{corr}	Jet correction factor (over avg. γ+jet F)
g-jet	A gluon-initiated jet
lq-jet	A jet originating from a light quark (up u, down d, strange s, charm c)
ϕ	Angle in the transverse plane
$\mathscr{L}$	Lagrangian density
$\mathcal{L}$	Luminosity
$p_n^{(i)}$	Single-particle response parameters for particle type n
p_z	Longitudinal momentum
γ	Lorentz factor or photon (context dependent)
m	Mass
$g_{\mu\nu}$	Metric tensor components
$g^{\mu\nu}$	Inverse metric tensor components
$\hbar$	Planck's reduced constant
η	Pseudorapidity or eta meson (context dependent)
y	Rapidity
c	The speed of light in vacuum

$p_{\mathrm{T}}^{\mathrm{probe}}$	Magnitude of probe jet transverse momentum
$p_{\mathrm{T}}^{\mathrm{tag}}$	Magnitude of tag object transverse momentum
$\mathcal{R}_{\mathrm{cone}}$	Jet cone radius
R_i^{MC}	Single-particle response for particle type i in simulation
R_i^{data}	Single-particle response for particle type i in simulation fitted to data

Abbreviations

ATLAS	An LHC experiment
CERN	European organization for nuclear research
CDF	Collider Detector at Fermilab, a Tevatron experiment
DØ	A Tevatron experiment located at point D0 along the accelerator ring
CMS	Compact Muon Solenoid, an LHC experiment
FNAL	Fermi National Accelerator Laboratory
corr	Correction / corrected
EMCAL	ElectroMagnetic CALorimeter
EW	ElectroWeak
FS	Final State
FSR	Final State Radiation
HCAL	Hadronic CALorimeter
IR	InfraRed, near-synonumous for low energy
IS	Initial State
ISR	Initial State Radiation
JES	Jet Energy Scale
LHC	Large Hadron Collider
LSQ	Least SQuare sum
MC	Monte Carlo simulation or default DØ SPR reconstruction
MC'	DØ P20ToP17 corrected SPR reconstruction
SM	Standard Model
SSB	Spontaneous Symmetry Breaking
SPR	Single Particle Response
QCD	Quantum ChromoDynamics

Chapter 1

Introduction

First observed in 1995 [1], the top quark is the heaviest elementary particle in the Standard Model (SM) of particle physics. The world average of its mass measurements is approximately 173 GeV [2]. In the SM, the masses of quarks are generated by spontaneous symmetry breaking of the ElectroWeak (EW) vacuum. The acting agent of this process is the Higgs field, the existence of which was confirmed by the discovery of a Higgs boson at a mass of approximately 125 GeV in 2012 [3, 4]. Excluding only neutrinos, the Higgs is coupled to every elementary particle with non-zero mass in the SM. The top mass is substantial enough to affect the behaviour of the Higgs field significantly via loop corrections – possibly enough to make the current EW vacuum a false one, waiting to eventually collapse into a global minimum. Therefore the value of the top quark mass is linked to cosmological predictions regarding the stability of the EW vacuum, and consequently that of the Universe as we know it [5, 6].

The SM offers no theoretical prediction for quark mass values. Rather, the experimentally measured masses must be inserted into the equations by hand via renormalization of divergent self-energies. What is more, there is further ambiguity on the definition of quark masses. This is due to colour confinement rendering the quarks never observable as free particles at energy scales below that of the phase transition of Quantum ChromoDynamics (QCD). Indeed, the connection between the mass values used by theorists and experimentalists is yet to be determined [7]. Nonetheless, the settling of the metastability problem requires a precise experimental result.

Contemporary understanding of the non-extended SM and experimental measurements have put the EW vacuum close to the border of stability [5, 6]. There is however some disagreement between the results of the various experiments that have performed a measurement of the top mass. In particular, the value obtained by the DØ experiment at Fermilab's Tevatron is inconsistent with those measured by the ATLAS and CMS collaborations using the Large Hadron Collider (LHC) at CERN, as well as that obtained by the CDF at Tevatron. The measurements of quark masses depend on the physics of sprays of particles called jets, which are captured by the detectors.

The task of experimental particle physics is to interpret the observed final states (FS) resulting from high-energy collisions of known initial state (IS) particles. The common approach is to compare the recorded detector output to simulation. The simulations are based on perturbation theory, starting with a Monte Carlo (MC) generated hard process at the parton level. The resulting particles are then hadronized into stable particles using phenomenological models. Followingly, the FS particles are clustered into jets. A simulation of the detector resolution is then applied on the FS particles to account for experimental factors in the differences between simulations and observations. In this work we reproduce the flavour-dependent jet energy scale (JES) corrections used at DØ. They are based on a calibration method that is based on the responses of individual particles, making it different to the approaches used at the more modern LHC experiments. During run II of the Tevatron, these corrections changed drastically between the IIa and IIb epochs at DØ. We examine the DØ JES methods and the determination of flavour-dependent jet energy corrections in detail and suggest improvements to the analysis.

We begin with a review of the theoretical framework of high-energy physics, a summary of the SM and the rise of the metastability problem in chapter 2. Chapter 3 contains a brief review of experimental matters and an introduction to the physics of jets, the objects observed by the detectors in particle physics experiments. In addition, we outline the DØ experiment. This discussion is done to the extent that is relevant for understanding the study of flavour-dependent corrections and interpreting the results of our simulations. The simulation methodology itself is discussed in further detail in chapter 4. There we outline the structure of our simulations and computations, describe the use of detector response simulations in JES determination and discuss the method of propagating flavour-dependent corrections to top quark mass measurements. The results of reproducing the DØ analysis as well as new results of our own are presented in chapter 5. This is followed by a discussion in chapter 6 and concluding remarks along with a future outlook in chapter 7.

Chapter 2

Theoretical background

In this chapter we introduce our notation and conventions for special relativistic physics. We briefly outline the SM and the metastability problem of the EW vacuum. The chapter is concluded by motivating the studies of DØ flavour-dependent jet energy corrections via top mass measurements.

2.1 Conventions for notation and relativistic kinematics

As the ElectroMagnetic (EM), weak and strong interactions are much more prominent in collider experiments than gravitation, we typically assume a zero coupling between spacetime curvature and energy content. Curvature would become important only at cosmic scales. Any collider existing to date is however approximately point-like and low-energetic on such measures. Hence we restrict to the Minkowski spacetime of special relativity, for which we use the metric tensor components $g_{\mu\nu} \doteq \mathrm{diag}(1, -1, -1, -1)$. For a more detailed overview of relativity and kinematics, see for instance [8, 9]. The Einstein summation convention [10] will be implied throughout the text. We shall in general denote vectors, matrices and tensors by a boldface font and drop the boldface when referring to the components only, or to quantities that are plain numbers. As a special case, we denote the vectors in a spacelike subspace of the Minkowski spacetime by an arrow. When discussing strictly Euclidean parameter spaces such as $\mathbb{R}^n$, $n \in N$, we shall drop the spatial minus signs and revert to the metric $g_{ij} \doteq \mathrm{diag}(1, 1, ..., 1) \doteq \delta_{ij}$.

Natural units are adopted by setting the speed of light and Planck's reduced constant to unity. Not only are equations simplified, but this also allows one to express all other units in powers of the units of energy – the electronvolt: 1 eV $\approx 1.602 \cdot 10^{-19}$ J. The derivations for the natural units dimensions of some frequently occurring quantities are shown in Table 2.1.

Table 2.1: The dimension and derivation of a conversion factor for some quantities to natural units. The square brackets stand for the units of the quantity inside the brackets. Here we assume $[E] = 1$ eV, one must not forget to also account for the difference of electronvolts and Joules if switching between the Systeme Internationale and natural units.

Quantity	Dimension d in natural units (eV^d)	Conversion factor	Derivation
Energy E	1	-	-
Mass m	1	$1/c^2$	$[m] = [E]/[c]^2$
Time t	-1	$\hbar$	$[t] = [\hbar]/[E]$
Length l	-1	$\hbar c$	$[l] = [\hbar][c]/[E]$

What is claimed to be physics must not be a mere consequence of the choice of coordinates or a frame of reference. Relativistic equations are stated as tensor relations, which are manifestly valid in all coordinate systems. The most relevant frames of reference in particle physics are the center of momentum (COM) frame, where the total momenta of the colliding particles sum to zero, and the laboratory frame (LAB), which is the rest frame of the detector. The average lifetimes of particles are measured in their proper time, which wont in general equal the coordinate time elapsing in the LAB frame.

A particle fulfilling the relativistic energy-momentum condition $p^\mu p_\mu = m^2$ is said to be *on-shell*, as the possible four vectors satisfying this condition draw a shell-like hyperbolic sheet in spacetime. The mass m obtained via this condition is the *invariant mass*, which is a Lorentz scalar. Physical particles existing in the FS must be on-shell, but virtual particles exchanged in quantum-mechanical scattering processes may also be *off-shell*. Experimentally, it suffices that physical particles are approximately on-shell. This is because mass measurements do not yield a precise value but rather a resonance peak with finite width, resembling e.g. the Breit-Wigner distribution.

A common choice of coordinates to represent 4-momenta in experimental particle physics is $p^\mu \doteq (E, p_\mathrm{T}, \eta, \phi)$. The temporal component E is for energy. The transverse momentum $\vec{p}_\mathrm{T}$ is the magnitude of the 3-momentum's projection to the plane transverse to the beam axis. Then in Cartesian coordinates with $\vec{p} = (p_x, p_y, p_z)$ we have $\vec{p}_\mathrm{T} = (p_x, p_y, 0)$ and $|\vec{p}_\mathrm{T}| \equiv p_\mathrm{T} = \sqrt{p_x^2 + p_y^2}$. Angular information of the direction is given by the azimuth angle ϕ and the *pseudorapidity* $\eta \equiv \ln\left(\tan^{-1}(\theta/2)\right)$. Here θ is the angle between the object's 3-momentum and the positive z-axis, defined as the direction of one of the accelerated particle beams. The value of $|\eta|$ is small for particles close to the transverse plane and away from the z-axis. The collision point cannot be completely surrounded by detectors, since openings must be left for the beams. Therefore only the particles with a low enough $|\eta|$ may hit a detector and be observed by the so-called *central experiments*. An alternative formula for pseudorapidity is given by

$$\eta = \frac{1}{2} \ln \left(\frac{|\vec{p}| + p_z}{|\vec{p}| - p_z} \right). \tag{2.1}$$

To illustrate the relation of the pseudorapidity presented in Eq. (2.1) to the ordinary *rapidity* y defined via the Lorentz factor γ, notice that $\gamma = \cosh y \Leftrightarrow \gamma(1+\beta) = e^y$. This leads to

$$y = \frac{1}{2} \ln \left(\frac{E + |\vec{p}|}{E - |\vec{p}|} \right). \tag{2.2}$$

which is, in the $|\vec{p}| \approx p_z$ limit, connected to the experimentalists' definition of rapidity

$$y \equiv \frac{1}{2} \ln \left(\frac{E + p_z}{E - p_z} \right). \tag{2.3}$$

There are different customs in literature, but in experimental context it is commonplace to use the rapidity as given in Eq. (2.3) instead of Eq. (2.2). One should also note that in the ultra-relativistic limit $E \gg m$ ergo $m \to 0$, we have that $E = |\vec{p}|$ and consequently the y of Eq. (2.3) agrees with the η of Eq. (2.1). As η is the more commonly used variable, the term rapidity is sometimes used even when referring to pseudorapidity. Rapidity is particularly useful in relativistic physics at collider experiments since it is additive, whereas ordinary 3-velocities are not. Differences in rapidity are also Lorentz invariant with respect to boosts in the z-direction.

2.2 The Standard Model

Here we overview the basic notions behind the contemporary elementary particle theory that collider experiments are probing. For good general references, see e.g. [11, 12, 13].

The SM fuses together the three successfully quantized fundamental interactions: the EM, the weak and the strong force. In the SM, all interactions are mediated by *gauge bosons*. The fundamental particles that constitute all matter – *quarks* and *leptons* – are spin-1/2 fermions, and there are three generations of them. Photons are the spin-1 vector gauge bosons responsible for the EM interactions between all electrically charged particles. The $W^{\pm}$ and Z bosons are also spin-1 vectors and mediate the weak interactions. The strong force that holds for instance protons and neutrons together is carried by gluons. The Higgs boson couples to and generates the masses of nearly all massive fundamental particles, excluding only neutrinos. The mass generation occurs via the spontaneous symmetry breaking (SSB) of the EW vacuum. The mechanism generating neutrino masses remains unknown, but a finite mass difference between generations is needed to explain their oscillation between flavour eigenstates. It is also unknown if there are other mass-generation mechanisms operating in the observable Universe or if the Higgs is responsible for the mass of dark matter as well. All SM particles are listed and grouped according to their interactions in Fig. 2.1.

Leptons experience only the EM and weak forces and may be observed as standalone particles. A quark then again carries one out of the three *colour charges* (r, g, b) of strong interactions. The contemporary description of strong interactions is Quantum ChromoDynamics (QCD), which describes the level of colour-charged *partons*: the fermion

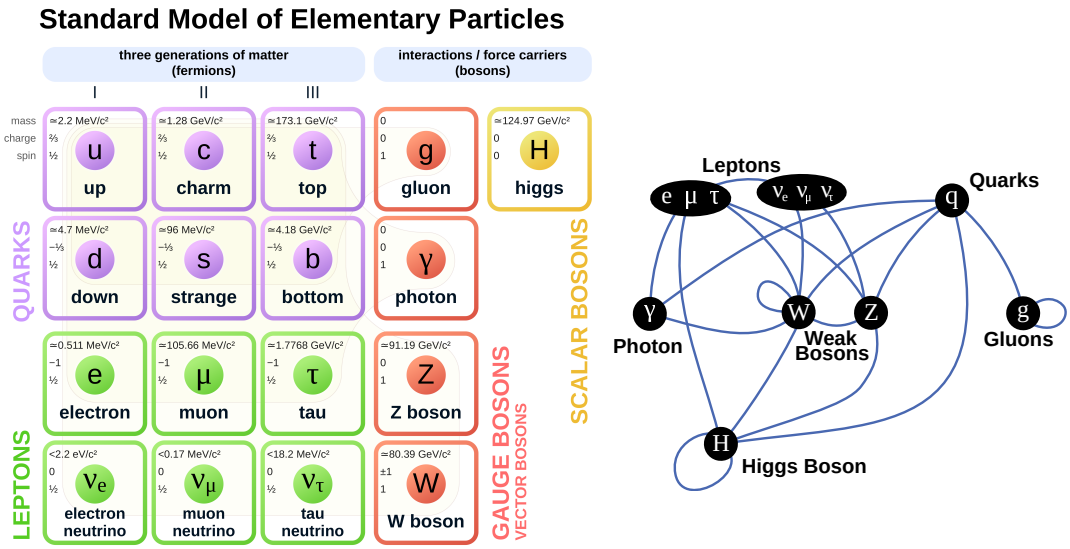

Figure 2.1: The table contains the SM particles and some of their quantum numbers. The graph shows which particles in the SM are coupled to each other. The curves connect the groups of particles that may appear in the same interaction vertex. A curve from a particle to itself means the particle has a self-coupling. Images obtained from [14, 15].

quarks and the vector gluons. Quarks carry one colour and gluons have both a colour and an anti-colour. They form observable composite particles called *hadrons*. According to quantum field theory, there is a relentless process of creation and annihilation of virtual *sea quarks* and gluons inside the hadrons. It is however approximated that the physics of hadrons is mainly determined by a bound state of more than two *valence quarks*. The hadron's quantum numbers are then in total equal to those of the valence quarks. *Mesons* are the bound states of one quark and one anti-quark with the corresponding anti-colour, so that the total colour charge sums to zero. *Baryons* contain three valence quarks or anti-quarks, each with a different colour. Also states with more valence quarks are possible, and *pentaquarks* have already been observed [16]. Albeit the QCD operators act on the level of free partons, unconfined quarks and gluons have never been directly observed in nature – only the hadrons can be detected. The parton model is nonetheless favoured due to explaining some scattering phenomena, such as the increasing steps in cross-sections as a function of energy when the production of on-shell heavier quarks from other generations becomes kinematically allowed. The model has also predicted new hadrons that have later been observed, see for instance [17]. The assignation of quark colours in a fashion that makes the hadron a colourless singlet is set to account for why there are no free partons – the quarks are said to be subject to *colour confinement*. Nevertheless, a rigorous explanation of confinement based on QCD computations is still elusive [13, 11].

The SM is built on $SU(3)_C \times SU(2)_L \times U(1)_Y$ gauge invariance. $SU(3)_C$ stands for the

colour charge of strong interactions and $SU(2)_L \times U(1)_Y$ is for the EW theory, where the weak bosons couple to left-handed leptons and the weak and electromagnetic forces have been unified under the concept of hypercharge. Further, Lorentz-invariant theories assume $\mathcal{CPT}$ invariance: we could not tell the difference in nature if all charges ($\mathcal{C}$), parity ($\mathcal{P}$) and time ($\mathcal{T}$) were simultaneously reversed. The theory need however not be invariant under the inversion of neither any single one of these nor the combination of any two of them. Alone or in pairs, these discrete symmetries are in fact expected, or have already been observed, to be violated in nature. See for instance the famous evidence obtained for $\mathcal{P}$-violation in [18] and for $\mathcal{CP}$-violation in [19]. $\mathcal{P}$-violation is included in the SM via weak interaction vertices that include a left-handed projection operator. Consequently, the SM includes only left-handed neutrinos and right-handed antineutrinos.

The SM Lagrangian is constructed by adding together the possible $SU(3)_C \times SU(2)_L \times U(1)_Y$ gauge-invariant scalar, spinor and vector field terms for the particles included in the SM. It has terms of the form

$$\mathscr{L}_{\text{SM}} = -\frac{1}{4} F^a_{\mu\nu} F_a^{\mu\nu} \tag{2.4}$$

$$+ i\overline{\psi}_i \gamma^\mu D_\mu \psi^i \tag{2.5}$$

$$+ \overline{\psi_{Li}} Y^{ij} H \psi_{Rj} + \text{h.c.} \tag{2.6}$$

$$+ (D^\mu H)^\dagger (D_\mu H) - V(H). \tag{2.7}$$

The vector boson kinematic terms and interactions are given on line (2.4), which should be recognized as similar to the kinetic term of the Proca Lagrangian. The usual partial derivatives of the field strength tensors are however replaced by *covariant derivatives*, which include additional terms to ensure gauge invariance. These are constructed out of the hypercharges, generators and respective gauge boson fields, giving the interactions of the fundamental bosons. The EW and QCD sectors have their own terms and the index a denotes a trace over the 2×2 (EW) or 3×3 (QCD) matrices. Due to being non-Abelian, QCD has further antisymmetric terms in the field strength tensor, contributing to the interactions between gluons [20, 21]. The additional terms in D_μ also couple the bosons to the fermions ψ participating in the interactions mediated by the respective boson. The fermion kinetic terms are included on line (2.5), which bears resemblance to the kinetic term of the Dirac Lagrangian. The Yukawa coupling of fermions to the Higgs field[1] is given on line (2.6) and gives rise to quark flavour mixing via non-zero off-diagonal elements in the flavour basis Yukawa matrix Y^{ij}. The term h.c. is for Hermitian conjugate. Finally, line (2.7) includes the machinery for EW symmetry breaking along with the resulting $W^\pm$ and Z boson mass generation and interactions with the Higgs.

Note that on line (2.6) we have explicitly denoted the handedness for one term in a manner that is required for the $SU(2)$ indices to be contracted appropriately, since the

[1] Here H is the Higgs doublet, to be explained in more detail in subsection 2.3.1.

left-handed spinors constitute $SU(2)$ doublets

$$\psi_L^i \doteq \left(\begin{bmatrix} e_L \\ \nu_{eL} \end{bmatrix}, \begin{bmatrix} \mu_L \\ \nu_{\mu L} \end{bmatrix}, \begin{bmatrix} \tau_L \\ \nu_{\tau L} \end{bmatrix} \begin{bmatrix} u_L \\ d_L \end{bmatrix}, \begin{bmatrix} c_L \\ s_L \end{bmatrix}, \begin{bmatrix} t_L \\ b_L \end{bmatrix} \right).$$

The ψ_R is for right-handed charged fermions. Notice however that conjugating a particle into its anti-particle reverses chirality. Mathematically it represents the $SU(2)$ singlets e_R,μ_R,τ_R for the leptons with hypercharge -1; u_R, c_R, t_R for the up-type quarks with hypercharge $2/3$ and d_R, s_R, b_R for the down-type quarks carrying hypercharge $-1/3$.

The above discussion has been done in the *interaction basis* where we use flavour eigenstates for the field operators. It simplifies the discussion of interactions, but one should notice that the conserved physical quantity describing a particle is mass, not flavour. Switching to the mass basis is done by applying suitable transformations via which the line (2.6) of $\mathscr{L}_{\text{SM}}$ can be written in terms of a diagonalized *mass matrix* sandwiched between the spinor multiplets. In this case the spinors become *mass eigenstates*.

2.3 The metastability of the electroweak vacuum

The EW vacuum is the energy minimum of the Higgs potential, which allows for SSB in the EW theory via the Higgs mechanism [22, 23]. In case there is no new physics below the Planck scale and if the relation of theory and experiment is interpreted right, current experimental results suggest that the EW vacuum may not be stable but metastable. Due to the need for renormalization, our understanding of the EW vacuum depends on the precise determination of the properties of the SM – in particular the mass of the heaviest particle, the top quark. It is hence of paramount importance that the measurements are robust and that our interpretations of the results are correct.

2.3.1 The Higgs mechanism

Consider the line (2.7) of the SM Lagrangian. Writing the potential $V(H)$ open, it is

$$\mathscr{L}_{\text{Higgs}} = (D_\alpha H)^\dagger (D^\alpha H) - \left(\mu^2 H^\dagger H + \lambda (H^\dagger H)^2 \right). \tag{2.8}$$

Since the $SU(2)$ doublet H is a $\mathbb{C}$ scalar, the potential can be depicted as a two-dimensional surface. Different possibilities of how the potential could look like under different circumstances are shown in Fig. 2.2. In the SSB, the Higgs doublet undergoes a change allowing it to be written as

$$H = \begin{bmatrix} H_1 \\ H_2 \end{bmatrix} \to \frac{1}{\sqrt{2}} \begin{bmatrix} 0 \\ v + h \end{bmatrix}$$

where the radial distance from the origin to the potential minimum is given by the vacuum expectation value v. The other component of the doublet can always be transformed to zero – any oscillations in the direction transverse to the radius correspond to

the Goldstone mode, yielding an unphysical field with massless bosonic excitations that are removable from the calculations. Oscillations in the radial direction are given by a $\mathbb{R}$ scalar field h, the excitations of which manifest as the physical Higgs boson [11, 13].

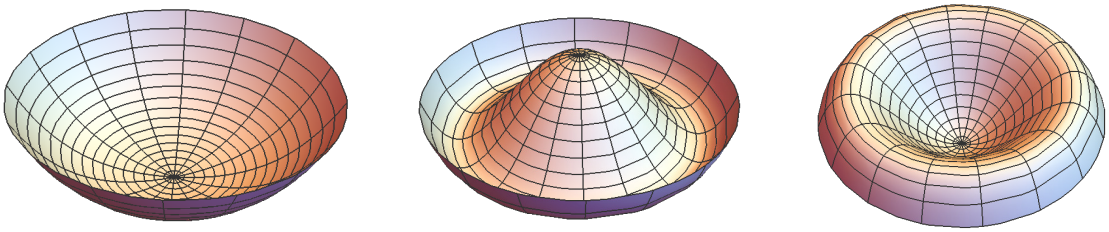

(a) $\mu^2 > 0, \lambda > 0$ **(b)** $\mu^2 < 0, \lambda > 0$ **(c)** $\mu^2 > 0, \lambda < 0$

Figure 2.2: The behaviour of the Higgs potential, depending on the signs of the parameters μ^2 and λ. The case **(a)** is commonly taken to be the state of the early Universe, **(b)** shows the Universe's current state, where the SSB has taken place and **(c)** is an alternative scenario where the Higgs mechanism would not produce the physics observed today.

This is the mechanism that allows elementary fermion and gauge boson mass terms to emerge in the SM, despite they are not initially included in $\mathscr{L}_{\text{SM}}$. The fermion mass terms now arise on line (2.6) of $\mathscr{L}_{\text{SM}}$ via the contribution of the non-zero vacuum expectation value. Composite particle masses can however be largely due to the field keeping the particles intact. For instance the proton mass is much larger than the sum of the constituent valence quarks [21]. The Higgs is hence not the whole story of mass.

2.3.2 Radiative corrections to the Higgs field

According to the standard cosmological model, the EW vacuum of the early Universe was in a state corresponding to Fig. 2.2a. The parameters μ^2 and λ then evolved as a function of the decreasing energy density into a configuration corresponding to Fig. 2.2b and elementary particles acquired their masses. The evolution of the parameters μ^2 and λ is studied via the renormalization group equations, and the Higgs propagator receives self-energy corrections from virtual loops. These corrections then contribute to the behaviour of the renormalized coefficient for the physical Higgs boson mass term h^2. Then in order to consider for instance the Higgs propagator, or the 2-point Green's function, at one-loop level one must take the sum

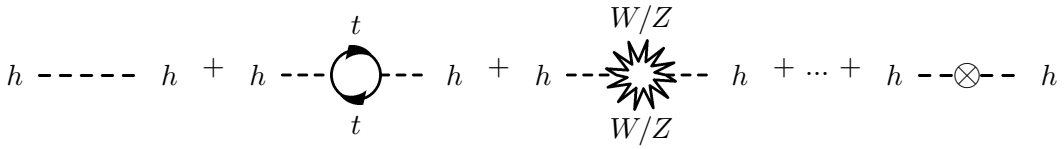

with the last term denoting the counterterm to cancel the infinities of loop diagrams and

leading to Higgs mass renormalization. Correspondingly, the corrections to the Higgs 4-point function – with terms of the order $\mathcal{O}(h^4)$ – are caused by the sum

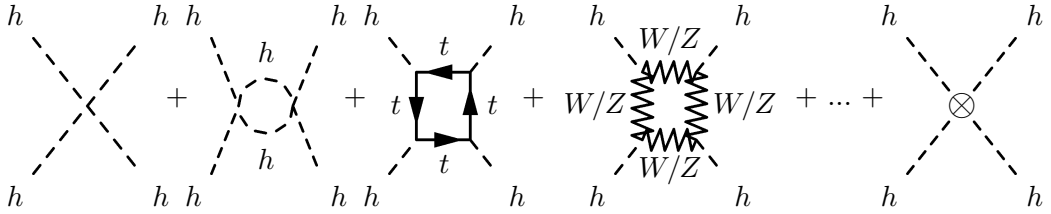

In total the h^4 terms arising from $(H^\dagger H)^2$ in the Higgs potential should have a factor with noteworthy contributions from the Higgs self-coupling, the top-Higgs Yukawa coupling Y_{tt} and the Higgs coupling to gauge bosons. Since $m_h \approx 125$ GeV $< m_t$ as measured by the CMS [3] and ATLAS [4] collaborations, the top is the heaviest elementary particle in the SM. Intuitively, as the Higgs coupling is related to mass, the top loop diagrams provide sizable corrections to the factors of the Higgs self-energy and self-interaction terms [24, 25].

Finding the renormalization group evolution of the Green's functions in a scalar φ^4 theory with a Higgs-like potential results in the Coleman-Weinberg [26] effective potential

$$V_{\text{eff}}(\varphi) = \frac{1}{4!}\varphi^4 \left(\lambda_R + \frac{3\lambda_R^2}{32\pi^2} \left[\ln\frac{\varphi^2}{\varphi_R^2} - \frac{25}{6} \right] \right),$$

with λ_R being the value where the 4-point vertex factor is renormalized and φ_R is some fixed scale. The metastability problem is essentially the question of whether or not the current EW vacuum is a false one, which should eventually collapse into the real vacuum at a lower energy. Therefore the interesting part of the calculation is in the limit $h \gg v$. For the field h, the part of the effective potential where the top quark contributes is then

$$V_{\text{eff}}(h) = \frac{\lambda}{4}h^4 + \left(\frac{9}{64\pi^2}\lambda^2 - \frac{3}{64\pi^2}Y_{tt}^4 \right) h^4 \ln\frac{h^2}{v^2}.$$

Dropping the subscript R from λ_R is due to the renormalization group serving to make λ a function of the arbitrary scale at which λ_R is defined. For the vacuum to be stable, we should then have $V_{\text{eff}}(h) > 0 \;\forall\; h \in \mathbb{R}$ [13].

Before the Higgs boson was found and any mass was measured for it, the metastability problem was used for setting Higgs mass limits within which the Universe could be stable. The present form of the metastability problem was brought up soon after the discovery of the Higgs boson. See for instance [27]. The problem is now considered to constrain the properties of the Higgs, top, strong coupling and possible new physics models in total. The perturbative calculations related to the metastability problem are currently at the next-to-next-to-leading-order level [5, 6]. The contemporary state-of-the-art is illustrated in Fig. 2.3. If the EW vacuum is not stable with the particle content of the SM, the hypothetical existence of new heavy particles could alter the calculation and

stabilize the vacuum. On the other hand, if the vacuum would turn out stable already in the SM, there would be one problem less where new heavy particles would be needed to provide a solution.

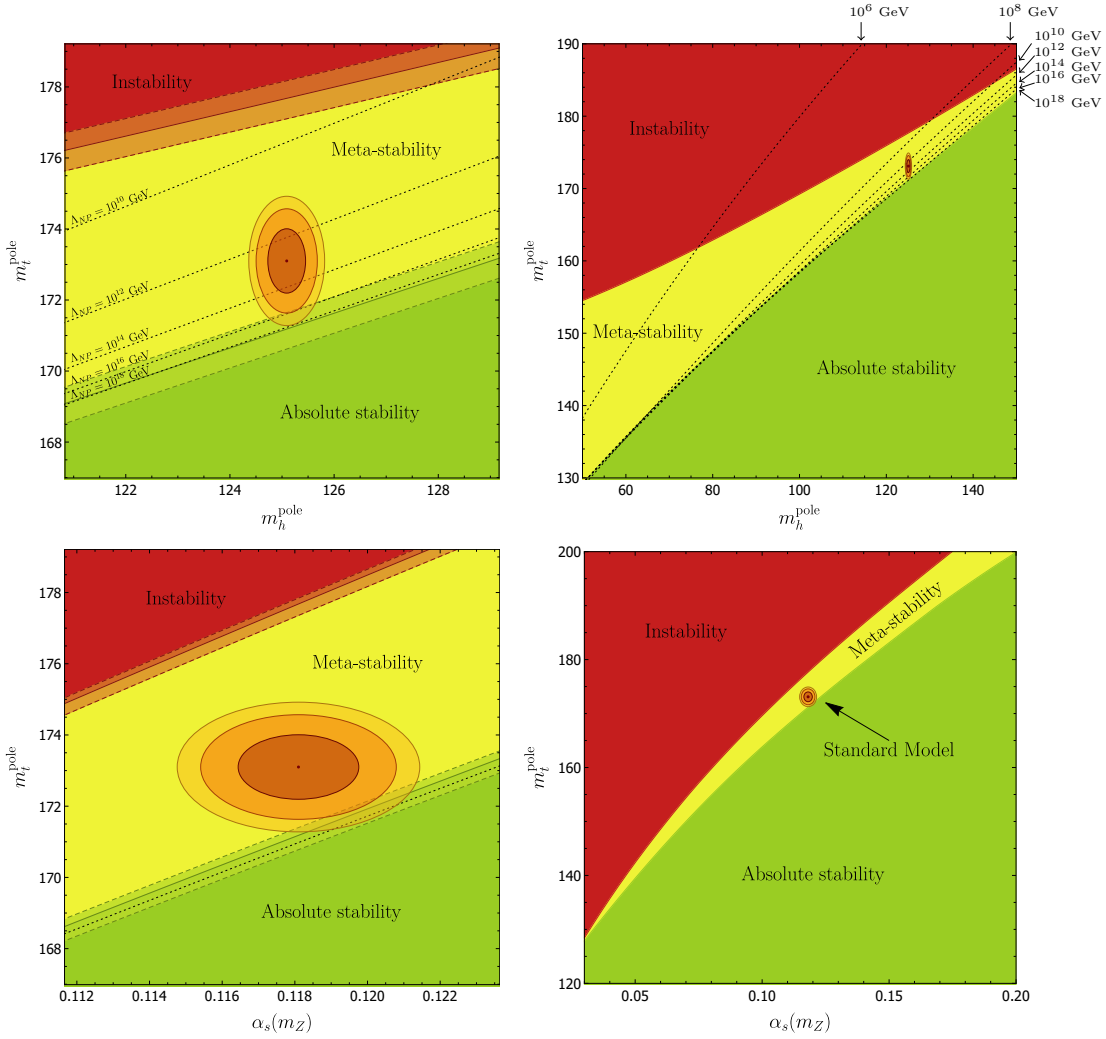

Figure 2.3: The metastability problem represented using the Higgs pole mass versus the top pole mass (above) and the strong coupling α_S versus the top pole mass (below). Images from [5].

2.4 The mass of the top quark

In this section we discuss the methods and results of contemporary top quark mass measurements. The study of jet energy calibration methods is motivated by these measurements. We begin with a brief introduction to the problem of defining a quark mass.

2.4.1 Interpretation of quark masses

Particle masses appear in the propagators, and also the fermion masses receive corrections from self-energy loop diagrams. Naively evaluating all diagrams and summing them together would however lead to the masses becoming infinite. The problem is circumvented by renormalizing the mass parameters to their measured values, with the drawback that the theory may no longer predict the masses. They become input parameters and are inserted into the calculations manually via counterterms to cancel the infinities [13, 11]. Besides the elementary particle masses, the free parameters of the SM include the fundamental couplings, the Higgs vacuum expectation value, parameters related to flavour mixing and one $\mathcal{CP}$-violating phase.

The mass renormalization can be done following several procedures with different motivations. Using the *pole mass* scheme is to demand that the pole at $p^2 = m^2$ in the fermion propagator

$$\left.\frac{i(p_\mu \gamma^\mu + m)}{p^2 - m^2 + i\epsilon}\right|_{\epsilon \to 0}$$

stays put. For free particles, this is then the physical on-shell mass. This scheme is interesting especially theory-wise, but it is not necessarily well-defined for quarks. This is because they are not colour-singlets and cannot be observed as free particles at low energies. The intuitive picture in perturbation theory would be to sum together all self-energy diagrams, which becomes a geometric series that can again be written in a form similar to the propagator. Only now the mass in the denominator is affected by the summation. Renormalizing the fermion mass then fixes this quantity, and it becomes the pole mass – the cause of the propagator's complex poles in the renormalized theory. One may also avoid the geometric series argument for self-energy diagrams using an alternative approach provided by the renormalization group. Nonetheless, the resulting form remains the same [13].

When it comes to experiment, the detector data is compared to Monte-Carlo (MC) simulations. A simulation is limited by finite temporal and computational resources and the perturbative expansion must be truncated before becoming too complicated – contemporary generators are based on leading order (LO) or next-to-leading order (NLO) computations. Hence the *Monte Carlo mass*, i.e. a preset mass parameter in the MC computations, cannot equal the full renormalized pole mass discussed above. What is more, the quarks are coloured objects but confinement enforces the detected decay products to be colourless. There must then be something extraneous or missing in the chain between the initial quark and the detected particles to explain this difference. The behaviour of m^{MC} may depend on the details of modeling the showering and hadronization. See chapter 3 for a brief discussion on the algorithms of the generators used in our simulations.

While studying this problem, theoretical physicists have come up with various alternative definitions for quark masses. Many modern calculations make use of the so-called *short-distance masses*. Whether or not some definitions can be linked more clearly to the MC-

masses of different generators is still a topic under study. For further information on the standard schemes, a good reference is provided by [13]. For more recent developments see e.g. [7, 28].

2.4.2 Top quark mass measurements

Fig. 2.4 shows that there is good agreement between the top mass results of the ATLAS, CDF and CMS experiments. However, the result of the DØ experiment is inconsistent with the other experiments, yet it is claimed to be very precise. A combination of the top-quark mass measurements from the Tevatron collider is given in [29]. For DØ top mass measurements in the leptons+ jets (l+jets) channel[2], see [30] explaining the matrix element method and [31] for a discussion on the kinematic fit and [32] for one of the latest analyses at 9.7 fb^{-1}. There are also methods for indirectly extracting the pole and $\overline{\text{MS}}$ top masses from cross-section measurements. For DØ results on this, see e.g. [33, 34]. The precision of these indirect pole mass measurements has recently increased and a recent result by CMS is $m_t^{\text{pole}} = 170.5 \pm 0.8$ GeV [35], whereas the most recent direct measurement in the l+jets channel at CMS has yielded $m_t^{\text{MC}} = 172.25 \pm 0.08$ GeV [36]. Additionally, efforts have been taken for a more precise calibration of the m_t^{MC} of direct measurements [37, 38].

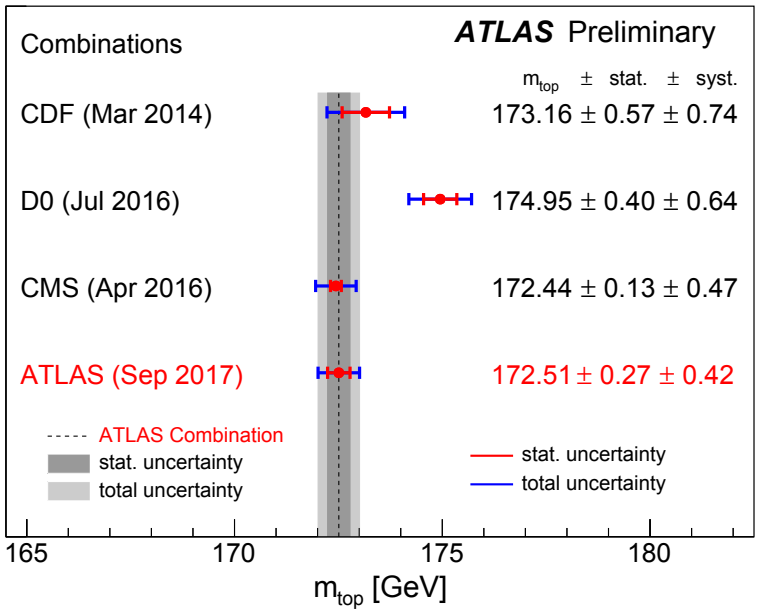

Figure 2.4: Comparison of the m_t results from ATLAS, CDF, CMS and DØ experiments. The DØ result can be seen to be inconsistent with the other results. Image from [39]

[2]For a description of jets, see ch. 3.

Let us consider for instance the measurements of top mass in the l+jets channel, depicted in Fig. 2.5. The top quark t is produced along with an anti-top $\bar{t}$ via the decay of a high-energy gluon g. The t and $\bar{t}$ decay dominantly into pairs formed by a W-boson and a b or $\bar{b}$ quark. In this channel one of the W bosons decays further into a charged lepton and a neutrino while the other one decays into quarks. Eventually the quarks form jets. In total, the top mass measurements performed in the l+jets channel require the identification and reconstruction of four jets. Additionally, there must be an electron or a muon and a sufficient amount of missing energy due to the unobserved neutrino. At least two of the jets must be tagged as originating from a b-quark. In the kinematic fit method, it is demanded that an on-shell W-boson can be reconstructed from the 4-momenta of the two remaining jets. In case more than two b-jets are present in the event, they must also be considered as possibly originating from a W-boson's daughter quarks. The different configurations of assigning the particles to the decay chain are then permuted and the final interpretation of the jets' origins is based on the on-shell W boson reconstruction arguments. Finally, the top mass is computed via the 4-momentum sum of one of the b-jets and the W boson. The measurements are therefore sensitive to jet reconstruction in general, but in particular to that of b-jets. There are also other m_t^{MC} measurement channels such as the all-jets and dilepton channels, but the need for precise b-jet identification and reconstruction remains a general feature.

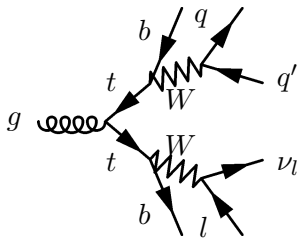

Figure 2.5: A process contributing to the l+jets channel. Here a gluon g forms a $t\bar{t}$-pair. Both the top and the anti-top decay into a W-boson and a b or $\bar{b}$ quark forming b-jets. One of the W-bosons decays leptonically and the other one into a quark–anti-quark pair $q\overline{q'}$. The prime serves to remind that q and q' need not be of the same flavour due to possible quark mixing.

The flavour-dependent jet energy corrections used at DØ are shown in Fig. 2.6. The determination of these factors is explained in detail in chapter 4, but a key observation can already be made: between the runs IIa and IIb, there is less change in the correction factors for light-quark (lq) and gluon (g) initiated jets than for the b-jets. It is possible that the drastic change in b-jet correction factors combined with the other factors' more modest changes may have had an effect on top mass analyses. Since the integrated luminosity[3] is 1.081 fb^{-1} for run IIa and 8.655 fb^{-1} for IIb, the factors used during run IIb will dominate the results. Run IIb is divided further into three epochs, which are known as IIb1, IIb2 and IIb3-4. However, the trend of the flavour-dependent corrections can be seen to be similar for all run IIb epochs [40].

[3]For luminosity, see ch. 3.

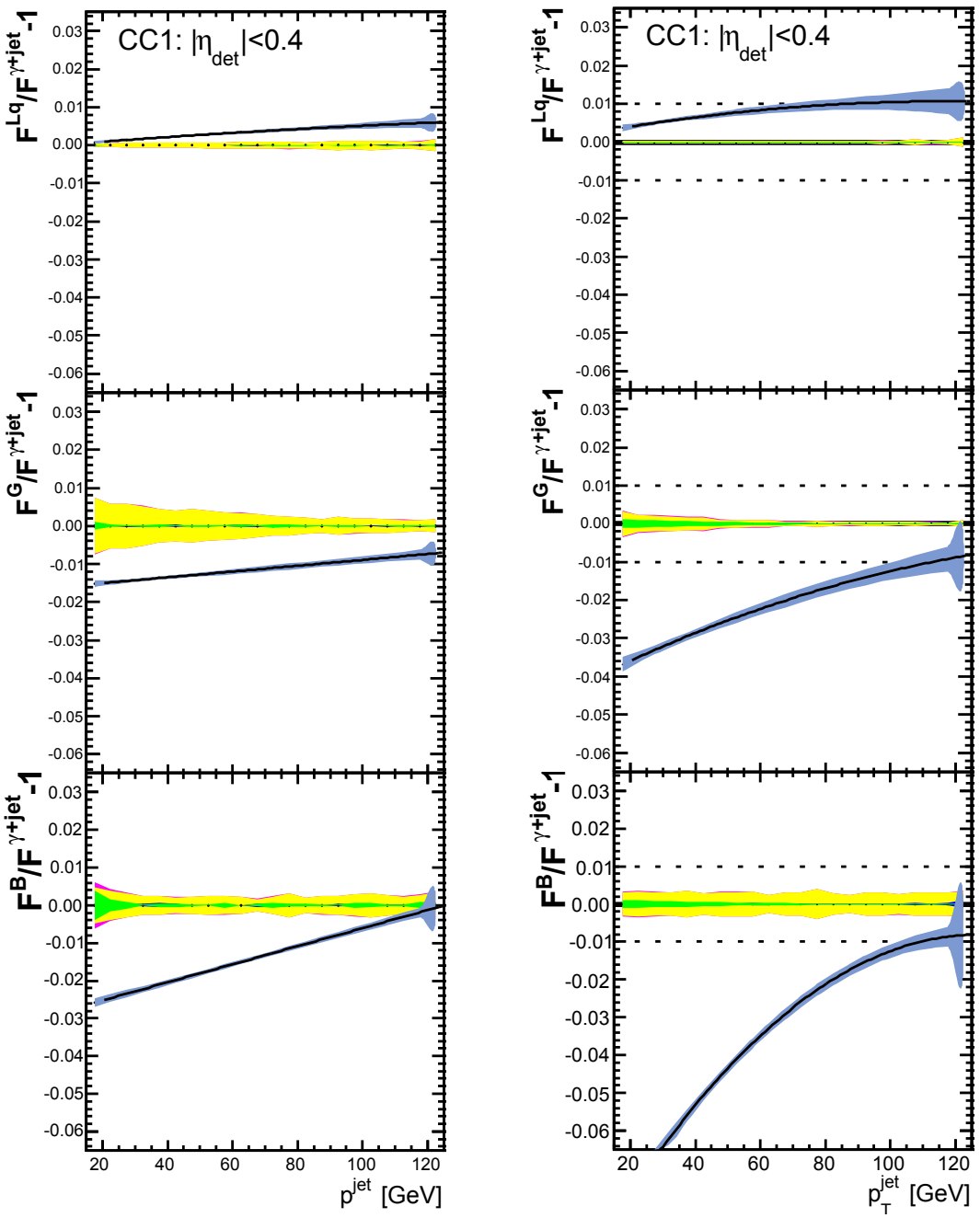

(a) Run IIa. **(b)** Run IIb2.

Figure 2.6: Flavour-dependent jet energy corrections at DØ, obtained from [41] for run IIa and from [40] for run IIb2, one of the three run IIb epochs. The blue bands represent the statistical uncertainty reported by DØ and the other bands represent systematic uncertainties.

Chapter 3

Physics at hadron collider experiments

In this chapter we discuss some general topics in experimental particle physics that are not restricted to the determination of flavour-dependent jet energy corrections at DØ. The latter will be addressed in detail in chapter 4. The information presented here is applicable to several analyses performed at DØ and – unless the DØ is explicitly referred to – at other experiments as well.

3.1 Concepts in experimental high-energy physics

Rather than accelerating and colliding individual particles, a particle accelerator operates on collections of particles known as *bunches*. Suppose there are N_b bunches circulating in the machine ring with approximately N particles in each bunch. *Instantaneous luminosity* is a quantity related to the frequency of events at a collider experiment. It is given by

$$\mathcal{L} = \frac{N N_b}{4\pi\sigma_x\sigma_y}.$$

The number N_b tells how many bunches are currently circulating in the collider. Approximating that the distribution of particles in a transverse cross section of a bunch would be Gaussian, the standard variations σ_x and σ_y serve as a measure for beam size in the x and y directions. The concept of *integrated luminosity* is then related to the amount of data that has been acquired within a given time-window.

Central experiments focus on observations at low pseudorapidity η and high p_{T}. Therefore, many quantities are defined in a way involving a projection to the transverse plane. For instance the *transverse energy* is defined as $E_{\mathrm{T}} \equiv \sqrt{p_{\mathrm{T}}^2 + m^2}$. It is not to be confused with the *missing transverse energy* or *missing* E_{T} (MET), which is given by the

vector sum

$$\vec{\not{E}}_T \equiv -\sum_{i \in \{\text{particles}\}^{\text{Observed}}} \vec{p}_{\mathrm{T},i}.$$

The magnitude of the MET vector is denoted by $|\vec{\not{E}}_T| \equiv \not{E}_T$. The MET serves as a measure for the magnitude and direction of unmeasured p_T in an event. It is due to the conservation of transverse momentum, as the initial colliding particles have approximately zero p_T. The main contributions to MET come from neutrinos and other particles not interacting with the detector, as well as those observed unusually poorly or not at all. For instance any particle piercing an uninstrumented region of the detector may increase MET even if it would interact with the detector matter.

3.2 Monte Carlo event generation

Recall that in the parton model the properties of a hadron are determined largely by the valence quarks. Then if one could – loosely speaking – pick a parton out of a hadron, the valence quarks would most probably be observed to be present in the hadron. There is however a non-vanishing possibility of selecting a sea quark or gluon. The information on the contents of the protons and antiprotons collided at high-energy experiments is contained in a Parton Distribution Function (PDF). It connects the initial state hadrons to the parton-level hard processes generated in MC simulations. The PDF has to be measured experimentally, since the problem of hadron structure falls within the regime of non-perturbative QCD.

The generation of scattering events in a simulation is done using perturbative techniques. The process starts by selecting two partons from the colliding hadrons according to their PDFs by Monte Carlo methods. These are taken as the initial state particles of a so-called parton level *hard process*, for which one can calculate matrix element and the cross-section $\hat{\sigma}$ via perturbation theory[1]. Applying a suitable factorization theorem [42] the total cross section can be calculated via an integral of the form

$$\sigma = \sum_{a,b} \int_0^1 \int_0^1 dx_1 dx_2 f_a(x_1) f_b(x_2) \hat{\sigma}_{ab}(x_1, x_2) + \mathcal{O}(\Lambda^2_{\mathrm{QCD}}/Q^2)$$

where f are the PDFs according to which the partons a and b are sampled. x_1 and x_2 are the fractions of momentum the particles take from the hadrons, assuming a squared momentum transfer Q^2 much less than the squared QCD scale Λ^2_{QCD}. A practical overview of the topic is given for instance in [43]. The energy density of the collision must be sufficiently high for the partons to be in the domain of *asymptotic freedom* [44] where confinement effects become small and the partons can be approximated as free particles. After the hard process is calculated, the MC generator proceeds to the phases known as *showering* and *hadronization*. At this stage, a set of hadrons is produced from

[1] A hat over a quantity is commonly used for referring to a parton- / matrix element level quantity.

the end products of a decay chain of unobservable intermediate objects. If a produced hadron is too short-lived to reach the detector volume, it is decayed further into particles that may be observed in the FS.

There is a multitude of objects and phenomena that are often observed in an event but which are not described by the hard process. These form what is collectively entitled the *underlying event*. One such contribution is given by *multi-parton interactions*, in which more than one parton from each colliding hadron becomes involved with the same hard process. As the hard process FS partons become connected to the colliding hadrons' remnants, the parton colours may need to be reassigned. This is called *colour reconnection* [45]. In event generator lingo, there is also the possibility of Initial State Radiation (ISR) and Final State Radiation (FSR). These account for the presence of an additional gluon in the hard process final state, attached to either the IS or FS partons as illustrated in Fig. 3.1. Physicswise it ought to be borne in mind that in case the FS contains such an additional gluon, both the ISR and FSR type amplitudes should be summed. For MC generators, the handling of ISR and FSR may however differ greatly. Besides the underlying event, the *pile-up* caused by multiple scattering events taking place in the same bunch crossing increases the amount of background noise in a measurement.

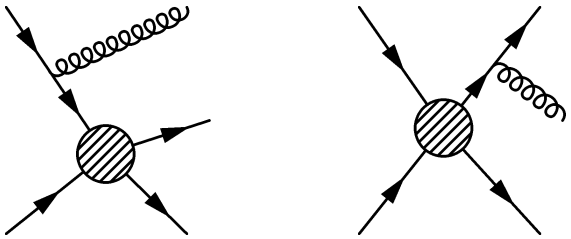

(a) ISR **(b)** FSR

Figure 3.1: Initial and final state radiation pictured as the emission of a gluon by either the initial or final state partons.

3.2.1 Phenomenological models of parton showering and hadronization

As there is no complete theoretical description of hadronization, the MC generators evolve partons into FS particles using various showering and hadronization algorithms. These models are of phenomenological nature at best and cannot be taken as rigorous. Rather, they are based on intuitive ideas of what might occur in the process and refined to improve the agreement of detector data and simulations.

The Pythia [46] series of MC generators uses the Lund string model. It is based on the production of string-like objects whose endpoints are interpretable as parts of a mesonic or a baryonic system. For instance a quark on one end and an anti-quark or a

diquark on the other would devise a valid configuration. As the partons emanate further from their point of production, the string stretches. New pairs of string endpoints are produced along the string in a Markovian fashion. If energy-wise preferable, the string can eventually break, possibly producing additional hadrons in between the new two pieces of strings. [46, 47].

The HERWIG [48, 49] line, including e.g. the HERWIG++ and HERWIG 7 generators, invokes *angular-ordered showering* and *coherent branching* to first form *clusters* out of the partons. Each incoming and outgoing coloured hard process particle is a starting point for showering. They form branches by radiating other particles according to a decreasing evolution scale parameter. All hard process particles are assigned a pair. The pair's angular difference sets an upper bound to the angle at which new coloured particles may be radiated. The angular ordering then means that the daughter partons resulting from a branching may continue to branch, but the evolution scale sets an upper limit to the opening angle. Once the phase-space no longer allows for more branchings, any remaining gluons are decayed into quarks. The quarks are then grouped into hadrons, which are decayed further until the level of stable FS hadrons is reached [48].

3.3 Jets

Starting from the parton level and proceeding through the level of particles, the highest stage to be eventually reached is that of *jets*. The FS particles produced in a decay chain starting from the same parton tend to be spatially more or less close to each other. Considering a detector, this leads to the observation of calorimeter tower groups i.e. localized regions of higher energy than their neighbourhoods. If all jets were reconstructed perfectly, their 4-momenta would equal the 4-vector sum of all their constituent FS particles. In MC simulations, the jets are formed out of the MC-produced FS particles. This is performed via algorithms that group nearby particles together into jets according to method-specific rules. In section 3.5.1 we discuss the DØ iterative midpoint algorithm, which can be used to cluster either MC particles or calorimeter towers in detector data into jets.

The characteristics of jets tend to depend on the flavour of the parton giving rise to the jet in the first place. Therefore also the jets are assigned a flavour in a process known as *tagging*. For example the particle composition of a jet as well as the amount of scaling needed to bring the energy of a detected jet to the level of pure MC simulations can vary greatly. Statistically one may however observe that jets of certain flavour embody some common features. It is therefore important to identify a jet's flavour correctly. Different definitions and techniques for this are summarized in e.g. [50]. In MC simulations, the problem is nevertheless simplified as the hard process parton information is directly available and can be checked by tracing back a generated particle's history. We utilize the common procedure of adding *ghostified* partons to the jets in the MC samples. The ghosts are 4-vectors carrying a parton-level flavour tag and a direction agreeing with a

jet, but whose momenta have been shrinked to a negligible magnitude so that they do not cause any considerable error to the calculations.

However, jets also contain particles or energy not coming directly from the parton whose flavour the jet was identified with. A jet is a collection of FS particles, which are colour singlets. Hence also the jet must be colourless as a whole, albeit it originates from a coloured particle. Something else must then be either coming in or going out to make it colourless. Naturally the MET plays an important role in the context of jets, since for instance neutrinos never end up in the reconstructed jets.

3.4 The Tevatron

The Tevatron is a circular particle accelerator complex located at the Fermi National Accelerator Laboratory (FNAL) in Batavia, Illinois, USA. It collided proton-antiproton beams at a COM energy of 1.96 TeV and was home to two large experiments, the Collider Detector at Fermilab (CDF) and the DØ. A schematic illustration of the Tevatron accelerator and related instruments is shown in Fig. 3.2.

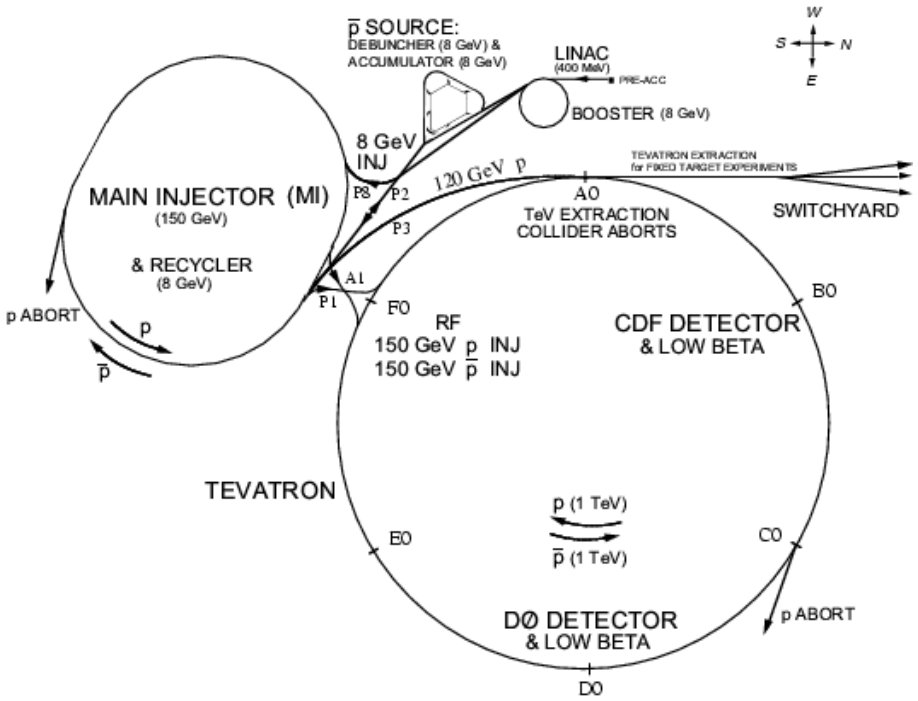

Figure 3.2: Schematic overview of the Tevatron and related accelerator machinery. Image obtained from [51].

3.5 The DØ experiment

The DØ experiment collected data until 2011. A cross-section of its detector is shown in Fig. 3.3. The proton and antiproton beams meet at the interaction point in the center of the detector. The point of collision is the central tracking system, which more specifically consists of a silicon microstrip tracker and a central fiber tracker. Originally there was no magnetic field in the tracker, but after the detector upgrade a 2 T solenoidal magnet was introduced [52]. The detected particles' energies are captured by the calorimeter. The calorimeter consists of an electromagnetic (EMCAL) section closest to the point of collision, surrounded by the hadronic calorimeter (HCAL) part that is further divided into the fine and coarse HCAL. In short, the operational principle of the calorimeter is that particles interact with matter surrounded by liquid argon. The matter is mostly depleted uranium in the EMCAL, an alloy of uranium and niobium in the fine HCAL and steel or copper in the coarse HCAL. The liquid argon is used for both refrigeration and as an active medium, permitting the particle-calorimeter matter interactions to be observed. The calorimeter temperature is maintained at approximately 90 K by cryostats [52].

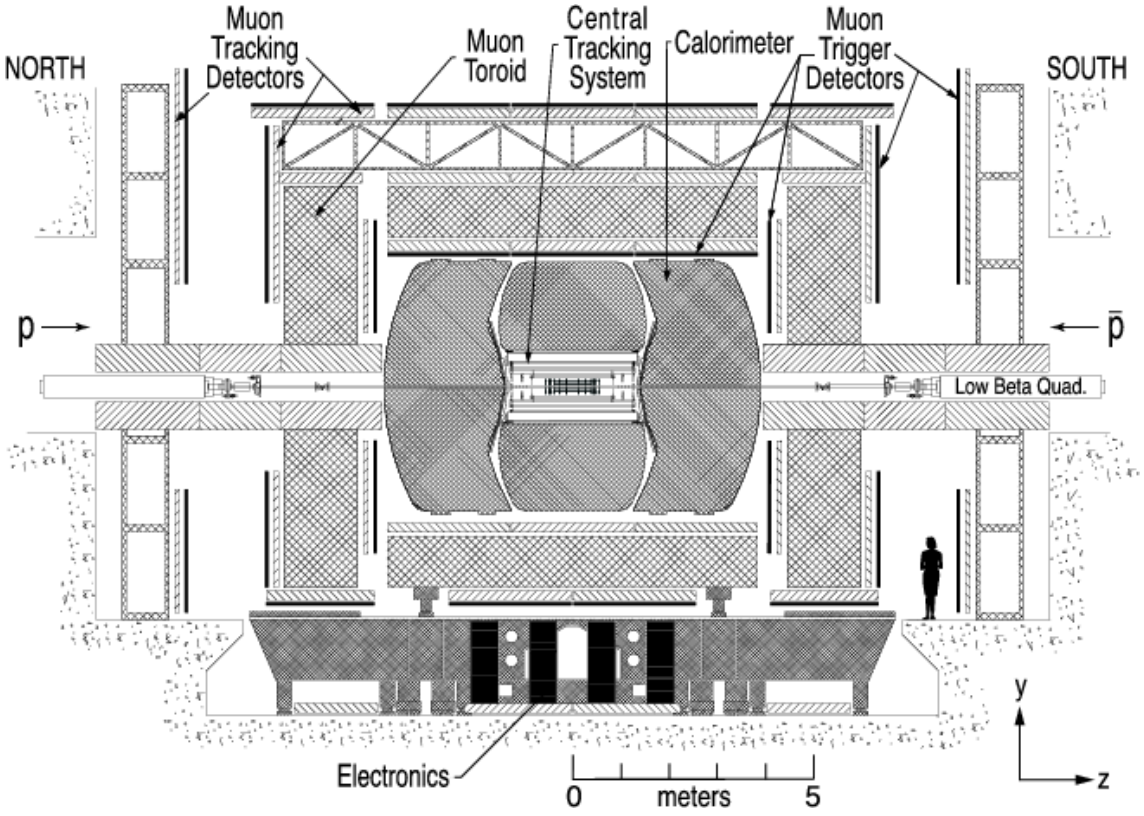

Figure 3.3: A schematic picture of the DØ detector. Image from [52].

Most particles are stopped by the different layers of the calorimeter, at latest by the coarse HCAL. However, weakly interacting ones such as muons make it through to the first muon trigger detector and proceed to pass the muon toroid. The muon toroid is a toroidal magnet designed to aid in the identification of muons and in the reconstruction of their momenta. This is done via the angular difference of the incoming and outgoing muon tracks [53]. The muon toroid is surrounded by muon tracking detectors and an another set of muon trigger detectors.

3.5.1 The DØ run II iterative midpoint algorithm

During Tevatron run II, the DØ experiment's jet algorithm of choice was the iterative midpoint algorithm. The algorithm has been implemented to FastJet as the D0RunIICone plugin [54, 55], which we employ in our simulations. First, the algorithm finds proto-jets by calculating the 4-vector sum of the 4-momenta of all particles (in case of MC simulations) or the calorimeter towers (in case of experimental data) within a given cone radius. The resulting 4-vector is then used for calculating the rapidity as given by Eq. (2.2), the azimuthal angle ϕ and the transverse momentum p_{T}. The algorithm merges proto-jets into a single jet if over 50% of the p_{T} of the lower energy jet overlaps with the other jet [56]. Therefore, we use a split ratio of 0.5 in the FastJet plugin. The next step of the algorithm is to take (y, ϕ) as the new center of the jet, around which a new cone is formed. The algorithm is considered converged when $\Delta\mathcal{R} \equiv \sqrt{(\Delta\eta)^2 + (\Delta\phi)^2} < 0.001$ between two last iterations' jet axes. Finally, jets with $p_{\mathrm{T}} < 6$ GeV are dropped [56], so we set this threshold to the FastJet plugin's minimum jet E_{T} parameter as the closest analogue.

The iterative midpoint algorithm has the known drawback of being infrared (IR) unsafe. It is IR_{3+1} unsafe in general and IR_{2+1} unsafe for jets with energy near the jet minimum E_{T} [57]. Infrared unsafety means that if new soft i.e. low-energy particles are introduced to the event, they may act as new seeds for finding jets. This can change the resulting set of jets drastically. As a result, for instance the selections of jets given for LO and higher-order QCD calculations may differ in such a way that the cancellations desired in perturbative calculations no longer occur. The label IR_{n+1} stands for IR-unsafety in case there are n nearby hard particles and one soft particle [58].

Chapter 4

Methodology of jet energy scale determination

4.1 The p_{T}-balance method

To determine the Jet Energy Scale (JES) and flavour-dependent jet energy corrections, We use the p_{T}-balance method. The studied observable in this method is the ratio of the transverse momenta of a *probe* and a *tag* object. The probe is a jet and the tag is either a high-p_{T} prompt photon or an *EM-object* comparable to it. The idea is that the tag is to be easily distinguished in the EMCAL and reconstructed with good precision, and ideally it would be back-to-back to the parton initiating the probe jet. The p_{T}-balance ratio can then be taken as a measure for jet response [56].

4.2 Samples and simulation setup

In our simulations, the events are generated using the PYTHIA 6 and HERWIG 7 MC generators. We use the software LHAPDF 6.2.0 [59] with the PDF CTEQ6L1 [60] as the structure function. Jets are formed out of the MC output FS particles using the FASTJET 3.3.0 [57] software with the DØ run II midpoint algorithm plugin. For the plugin, we set the cone radius parameter to $\mathcal{R}_{\mathrm{cone}} = 0.5$ as in [41, 40], split ratio to 0.5 and discard jets with transverse energy $E_{\mathrm{T}} < 6$ GeV as in [56]. After this, the generated events are saved into tuples and further analysis is done using ROOT [61] version 6.15.

The original pyevwt.f routine distributed with PYTHIA 6 is a dummy. It is intended to be modified to allow for event weighting, and we used it to enable $\hat{p}_{\mathrm{T}}$-weighting. For further details on our simulation setup, including this change, see the codes in the GitHub repository [62].

4.2.1 γ + jet events

For producing the γ+jet sample, we set the MSEL variable in PYTHIA 6 to 0. This allows for user-specified event type selection in the generation. We chose the same processes as reported in [56]. The Feynman graphs of the hard processes involved in the sample are illustrated in Fig. 4.1. For HERWIG 7 studies, we enable the MEGammaJet subprocess matrix elements to produce the γ+jet sample..

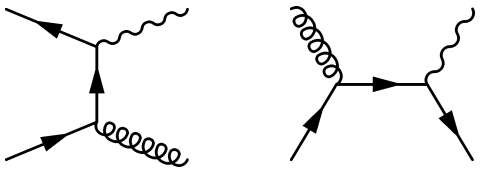

(a) $q_i\bar{q}_i \to g\gamma$ **(b)** $q_i g \to q_i\gamma$

Figure 4.1: Examples of LO diagrams for the hard processes enabled in PYTHIA 6 γ+jet sample production.

4.2.2 EM+jet events

This sample is constructed out of dijet events ergo general QCD events where both partons in the LO hard process FS are jet-initiating quarks or gluons. For our p_{T}-balance studies there is the additional requirement that one of the jets ought to be an EM-object, corresponding to the tag photon in γ+jet events. The tag object's energy should come mostly from photons, as can be the case e.g. if a high fraction of the jet energy is carried by π^0 or η mesons that decay rapidly into photons. The response of such a jet is very high, almost like that of the leading photon in γ+jet events. A quick Ansatz to provide the necessary cut for finding such events in a generic dijet sample would be for instance to demand the fraction

$$f_{\mathrm{EM}} = \frac{1}{E_{\mathrm{jet}}^{\mathrm{gen}}} \left(\sum_{i \in \{ {}^{\gamma \text{ or } l}_{\text{in jet}} \}} E_i^{\mathrm{gen}} + \frac{1}{2} \sum_{j \in \{ {}^{\text{Hadrons}}_{\text{in jet}} \}} E_j^{\mathrm{gen}} \right)$$

to be above a high threshold value, e.g. 0.8. Events passing such a cut are however only a few in a thousand. Given finite computational resources, this would leave us with little statistics. Besides, it would enforce us to make assumptions on the MC generators' ability to simulate such rare events with adequate precision. Thus we emulate the EM objects by regular jets in a generic dijet sample, but reconstruct them with photon response instead of the respective functions of each particle in the jet. The individual particle responses are discussed in detail in subsection 4.3.1. This endowes us with more statistics, as we may consider both ways of assigning the tag and probe. For a discussion on p_{T}-balance addressing also the reconstruction of a jet as a photon, see [63].

In dijet sample production, we set the PYTHIA 6 MSEL variable to 1. This is a high-p_{T} QCD process preset containing the hard processes depicted in Fig. 4.2 [46]. This was done to obtain a similar selection of processes as given in [56]. For HERWIG 7 we enable the subprocess matrix elements MEQCD2to2 to attain a similar selection.

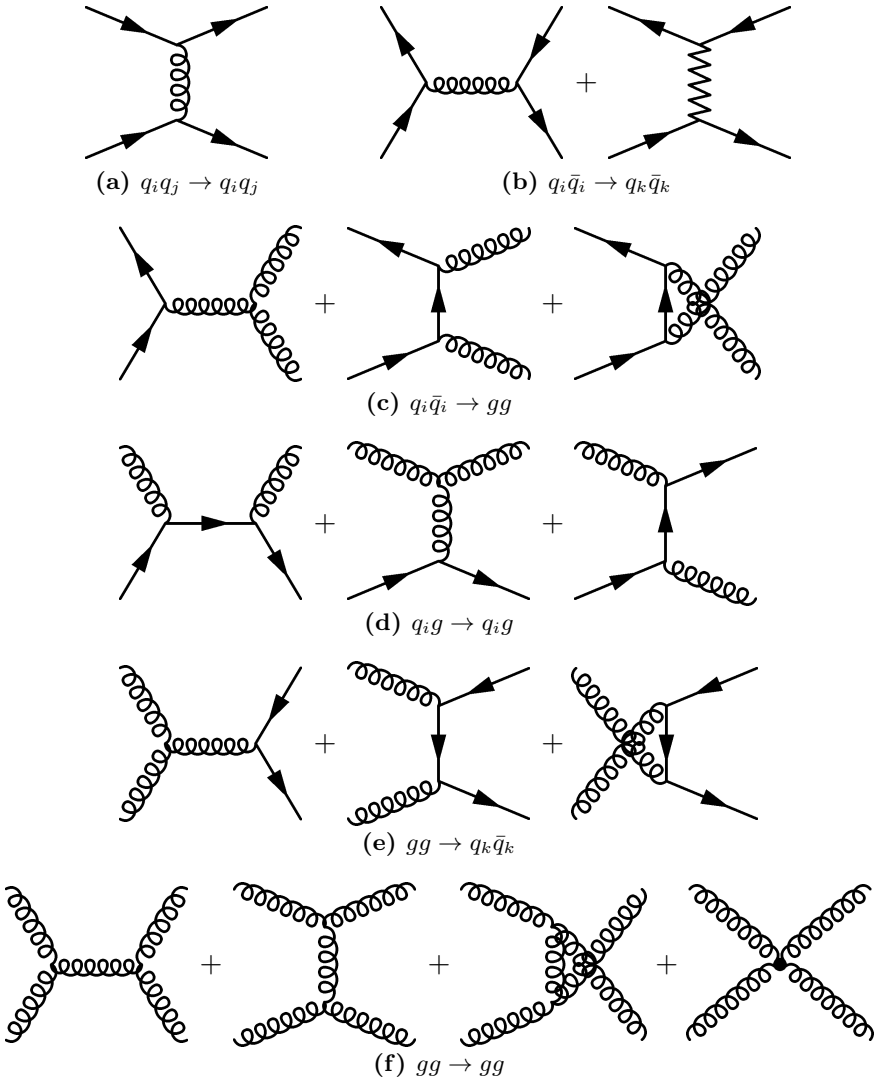

Figure 4.2: Examples of LO diagrams for the hard processes enabled in PYTHIA 6 dijet sample production. The indices i, j, k stand for possibly different flavours. In case the indices are the same, the corresponding u-channel processes must also be accounted for i.e. switching the FS momenta yields another valid configuration. The four gluon vertex is marked with a dot to avoid confusion with two crossing gluon lines.

4.2.3 Event selection

At the MC generator level, we have cut the hard process transverse momentum into the phase-space window $\hat{p}_{\mathrm{T}} \in [5, 980]$ GeV as was done in [56]. Any resulting jets with $p_{\mathrm{T}}^{\mathrm{gen}} < 6$ GeV are dropped already by FastJet and are not stored into tuples. Complete jet reconstruction is done only at the last stage of the analysis, which is performed in ROOT. At this level we raise the jet minimum p_{T} threshold by requiring all jets in both samples to have a p_{T} above 6 GeV, as reconstructed using the R^{MC} Single-Particle Responses (SPR) described in subsection 4.3.1. Note that in general we expect the reconstructed jets to have less p_{T} than the generator level jets.

To find the tag photon in the γ+jet sample, we take the highest-p_{T} photon in the event as the leading γ and demand $p_{\mathrm{T},\gamma}^{\mathrm{MC}} > 7$ GeV. To ensure the isolation of the tag photon already at generator level, we demand

$$\frac{E_{\Delta\mathcal{R}<0.4}^{\mathrm{tot}} - E_{\Delta\mathcal{R}<0.2}^{\mathrm{EM}}}{E_{\Delta\mathcal{R}<0.2}^{\mathrm{EM}}} < 0.07, \tag{4.1}$$

where the superscript tot refers to the total scalar sum of generator level particle energies and the subscript denotes the distance from the tag photon up to which this summation is performed. The superscript EM stands for an approximation of the energy left in the EMCAL. At generator level, this is obtained by summing all photon and charged particle energies and half of other particle energies. Further, we require

$$\frac{E_{\Delta\mathcal{R}<0.3}^{\mathrm{EM}}}{E_{\Delta\mathcal{R}<0.3}^{\mathrm{tot}}} > 0.96 \tag{4.2}$$

and that the sum of charged particle $p_{\mathrm{T}}^{\mathrm{gen}}$ in an annulus of $0.05 < \Delta\mathcal{R} < 0.7$ is less than 1.0 GeV. After these checks, we simulate the experimental fact that the detector does not record a single photon but a cluster in the EM-calorimeter by adding the EM energy within $\Delta\mathcal{R} < 0.4$ to the tag, should there be some surviving the isolation. The event is accepted if it contains exactly one such isolated EM-cluster and if the cluster is within $|\eta| < 1.0$.

To find the probe in the γ+jet sample, we require that there is only one jet with $p_{\mathrm{T,probe}}^{\mathrm{MC}} > 6.0$ GeV and $|\eta_{\mathrm{probe}}| < 0.4$. An additional jet is however tolerated in case it is within $|\Delta\mathcal{R}| < 0.2$ of the EM-cluster, implying that the prompt photon was reconstructed as a jet. In the EM+jet sample, there must be exactly two jets within $|\eta| < 0.4$. The requirements set above for probe objects apply for both jets.

For both samples, we require the tag and probe objects to be back-to-back so that they have an azimuth angle difference of $\Delta\phi$(tag,probe) > 3.0 rad. Furthermore, we

implemented the MET cuts given in [64]

$$\begin{cases} \not\!\!E_T < 2.0 p_{\mathrm{T,tag}}^{\mathrm{MC}}, & p_{\mathrm{T,tag}}^{\mathrm{reco}} < 15 \text{ GeV} \\ \not\!\!E_T < 1.2 p_{\mathrm{T,tag}}^{\mathrm{MC}}, & 15 \text{ GeV} < p_{\mathrm{T,tag}}^{\mathrm{reco}} < 25 \text{ GeV} \\ \not\!\!E_T < 1.1 p_{\mathrm{T,tag}}^{\mathrm{MC}}, & 25 \text{ GeV} < p_{\mathrm{T,tag}}^{\mathrm{reco}} < 50 \text{ GeV} \\ \not\!\!E_T < 0.9 p_{\mathrm{T,tag}}^{\mathrm{MC}}, & p_{\mathrm{T,tag}}^{\mathrm{reco}} > 50 \text{ GeV} \end{cases}$$

and demand $\not\!\!E_T / p_{\mathrm{T,probe}}^{\mathrm{MC}} < 0.7$.

4.3 Jet energy scale determination

The behaviour of a jet depends on whether it originates from a gluon or a quark. In the latter case, also the flavour of the initiating quark matters. We therefore separate jets into three categories and refer to these categories by the term *jet flavour*: g-jets originating from gluons, b-jets from bottom quarks and lq-jets from light quarks. We consider u, d, s and c as light quarks. Note that there are no t-hadrons since the top quark decays before hadronization, and the jet that is eventually formed is to be considered as a jet originating from the decay product. Therefore, we do not consider jets to originate from top quarks at Tevatron's COM collision energies. The jet flavour has to be taken into account when correcting jets to get MC corresponding to data. We shall therefore focus our attention to the Jet Energy Scale (JES) determination methods used for determining flavour-dependent jet energy corrections at the DØ experiment.

4.3.1 Single-particle response functions

The DØ single-particle responses are based on a full GEANT [65] simulation of the DØ detector. The procedure is to simulate the detector's response to single-particle samples [56]. A functional form is then fitted into the histograms depicting how large a fraction of a particle's energy was successfully captured by the detector, as a function of the particle's energy [41, 40]. Aside from fixing a typographical error in the electron and photon response functions[1] we use the photon, electron, muon and hadron response functions given in [40]. The photon response reads

$$R_\gamma^{\mathrm{MC}} = \frac{p_\gamma^{(0)}}{4} \left[1 + \mathrm{Erf}\left(\frac{E + p_\gamma^{(1)}}{\sqrt{2} |p_\gamma^{(2)}|} \right) \right] \left[1 + \mathrm{Erf}\left(\frac{E + p_\gamma^{(3)}}{\sqrt{2} |p_\gamma^{(4)}|} \right) \right] + p_\gamma^{(5)}, \tag{4.3}$$

where

$$\mathrm{Erf}(a) = \frac{2}{\sqrt{\pi}} \int_0^a e^{-x^2} dx.$$

[1] The plots in [41, 40] however agree with the ones obtained by using the functions in the form that we have written here.

For electrons and positrons, we use

$$R_{e^\pm}^{\mathrm{MC}} = \frac{p_{e^\pm}^{(0)}}{4}\left[1+\mathrm{Erf}\left(\frac{E+p_{e^\pm}^{(1)}}{\sqrt{2}|p_{e^\pm}^{(2)}|}\right)\right]\left[1+\mathrm{Erf}\left(\frac{E+p_{e^\pm}^{(3)}}{\sqrt{2}|p_{e^\pm}^{(4)}|}\right)\right] \tag{4.4}$$

if $p_{\mathrm{T}}^{\mathrm{gen}} > 0.3$ GeV and 0 if $p_{\mathrm{T}}^{\mathrm{gen}} < 0.3$ GeV. The muon and anti-muon response is given by

$$R_{\mu^\pm}^{\mathrm{MC}} = \left(p_{\mu^\pm}^{(0)} + E\cdot p_{\mu^\pm}^{(1)}\right)\mathrm{Landau}\left(E, p_{\mu^\pm}^{(2)}, p_{\mu^\pm}^{(3)}\right), \tag{4.5}$$

if $p_{\mathrm{T}}^{\mathrm{gen}} > 0.3$ GeV and 0 if $p_{\mathrm{T}}^{\mathrm{gen}} < 0.3$ GeV. Here we refer to the probability density function of the Landau distribution such that

$$\mathrm{Landau}(x,\mu,\sigma) \equiv P_{\mathrm{Landau}}((x-\mu)/\sigma) = \frac{1}{2\pi i}\int_{a-i\infty}^{a+i\infty} e^{s(x-\mu)/\sigma + s\ln(s)}ds$$

for any $a \in \mathbb{R}_+$, which is to say that the integration may be performed over any path parallel to the imaginary axis. The muon response is due to energy loss in ionization and is therefore typically described in terms of a Landau distribution or Bethe-Fano theory. For more details, see e.g. [66, 67]. Neutrinos are not expected to be observed, so their response is set to zero. For hadrons, we use the response

$$R_h^{\mathrm{MC}} = p_h^{(0)}\left(1 - p_h^{(1)}(4E/)^{p_h^{(2)}-1}\right) \tag{4.6}$$

if $p_{\mathrm{T}}^{\mathrm{gen}} > p_{\mathrm{T}}^{\mathrm{min}}$ and 0 if $p_{\mathrm{T}}^{\mathrm{gen}} < p_{\mathrm{T}}^{\mathrm{min}}$. Here $p_{\mathrm{T}}^{\mathrm{min}} = 0.3$ GeV for run IIa and $p_{\mathrm{T}}^{\mathrm{min}} = m_h$ for run IIb, as in [41, 40]. The power law behaviour is expected by the phenomenology of the calorimeter showers formed by particles hitting the detector material [68]. Physically, it is reasonable to demand that particles must have energies greater than their rest masses to get non-zero response values. Ideally, this feature should be taken care of by the SPR parametrization, at least approximately. The additional cut on particle $p_{\mathrm{T}}^{\mathrm{gen}}$ is to say that the particle must have sufficient transverse momentum to actually reach and trigger a detector, which might not always be the case even if the particle has sufficient energy to exist with on-shell mass. For example a particle in the transverse plane has $|\vec{p}|^2 = p_{\mathrm{T}}^2$ and is considered observed if $E^2 = p_{\mathrm{T}}^2 + m^2 > 2m^2 \Leftrightarrow E > \sqrt{2}m$. This demand acts as a safeguard in case the SPR parametrization would give non-physical low-energy responses.

For run IIb, DØ used two different SPR sets: a default set similar to run IIa and another set with a P20ToP17-correction. The latter is based on a W-mass style MC [40] and its use is due to a change in the interpretation of the detector data level raw jet energy during run IIb: it was taken to be higher than on run IIa. This can be seen as an overall rise of approximately 8% in the p_{T}-balance detector data points between runs IIa and IIb despite MC has shifted only little. This is illustrated in Fig. 4.3. A careful examination of the analysis notes [41, 40] has lead to the understanding that, for run IIb, DØ used a p_{T}-balance variable of the form

$$\frac{p_{\mathrm{T,probe}}^{\mathrm{MC}}}{p_{\mathrm{T},\gamma}^{\mathrm{MC}}}\frac{\sum_i R_i^{\mathrm{data}}E_i}{\sum_j R_j^{\mathrm{MC}}E_j} \tag{4.7}$$

where R_i^{data} is reconstructed using the P20ToP17 SPR, but the denominator using default SPR parameters. Hence, setting the fit parameters to $(A, B, C) = (1, 0, 1)$ will not yield F identically 1 for run IIb. For run IIa it would, since it had only one set of SPR parameters. In the low-$|\eta|$ regime, Eq. (4.7) is equivalent to reconstructing the tag with the default photon parameters and the probe using the P20ToP17-corrected SPR in calculating the vertical axis' p_{T}-balance variable, which was our approach.

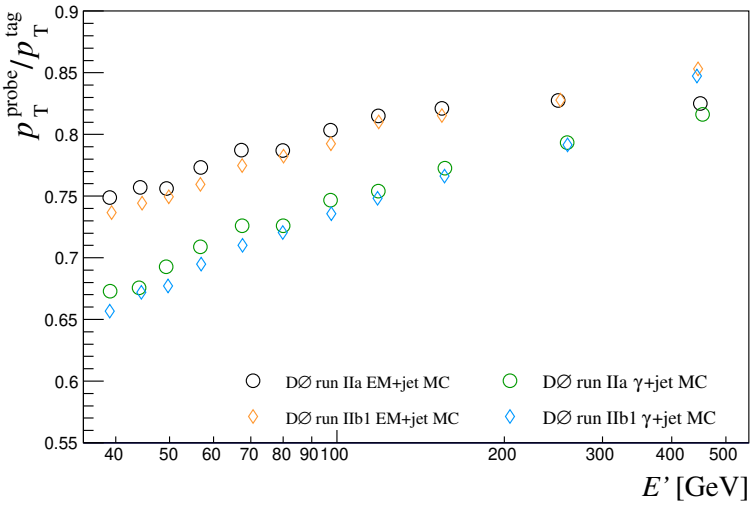

(a) DØ MC

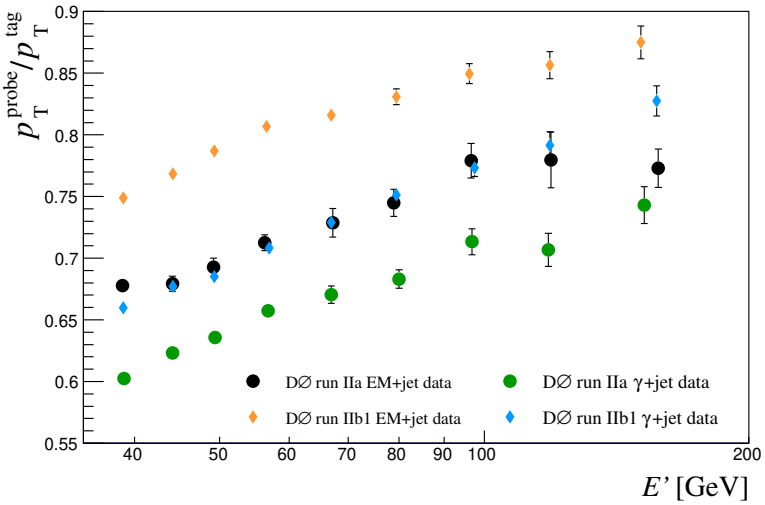

(b) DØ detector data to fit to

Figure 4.3: DØ MC simulation and detector data points for run IIa [41] and IIb1 [40]. The small shift in MC amounts to slightly different SPR parametrizations and statistical effects. The larger shift in detector data is due to a change in the interpretation of the tag and probe scales at DØ [40]. Note that the plots have different axis ranges.

Along with the functional forms, we obtained the values of the parameters $p^{(i)}$ for photons (γ), electrons (e), muons (μ), charged pions ($\pi^{\pm}$), charged kaons ($K^{\pm}$), short-lived (K^0_S) and long-lived (K^0_L) neutral kaons, Lambdas (Λ), neutrinos (n) and protons (p) from the analysis notes [41, 40]. Some of the resulting SPR functions are displayed in the region $|\eta| < 0.1$ in Fig. 4.4. The parameters are included also for further $|\eta|$ regions in appendix A for reference.

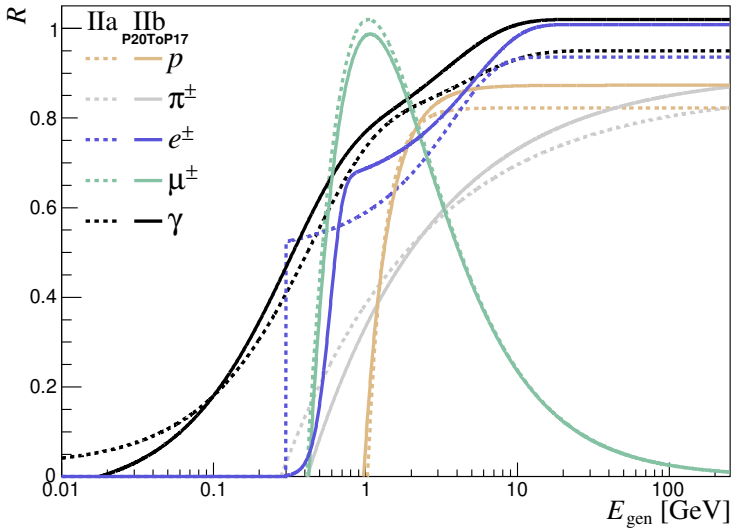

Figure 4.4: An illustration of the behaviour of the SPR functions of Eq.s (4.3), (4.4), (4.6) and (4.5) in the innermost $|\eta|$ region. Due to different hadrons' responses overlapping largely with each other, only proton and charged pion responses are displayed here for clarity. The dashed lines are plotted using the parameters for DØ run IIa and the solid lines using those for DØ run IIb. Both sets of parameters are presented in appendix A.

In addition to the particles listed above, Pythia 6 and Herwig 7 produce also Σ^-, Σ^0, Σ^+, Ξ^-, Ξ^0 and Ω^- at the $c\tau = 10$ mm lengthscale setting. We chose this $c\tau$ value based on the discussion in [69], although the value used at DØ was left unknown. However, one should note that DØ did report SPR parameters for the K^0_S mesons in [41, 40]. Based on the average lifetimes [21], the K^0_S should be no longer present in the produced samples if $c\tau$ was set high enough for the strange baryons in the above list to decay. This is due to Pythia 6 decaying all particles whose average lifetimes are below the given $c\tau$. We experimented with several $c\tau$ values before settling to 10 mm as no alternative provided a satisfactory solution to this problem. It remains unclear if the DØ jet energy scale determination was done using some parameters for the strange baryons or not, as they were not included in [41, 40]. Since these particles are hadrons, we reconstruct them with an Ansatz based on Eq. (4.6). We use the $\pi^{\pm}$ SPR parameters of the appropriate epoch as the basis of the Ansatz, as some earlier JES analyses have been performed using only the charged pion SPR [70]. However, we introduce the physically motivated demand that the response tends to zero at rest mass energies, similar to most of the

P20ToP17-corrected SPR functions shown in Fig. 4.4. As can be seen from Eq. (4.6), the role of $p_h^{(0)}$ is mainly to scale the value R approaches at high E. Hence we proceed by making $p_h^{(1)}$ and $p_h^{(2)}$ dependent on each other in a way that incorporates the strange baryon's mass m_{sb} in determining the low-energy behaviour. Thus we demand

$$R_{sb}^{\mathrm{MC}}(E = m_{sb}) = 0 \quad \Leftrightarrow \quad p_{sb}^{(0)} \left(1 - p_{sb}^{(1)} (4m_{sb}/3)^{p_{sb}^{(2)}-1}\right) = 0, \tag{4.8}$$

which yields

$$p_{sb}^{(1)} = (4m_{sb}/3)^{1-p_{sb}^{(2)}}. \tag{4.9}$$

The rest of the parameters remain the same as for $\pi^{\pm}$, so that $p_{sb}^{(0)} = p_{\pi^{\pm}}^{(0)}$ and $p_{sb}^{(2)} = p_{\pi^{\pm}}^{(2)}$. We use this Ansatz for determining the responses of all the extraneous strange hadrons. Example graphs of the resulting functions are shown in in Fig. 4.5.

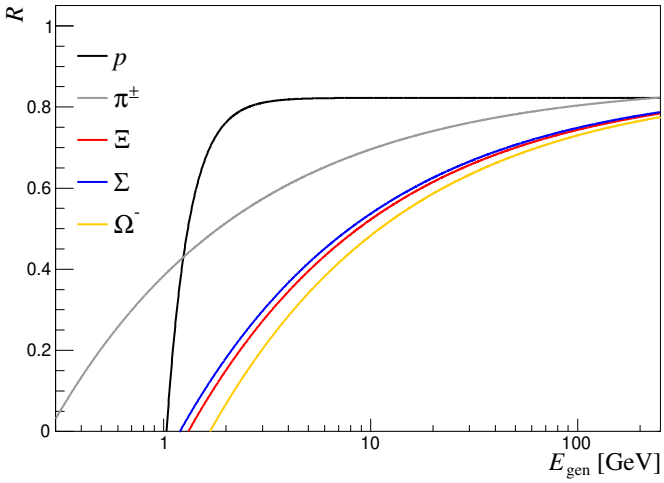

Figure 4.5: Ansätze for the Σ, Ξ and Ω^- SPR functions based on run IIa pion parameters. The various Σ baryons are closely grouped and the Ξ baryons are in the vicinity of each other as well. Therefore only one band is drawn for each type. The p and $\pi^{\pm}$ SPR are shown for reference.

4.3.2 Flavour-dependent jet energy corrections

Following DØ, we compute the p_{T}-balance as a function of the jet energy estimator $E' = p_{\mathrm{T,tag}}^{\mathrm{MC}} \cosh(\eta_{\mathrm{probe}})$. This is due to the $p_{\mathrm{T,tag}}$ and η_{probe} being easier to measure precisely than the E_{probe} itself [56].

We shall refer to the level of reconstruction resulting from the application of the default DØ SPR parameters for R^{MC} as the MC-level. This label shall appear as a superscript in the reconstructed quantities when otherwise not clear from context. For run IIb, there is also the possibility of using the P20ToP17 corrected parameters, and [40] refers to these with the label MC′. We shall adopt this notation when explicitly needed. We also use the label gen to denote a level of reconstruction where all particles' 4-momenta

are taken at the values output by the MC generator. However, the neutrinos and muons are dropped from the jets even at gen level due to being reconstructed poorly at best in the SPR formalism. Our choices and notations aim to follow the logic of [56, 41, 40].

The method of reconstructing jets from their constituents via the SPR is based on the assumption that a jet's p_{T} is approximately equal to a vector sum of its particles. Also the GEANT simulation may not account for all detector inhomogeneities and aging effects. Thus the MC-level may not exactly agree with the data. This difference is covered by introducing additional fit parameters A, B, C to the hadron SPR such that

$$R_h^{\mathrm{data}} = C p_h^{(0)} \left(1 - A p_h^{(1)} (4E/3)^{p_h^{(2)}+B-1}\right) \tag{4.10}$$

if $p_T^{\mathrm{gen}} > p_{\mathrm{T}}^{\mathrm{min}}$ and 0 otherwise. For other particles, we assume that $R^{\mathrm{data}} = R^{\mathrm{MC}}$. The jet energy correction factor is then found from the ratio [56]

$$F = \frac{\sum_{i \in \{\substack{\mathrm{Particles} \\ \mathrm{in\ jet}}\}} E_i R_i^{\mathrm{data}}(E_i)}{\sum_{j \in \{\substack{\mathrm{Particles} \\ \mathrm{in\ jet}}\}} E_j R_j^{\mathrm{MC}}(E_j)}. \tag{4.11}$$

To make the correction flavour-dependent, the factors F are calculate as separate histograms depending on the flavour of the initial parton associated with the jet. Repeating the DØ method, we divide the jets into b-jets (b-quark initiated), g-jets (gluon-initiated) and (u, d, s, c)-jets (originating from light quarks, sometimes denoted lq). The relative correction factor that is used for bringing simulated jets to data level is obtained by normalizing Eq. (4.11) by the average F for all jet flavours in the γ+jet sample [56]

$$F_{\mathrm{corr}} = \frac{F}{\langle F \rangle_{\gamma+\mathrm{jet}}}. \tag{4.12}$$

The DØ data points to which we fit our simulations to are extracted from [41, 40] using the WebPlotDigitizer software provided by [71], whenever not available for extraction in the source of [56].

4.3.3 The binning variable of F profiles and shifting to reconstructed jet p_{T} level

The analysis notes [41, 40] report the F and F_{corr} histograms ambiguously as a function of a variable denoted by $p_{\mathrm{T}}^{\mathrm{jet}}$. It was left unclear which reconstruction level this refers to: generator level, reconstruction using R^{MC}, R^{data} or something else resulting for instance from the use of a conversion factor. On the other hand, the jet energy estimator $E' \propto p_{\mathrm{T,tag}}^{\mathrm{MC}}$ was introduced due to the probe jet energy being measured less precisely than the tag p_{T}. It would hence seem consistent to find also F as a function of E' or some other quantity related to the energy or momentum of the tag and later apply an approximative mapping from that variable to probe p_{T}. This question is important since

the flavour fractions don't generally agree. This will consequently affect how the sample average is calculated and how the F_{corr} will end up. The choices made here are done in pursuit of reproducing the DØ F_{corr} as accurately as possible when plugging their fit parameters A, B, C into our MC simulations. The best agreement was obtained by finding F first as a function of $p_{\text{T,probe}}^{\text{gen}}$. Then $p_{\text{T}}^{\text{gen}}$ is transformed to the average SPR reconstructed[2] $p_{\text{T}}^{\langle\text{MC}\rangle}$ by the linear map shown in Fig. 4.6. The values of each bin in the F profiles is shifted in the vertical direction, leaving the horizontal bin locations unchanged. The shift is done by fitting a power law with the parametrization

$$P^{(0)}\left(1 - P^{(1)}(p_{\text{T}})^{P^{(2)}-1}\right), \tag{4.13}$$

into the F histograms and incrementing or decreasing a bin's F value by the difference of the fitted function's values at the original $p_{\text{T}}^{\text{gen}}$ value and at the shifted p_{T} value. The P^i are fit parameters. The shifting procedure is performed in this manner for ease of recalculating the shifted γ+jet sample average $\langle F\rangle_{\gamma+\text{jet}}$, which requires keeping track of the fractions of jets of each flavour at each bin's p_{T} value.

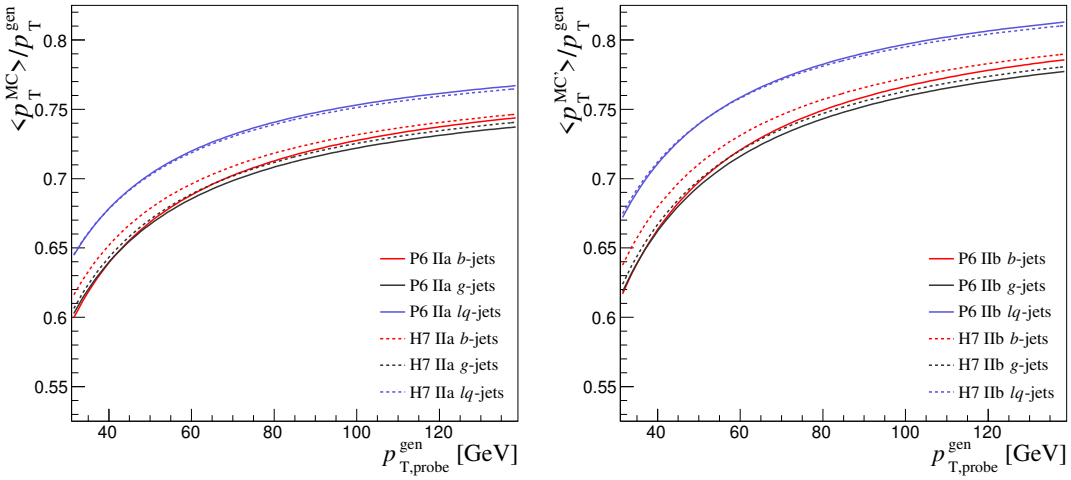

(a) Run IIa **(b)** Run IIb

Figure 4.6: The relation of generator level jet p_{T}, with muons and neutrinos excluded, to the jet p_{T} reconstructed using R^{MC} for run IIa and the P20ToP17-corrected $R^{\text{MC}'}$ for run IIb. As we are not using R^{data} and the SPR parameters agree for all run IIb epochs, these ratios suffice to describe the p_{T} conversions for all run II epochs. Notice however that in order to enhance readability we have plotted $\langle p_{\text{T}}^{\text{MC}}\rangle/p_{\text{T}}^{\text{gen}}$ vs. $p_{\text{T}}^{\text{gen}}$ instead of the $\langle p_{\text{T}}^{\text{MC}}\rangle$ vs. $p_{\text{T}}^{\text{gen}}$ actually used for the mapping.

Once the F_{corr} histograms have been found, we calculate an average of the EM+jet and

[2]For run IIa we use the default SPR parameters and for IIb the P20ToP17 corrected ones to do the conversion. In DØ notation, the latter would correspond to $\langle p_{\text{T}}^{\text{MC}'}\rangle$.

γ+jet histograms. A power law function of the form given in Eq. (4.13) is fitted into the resulting average F_{corr} histogram for each run II epoch. The fitted power law functions are then imported into further analyses, such as those of m_t.

4.3.4 Fitting MC simulation to detector data

The fitting problem to be solved for finding the parameters A, B, C involves looping through all the events in a sample. In each event, the SPR functions must be evaluated for all particles individually when filling the p_{T}-balance profile. The nature of the problem then renders many ready-made fit algorithms slow or unusable. Our approach was to implement the Gauss-Newton method and optimize it for this problem. Details are included in appendix B. In this subsection we shall only discuss an important caveat.

Constraining the fit

Considering a fit's success solely as a mathematical problem may yield solutions where C differs notably from the default value of one. This may lead to undesirable behaviour in the SPR functions and/or the flavour-dependent jet energy correction factors to be obtained. Therefore, we constrain C close to 1. This is done by extending the standard form of Eq. (B.3) into

$$\tilde{\chi}^2 = \chi^2 + \frac{1}{\sigma_C^2}(C-1)^2. \tag{4.14}$$

The constraint weight is chosen so that σ_C is the expected the standard deviation of C to be. In our studies, we set $\sigma_C = 0.01$. Recalling that $\partial_C(1-C)^2 = \partial_C(1-2C+C^2) = 2(C-1) = \partial_C(C-1)^2$, differentiating Eq. (4.14) gives the modification's contributions to the gradient as

$$\partial_C\tilde{\chi}^2 = \partial_C\chi^2 + 2\lambda_C(C-1)$$

and the Hessian is modified by

$$\partial_C\partial_C\tilde{\chi}^2 = \partial_C\partial_C\chi^2 + 2\lambda_C.$$

Notice that for all other elements, $\partial_i\tilde{\chi}^2 = \partial_i\chi^2$ and $\partial_i\partial_j\tilde{\chi}^2 = \partial_i\partial_j\chi^2$. This is because the partial derivatives with respect to A and B eliminate the constraint term in (4.14) as it depends only on C.

Chapter 5

Results

In this chapter we present further details on the contents of our MC samples. We then examine some key indicators for our level of success in reproducing the DØ analyses. Finally, we present the results of our p_{T}-balance fits and the flavour-dependent jet energy corrections following from them.

5.1 Probe jet particle composition

The particle composition of the probe jets in our general Pythia 6 γ+jet sample is shown for in Fig. 5.1. Additionally, the same figure gives details on the fractions of the strange baryons for which we had no SPR functions from DØ. The particle compositions of the b-enriched Pythia 6 γ+jet sample and the generic Herwig 7 sample are given in Fig. 5.2. The b-enriched sample was produced in order to enhance b-jet statistics in the determination of the correction factors F, which are shown in section 5.4. Due to computational resources, we do not have b-enriched samples for Herwig 7, but made the general sample twice as large as in the case of Pythia 6.

Here we show only the γ+jet samples at generator level i.e. as output by the MC generator. These suffice to portray the key features, since the composition plots are largely similar in many cases. Appendix C contains a complete collection of similar probe jet particle composition plots for all samples and reconstruction levels.

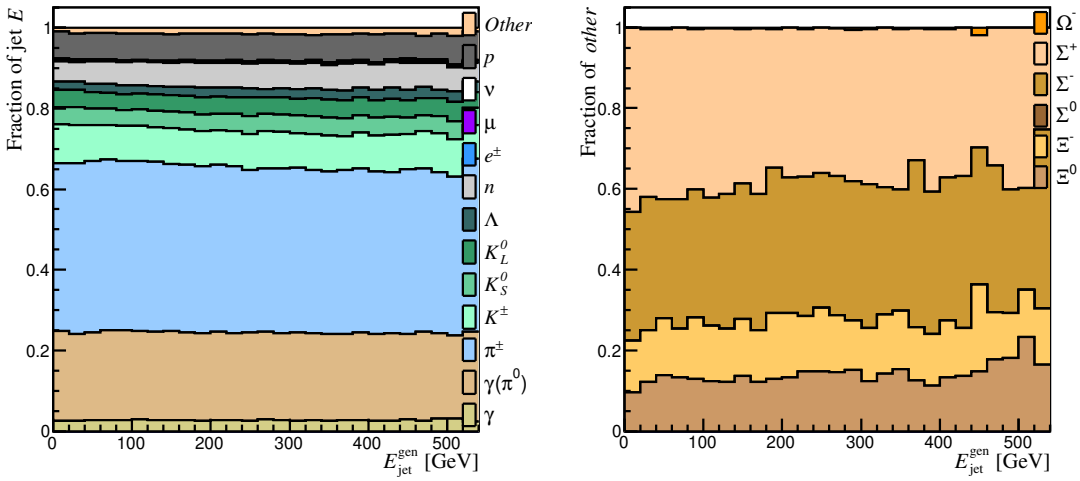

(a) Generic P6 γ+jet sample

(b) Particles labeled *other*

Figure 5.1: Probe jet particle contents in the generic Pythia 6 γ+jet sample.

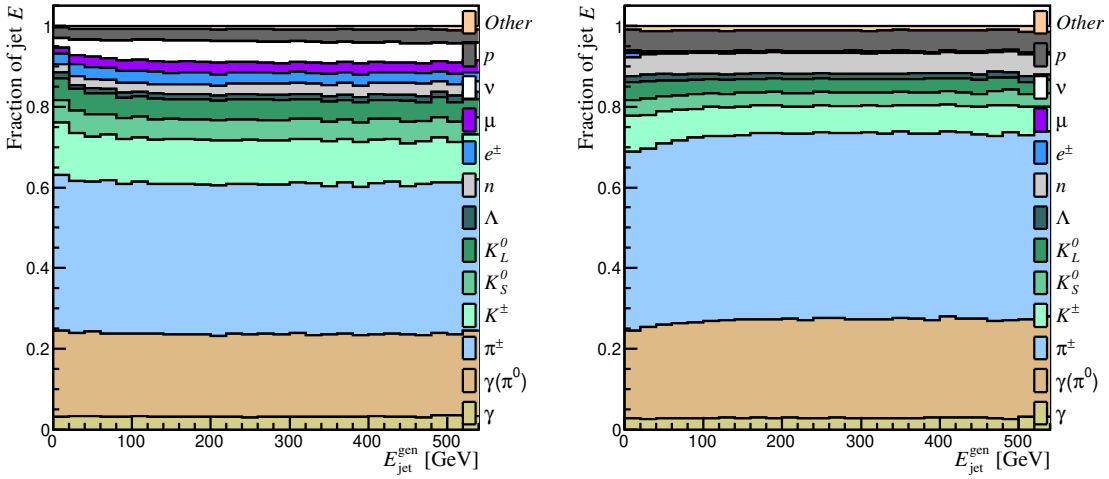

(a) b-enriched P6 γ+jet sample

(b) Generic H7 γ+jet sample

Figure 5.2: Probe jet particle contents in the b-enriched Pythia 6 γ+jet sample and the generic Herwig 7 γ+jet sample.

5.2 Flavour fractions

The fraction of jets originating from partons with different flavour are shown in Fig. 5.3. The fractions are shown for the Pythia 6 and Herwig 7 generators, as well as for the

b-jet enriched Pythia 6 sample.

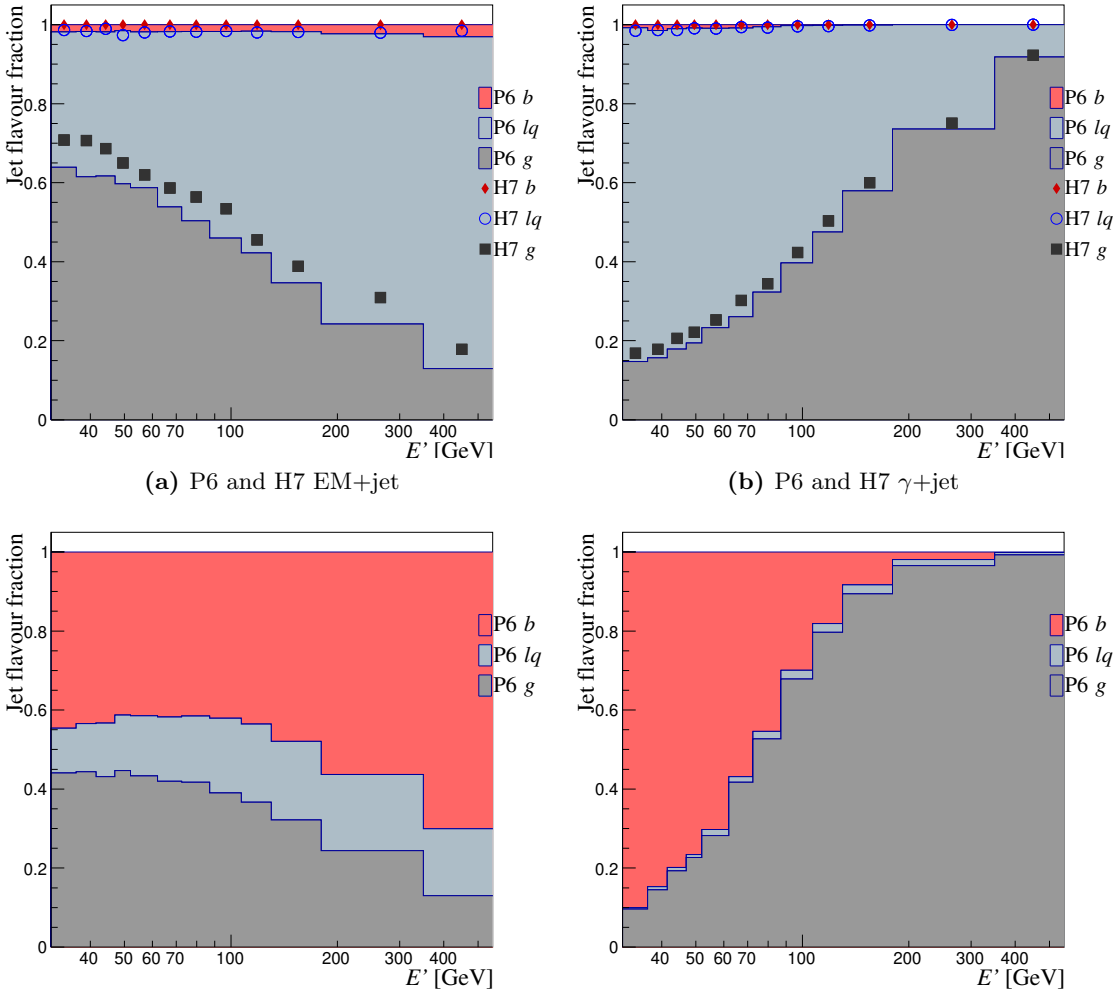

(a) P6 and H7 EM+jet

(b) P6 and H7 γ+jet

(c) P6 EM+jet (b-enriched)

(d) P6 γ+jet (b-enriched)

Figure 5.3: The fractions of events with the probe jet originating from different partons in the Pythia 6 and Herwig 7 EM+jet and γ+jet samples.

5.3 JES determination via the p_{T}-balance method

Here we illustrate the results of our p_{T}-balance studies. First we show the similarity of our MC to DØ MC and that using the DØ fit parameters takes the p_{T}-balance profiles to the vicinity of the DØ detector data points, as should. Lastly, we show our own fits.

5.3.1 Reproducing the DØ p_{T}-balance results

A comparison of the DØ MC p_{T}-balances reported in [41, 56] and our PYTHIA 6 MC is shown in Fig. 5.4 for runs IIa and IIb1. IIb2 and IIb3-4 are included in Appendix D.

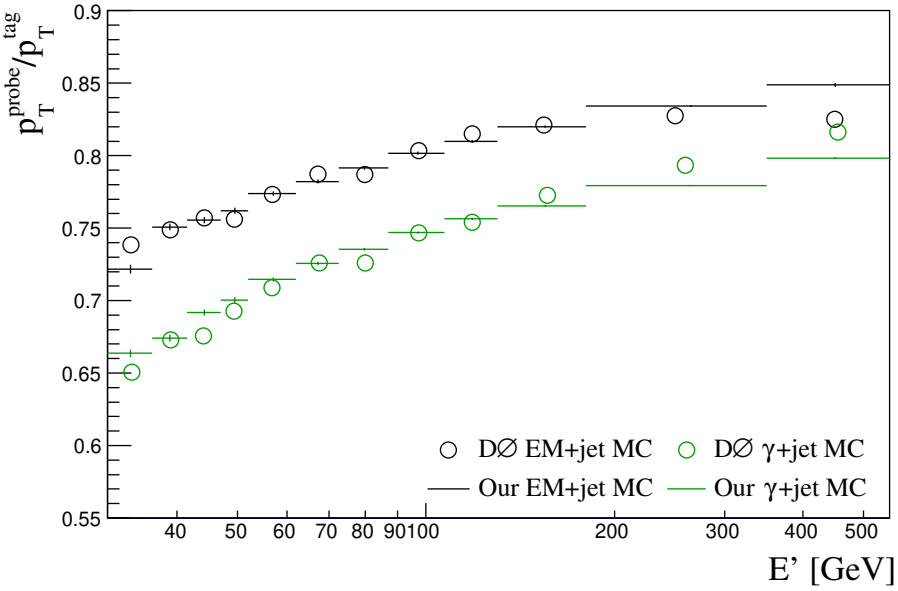

(a) Run IIa

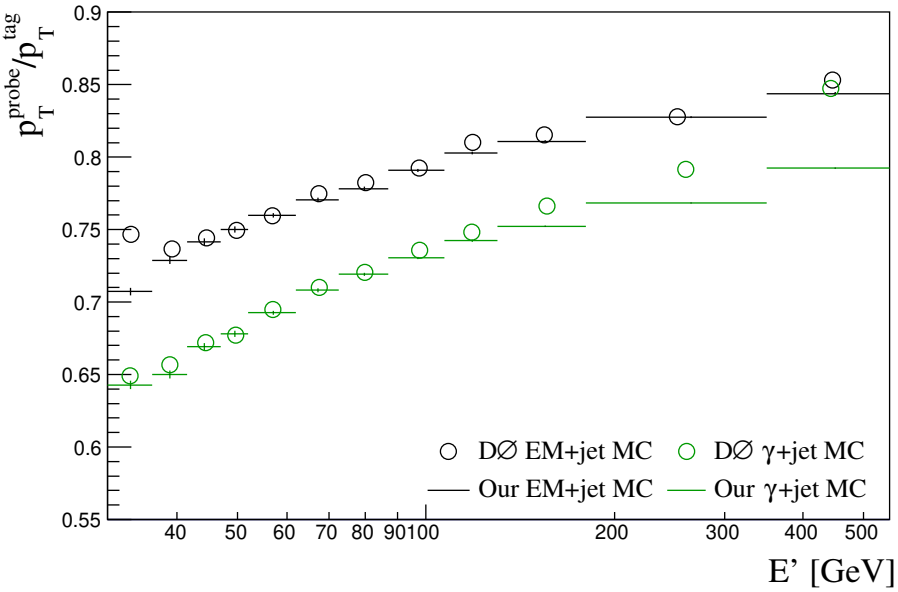

(b) Run IIb1

Figure 5.4: A comparison of DØ MC (open circles) to our MC (histogram lines) reconstructed using R^{MC}.

To check the similarity of our samples to those produced by DØ, we calculate the fit-level p_{T}-balances by using our MC samples and applying the fit parameters reported by DØin [41] for IIa and in [40] for IIb. These are plotted in Fig. 5.5 for the runs IIa and IIb1. For reference, we have listed The DØ fit parameters for all epochs in Table 5.1.

Table 5.1: DØ Pythia 6 fit parameters and uncertainties from [41] for run IIa and from [40] for the run IIb epochs.

	IIa	IIb1	IIb2	IIb3-4
A	1.409	2.1682	1.933	1.469
B	0.0017	-0.310	-0.1611	0.004
C	0.9973	1.0228	1.059	1.073
σ_A	0.02047	0.2854	0.1335	0.050
σ_B	$7.104{\cdot}10^{-3}$	0.1005	0.0571	0.0301
σ_C	0.09297	0.0142	0.0153	0.0143

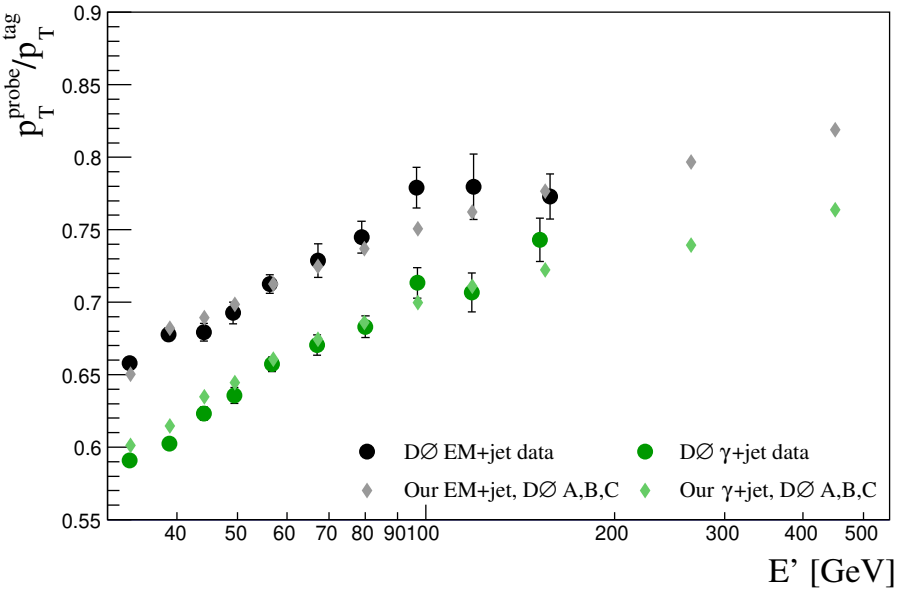

(a) P6 run IIa

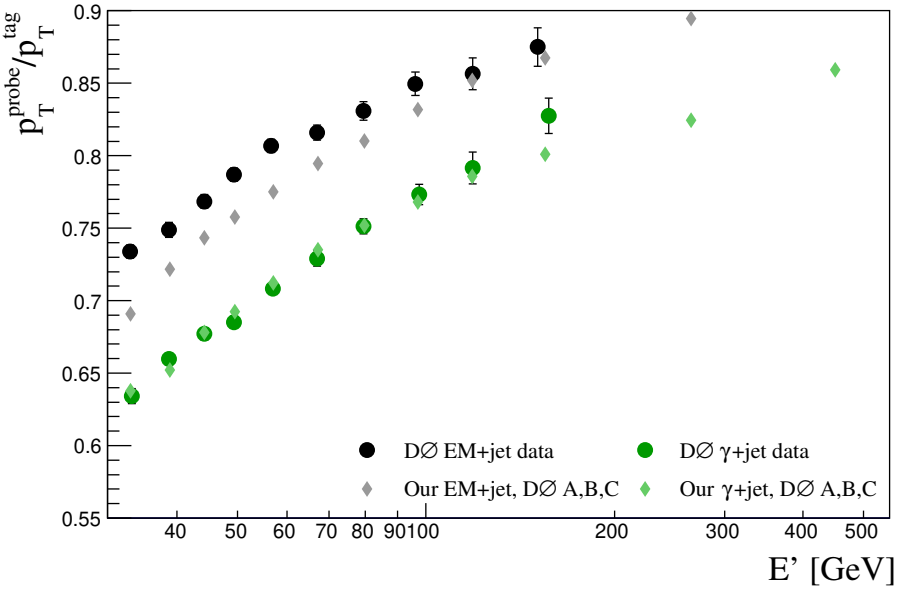

(b) P6 run IIb1

Figure 5.5: A comparison of DØ detector data (filled circles) to our MC reconstructed using R^{data} with DØ fit parameters A, B, C given in [41] for run IIa and in [40] for run IIb (diamonds).

Similar checks were carried out for all run II epochs. The plots for the runs IIb2 and IIb3-4 are included in Appendix D.

5.3.2 Our p_{T}-balance fits

Our p_{T}-balance fits using the Gauss-Newton method are depicted in Fig. 5.6 for runs IIa and IIb1. The resulting fit parameters along with their uncertainties and correlations are shown in Table 5.2 for Pythia 6 and in Table 5.3 for Herwig 7.

Table 5.2: The fit parameters, uncertainties and correlations resulting from our Pythia 6 fits to the different run IIb epoch detector data points.

	IIa	IIb1	IIb2	IIb3-4
A	1.459	1.420	1.752	1.660
B	$3.927{\cdot}10^{-3}$	-0.1290	-0.2412	-0.2132
C	1.004	1.009	1.011	1.008
σ_A	0.05768	0.06349	0.07276	0.06876
σ_B	0.02636	0.03580	0.03740	0.03647
σ_C	$7.049{\cdot}10^{-3}$	$7.034{\cdot}10^{-3}$	$7.012{\cdot}10^{-3}$	$7.014{\cdot}10^{-3}$
σ_{AB}	$-1.436{\cdot}10^{-3}$	$-2.127{\cdot}10^{-3}$	$-2.571{\cdot}10^{-3}$	$-2.356{\cdot}10^{-3}$
σ_{AC}	$-5.931{\cdot}10^{-5}$	$-1.345{\cdot}10^{-4}$	$-2.258{\cdot}10^{-4}$	$-2.056{\cdot}10^{-4}$
σ_{BC}	$8.372{\cdot}10^{-5}$	$1.529{\cdot}10^{-4}$	$1.837{\cdot}10^{-4}$	$1.787{\cdot}10^{-4}$

Table 5.3: The fit parameters, uncertainties and correlations resulting from our Herwig 7 fits to the different run IIb epoch detector data points.

	IIa	IIb1	IIb2	IIb3-4
A	1.236	1.087	1.316	1.221
B	0.02905	-0.06843	-0.1733	-0.1289
C	1.002	1.003	1.003	1.002
σ_A	0.05630	0.05681	0.06262	0.05743
σ_B	0.02969	0.03970	0.04074	0.03864
σ_C	$7.061{\cdot}10^{-3}$	$7.056{\cdot}10^{-3}$	$7.044{\cdot}10^{-3}$	$7.047{\cdot}10^{-3}$
σ_{AB}	$-1.574{\cdot}10^{-3}$	$-2.082{\cdot}10^{-3}$	$-2.363{\cdot}10^{-3}$	$-2.038{\cdot}10^{-3}$
σ_{AC}	$-3.617{\cdot}10^{-5}$	$-8.227{\cdot}10^{-5}$	$-1.480{\cdot}10^{-4}$	$-1.227{\cdot}10^{-4}$
σ_{BC}	$8.550{\cdot}10^{-5}$	$1.551{\cdot}10^{-4}$	$1.874{\cdot}10^{-4}$	$1.750{\cdot}10^{-4}$

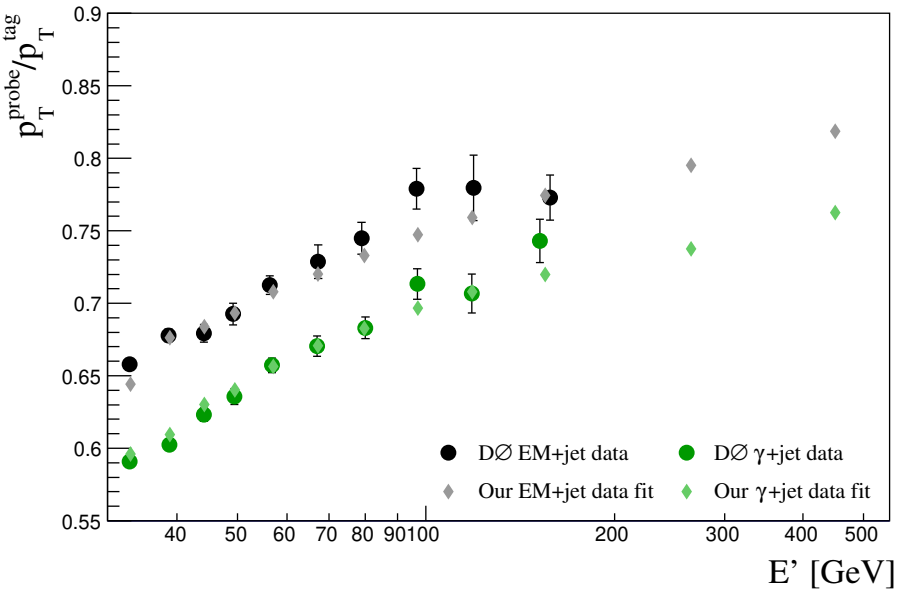

(a) P6 run IIa

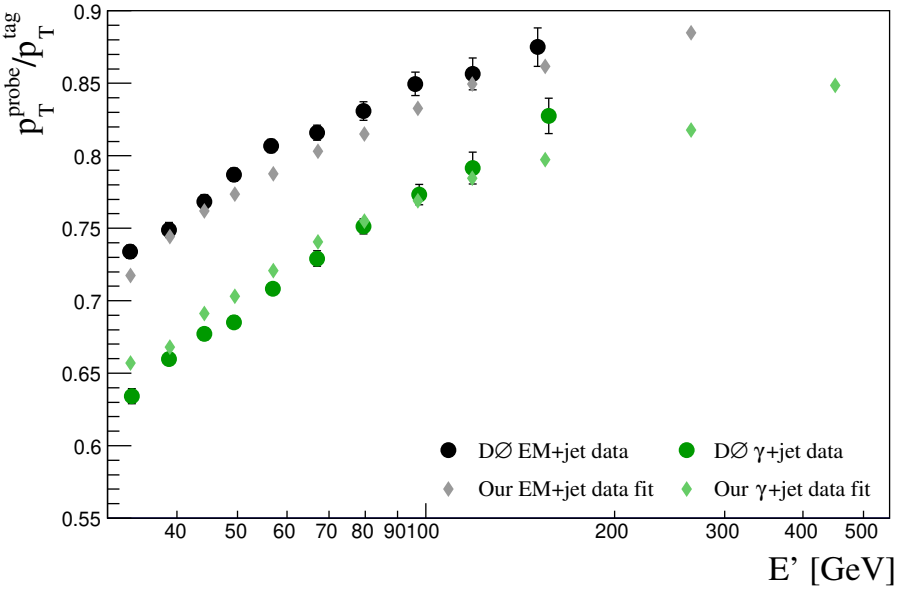

(b) P6 run IIb1

Figure 5.6: Comparison of DØ detector data (filled circles) and our PYTHIA 6 MC reconstructed using R^{data} with our fit parameters A, B, C for runs IIa and IIb1 (filled diamonds).

Fig. 5.7 shows a comparison of our MC level reconstructed HERWIG 7 p_{T}-balance to DØ PYTHIA 6 MC for run IIa and IIb1. The epochs IIb2 and IIb3-4 are included in appendix D. Fig. 5.8 shows our HERWIG 7 fit to DØ detector data for these epochs.

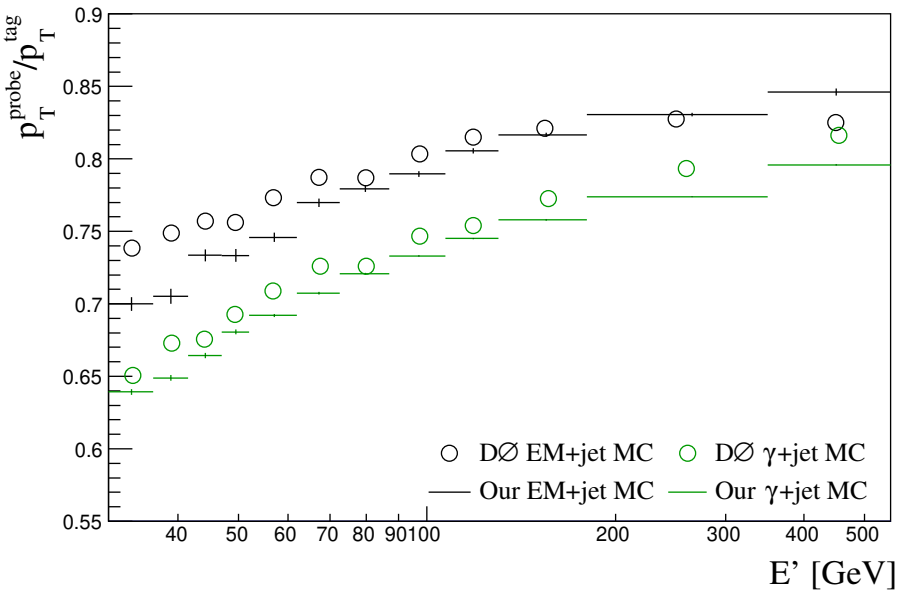

(a) H7 run IIa

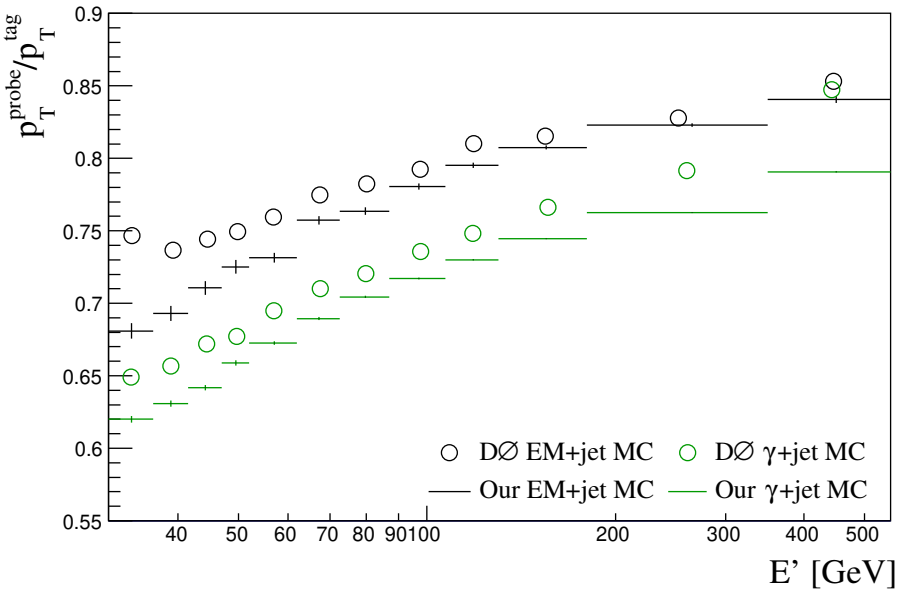

(b) H7 run IIb1

Figure 5.7: Comparison of DØ PYTHIA 6 MC (open circles) to our HERWIG 7 MC reconstructed using R^{MC} (histogram lines) for runs IIa and IIb1.

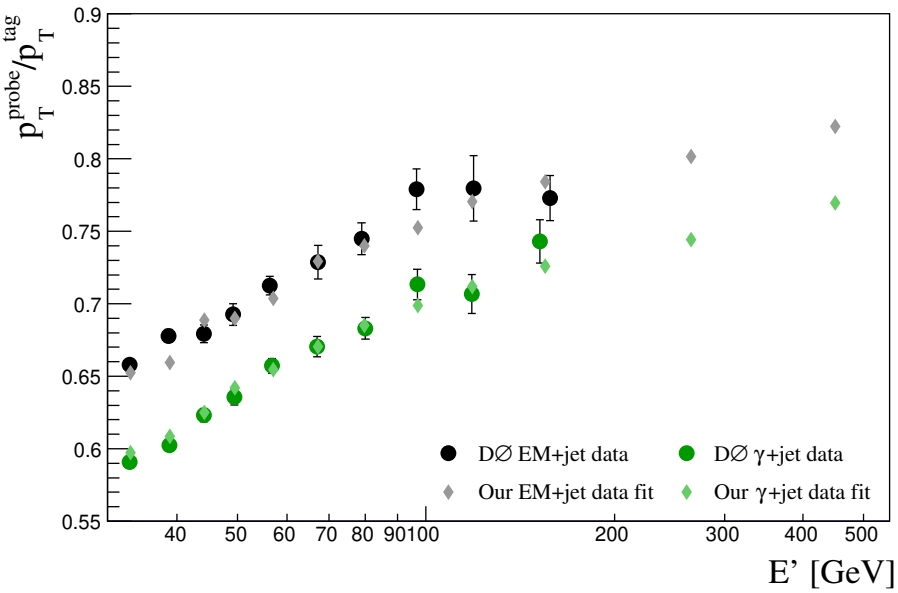

(a) H7 run IIa

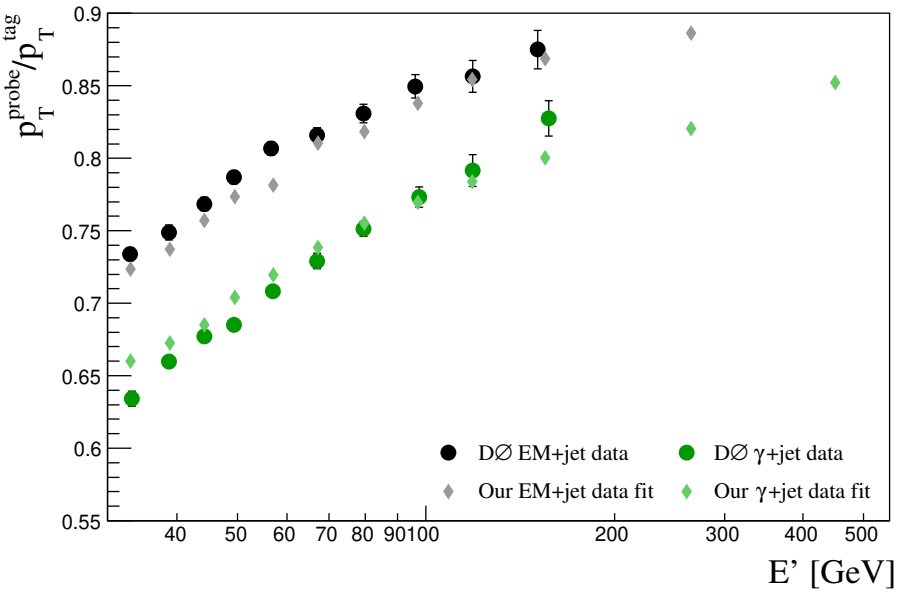

(b) H7 run IIb1

Figure 5.8: Comparison of DØ detector data (filled circles) to our HERWIG 7 MC reconstructed using R^{data} with our fit parameters A, B, C for runs IIa and IIb1.

5.4 Flavour-dependent jet energy corrections

Here we present the correction factors F and F_{corr}. We show both the reproduction of the DØ factors presented in [41, 40] and the factors resulting from our p_{T}-balance fits.

5.4.1 Reproduced DØ results

In Fig. 5.9 we present the F and F_{corr} resulting from applying the DØ A, B, C values of [41] to our MC for the runs IIa and IIb1,. The epochs IIb2 and IIb3-4 are included in Appendix E.

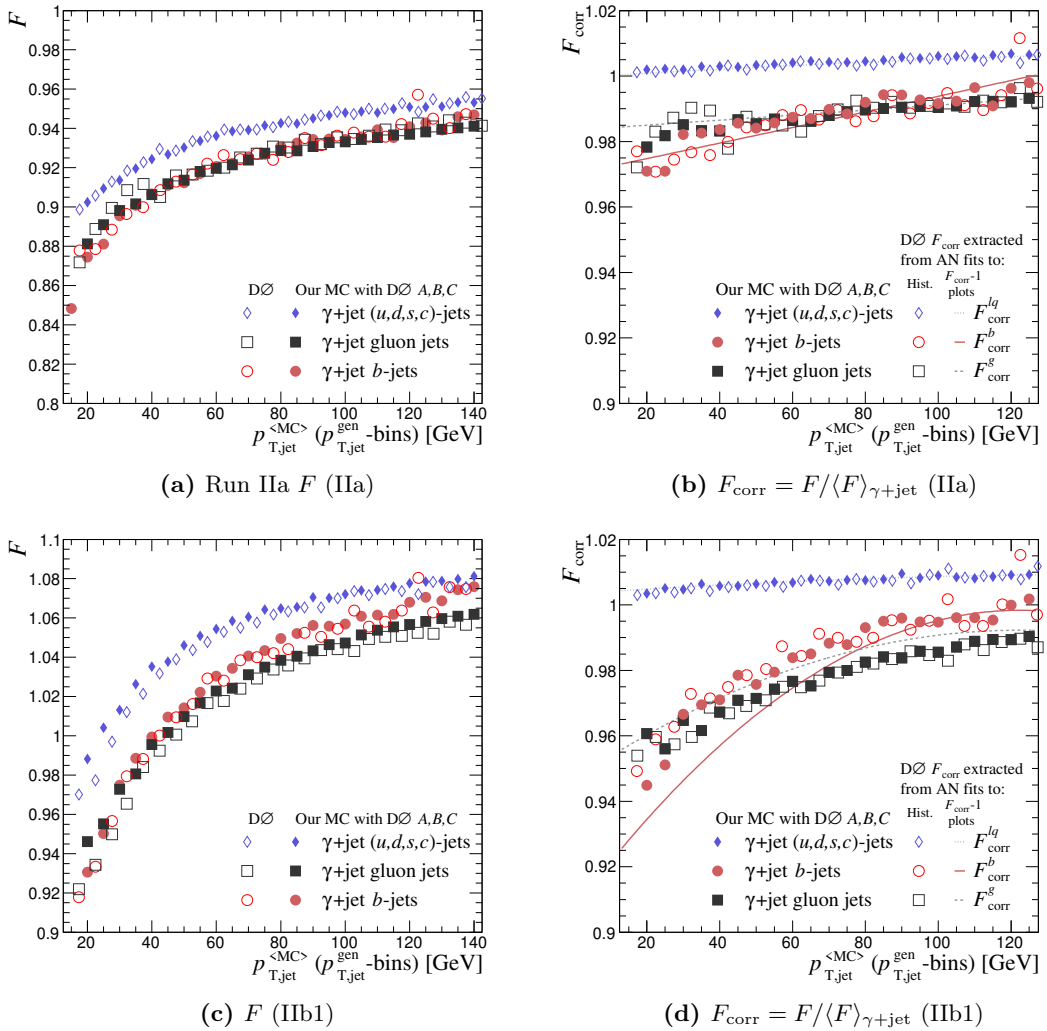

(a) Run IIa F (IIa)

(b) $F_{\text{corr}} = F/\langle F\rangle_{\gamma+\text{jet}}$ (IIa)

(c) F (IIb1)

(d) $F_{\text{corr}} = F/\langle F\rangle_{\gamma+\text{jet}}$ (IIb1)

Figure 5.9: The correction factors F and F_{corr} for different flavours, obtained by applying DØ fit parameters A, B, C given in [41, 40] to our MC. The open markers are DØ histograms and the curves are the DØ fits, both extracted from [41, 40]. The filled markers are our reproduction.

5.4.2 Flavour-dependent jet energy corrections resulting from our fit

The F_{corr} resulting from our fits to DØ detector data points are shown in Fig. 5.10 for Pythia 6 and in Fig. 5.11 for Herwig 7. The plots are produced by averaging over the γ+jet and EM+jet samples for each run II epoch and fitting a power law of the form given in Eq. (4.13) to the resulting average.

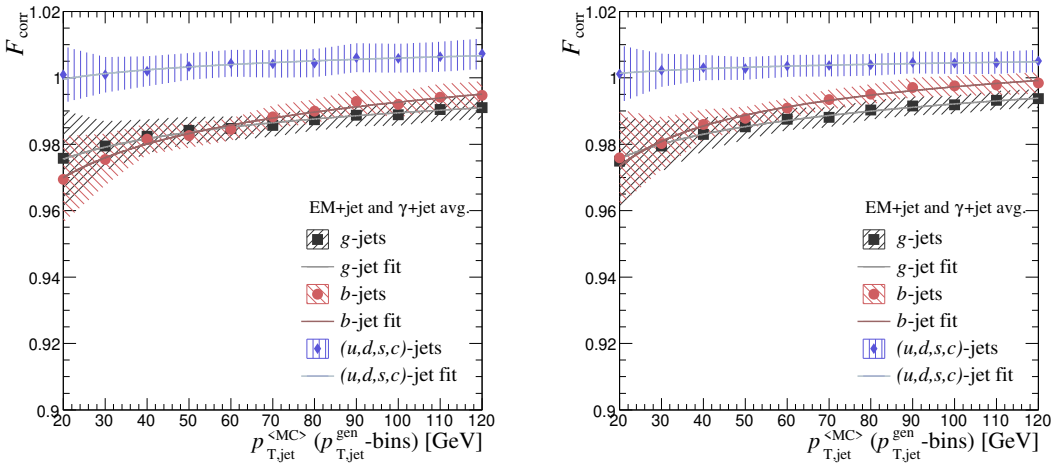

(a) Run IIa **(b)** Run IIb1

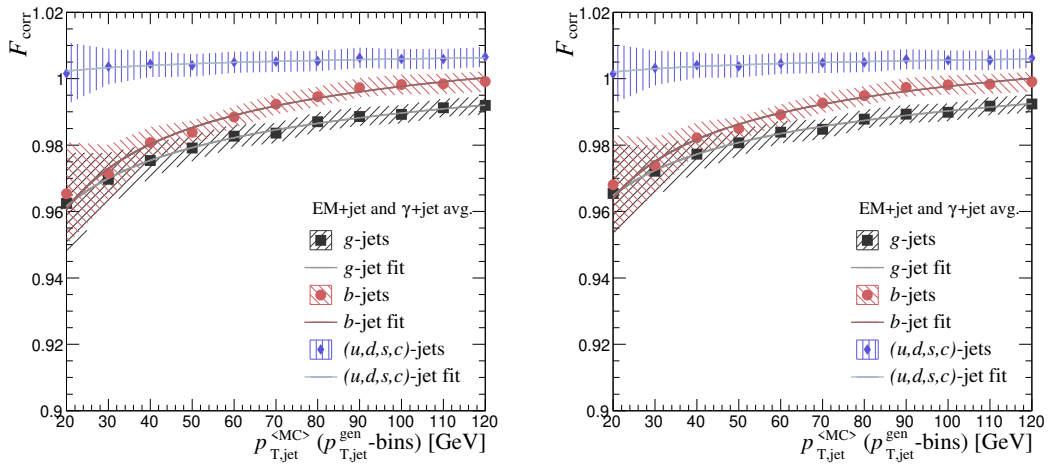

(c) Run IIb2 **(d)** Run IIb3-4

Figure 5.10: F_{corr} resulting from fitting our Pythia 6 MC to the DØ detector data points given in [41] for run IIa and in [40] for run IIb. The shaded bands represent the statistic and systematic uncertainties added in quadrature.

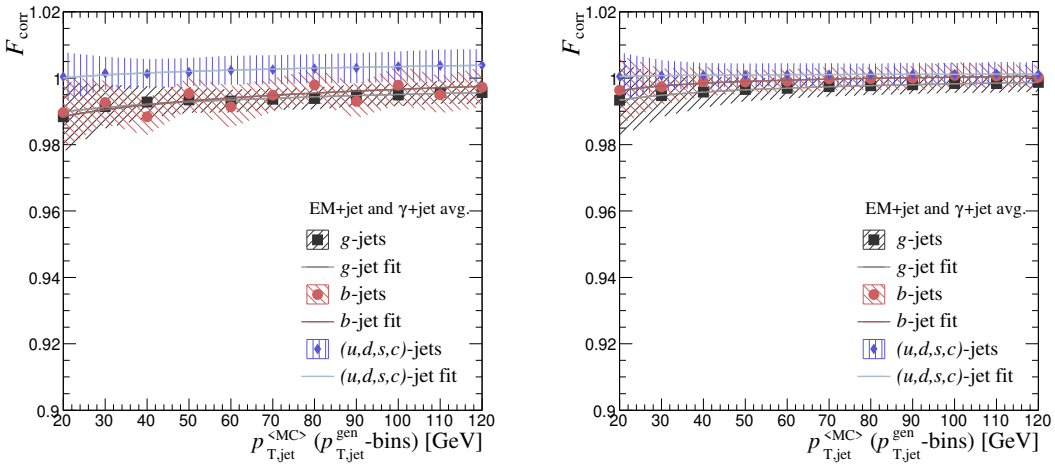

(a) Run IIa

(b) Run IIb1

(c) Run IIb2

(d) Run IIb3-4

Figure 5.11: F_{corr} resulting from fitting our HERWIG 7 MC to the DØ detector data points given in [41] for run IIa and in [40] for run IIb.

Chapter 6

Discussion

The agreement between the histogram lines and open circles in the p_{T}-balance profiles presented in subsection 5.3.1 indicates our level of success in reconstructing the features of the Pythia 6 MC samples used for JES determination at DØ. This is demonstrated further by the similarity of the diamonds and filled circles in the same subsection. At the level of the flavour-dependent correction factors F and F_{corr}, we have made our choices of interpretation in the manner that best reproduces the DØ F_{corr} histograms reported in the DØ analysis notes [41, 40]. This was successful for all run II epochs. These serve as the metrics by which we may claim to have reproduced the DØ method.

There are also some differences between our analysis and that of DØ. First, our γ+jet MC p_{T}-balance profile is somewhat below the DØ MC points in the high-E' region for all epochs. Notice however that there are no detector data points to fit to in at such E' values, and the agreement is good in the fit region. Second, the slight differences in the run IIb F plots are not present at the F_{corr} level obtained after normalizing F by the γ+jet sample average. Hence the difference is not too big and we are nonetheless in the same neighbourhood also at the level of F. One should also note that, in the context of top mass measurements, the most important region for F^b_{corr} is at around half of m_t. Therefore any fluctuations in the low-p_{T} region are not expected to cause drastic differences. Third, our Herwig 7 p_{T}-balance profiles are noticeably below the DØ Pythia 6 MC points. This is however an expected feature, since we do not have a DØ Herwig study to compare our results to. The points compared here are from different generators relying on different algorithms. Therefore the sample compositions may differ despite our efforts to initialize the simulations to be as similar as possible. The flavour fraction histograms presented in section 5.2 indicate that there are noticeably more gluon jets in the Herwig 7 samples with respect to the Pythia 6 samples. Gluon jets have higher particle multiplicities than quark jets [63], and an increase in the amount of particles between which to divide the jet energy is bound to result in less energetic particles. Consequently, the SPR-based reconstruction returns probe jets of lower p_{T}. For the tag object reconstructed using the photon SPR, there is no similar effect in $p_{\mathrm{T,tag}}$

to counter for a decrease in $p_{\mathrm{T,probe}}$.

6.1 Differences between our $F_{\mathbf{corr}}$ determination and DØ

The method used at DØ for finding the parameters A, B, C is to scan through a grid of χ^2 values in the fit parameter space, fit a 3rd degree polynomial in the p_{T}-balance profile and compute the χ^2 between this polynomial and the detector data points. The parameter-space coordinates of the grid point giving the smallest χ^2 are then taken as the resulting A, B, C values [41, 40]. However, this method depends on the roughness of the grid and the covered parameter space volume. Our method determines the χ^2 directly from the difference of the p_{T}-balance profile and the detector data points.

It appears from the figures presented in the analysis notes [41, 40] that DØ fit a 2nd degree polynomial to the F_{corr} histograms. The 2nd degree polynomial may however be ill-behaved in the region where there are no points to fit to, and the curve may e.g. turn unexpectedly. It remains unknown if DØ had any safeguard to assert that the F_{corr} remain at some plateau in the high-p_{T} region. Therefore our choice was to fit a power law to the F_{corr}, leading to more stable extrapolation properties. Furthermore, it remains unknown why the DØ F_{corr} fits in [40] are not very similar to the corresponding F_{corr} histograms, as can be seen also from the plots in subsection 5.4.1 by comparing the open markers with the continuous curves of the respective colours.

6.2 Propagating the corrections to top mass analyses

The jet energy corrections produced by the author and reported in this thesis serve as input to top mass analyses conducted by H. Siikonen. The details of these mass analyses are to be presented in an upcoming publication, but in this section we give a brief outline of the procedure for reference and documentative purposes.

Three top production samples are produced with the Pythia 6 top mass parameter range $m_t^{\mathrm{gen}} \in \{172.5, 173.7, 175\}$ GeV. These values are chosen based on the region where the experimental results vary. Next, a reconstruction chain is set up in a way that utilizes the F_{corr} extracted from [41, 40] and results in the top mass values observed by DØ. However, it should be noted that besides the top mass, there are differences between the observed and generator level values in the analysis for various other quantities besides m_t as well.

The parton level values are related to the observed values by a transfer function, which can be approximately decomposed into factors. Then F_{corr} is one such factor. Experimentwise, this corresponds to how the measured and calibrated energies are related to each other via the JES. However, what is used here is rather a residual JES related to F_{corr} as we do not perform a full detector simulation to obtain the JES. The residual

JES is found by comparing the location of W peaks at the jet level to the generator level values. In order to prevent bias, the effect of the light quark correction F_{corr}^{lq} to the JES is studied. In the top mass measurement channels considered here, the JES is further limited by demanding that the hadronically decaying W is on-shell.

The effect of our corrections to F_{corr} is studied by proceeding the reconstruction chain backwards, accounting for the ratio of our F_{corr} to the DØ F_{corr} in the process. Should this ratio be one, the backward reconstruction would yield the corresponding sample's m_t^{gen}. Since the ratio is not unity, there is a difference between the original simulation truth and the reconstructed m_t^{gen} value. This difference is interpreted as the mass shift due to effects from F_{corr}. Furthermore, the difference between the F_{corr} obtained from the Pythia 6 and Herwig 7 simulations implies additional uncertainty due to the modeling of showering and hadronization, but is yet to be taken into account. The resulting top mass values are eventually calculated as the average of the hadronically and leptonically decaying tops, although other estimator options have been studied as well. The shift obtained in the e+jets and μ+jets channels is shown in Fig. 6.1. In total, we observe a shift of $\Delta m_t \approx 2.5$ GeV.

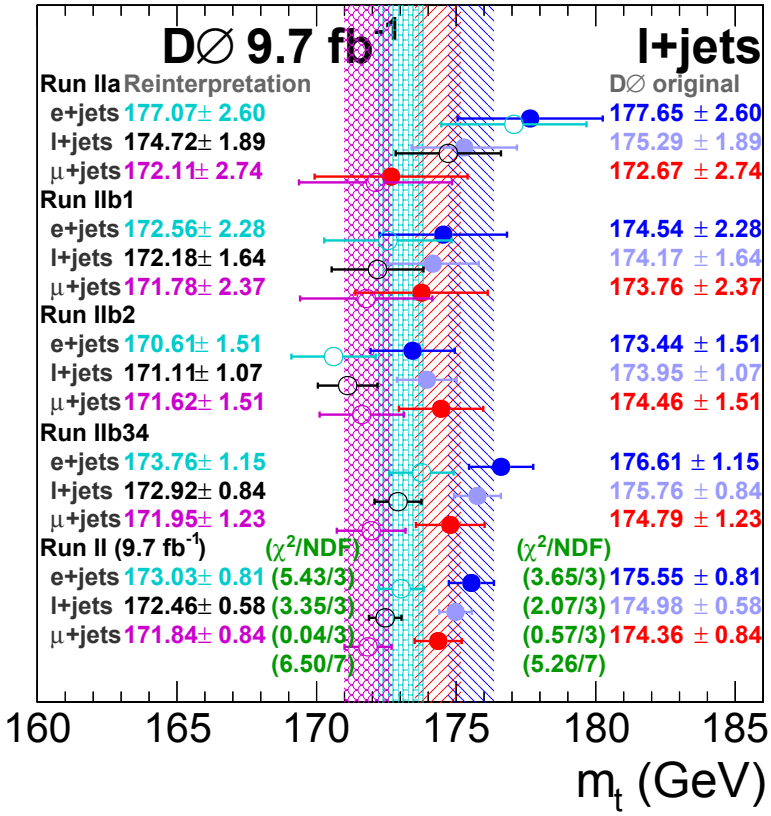

Figure 6.1: Reinterpreting the DØ l+jets channel results using our F_{corr}. The filled markers are the original DØ results. Open markers indicate where the top mass values shift after accounting for the ratio of the F_{corr} determined by us and DØ. Analysis performed and plot produced by H. Siikonen.

Chapter 7

Conclusions

For the first time in history hitherto, we have been able to reproduce the flavour-dependent jet energy correction methods originally designed and invoked by the DØ collaboration. The success of the reproduced simulations was demonstrated by comparing our chain of analysis to corresponding DØ results, using parameters determined by DØ as input to our own analysis code. We also presented new results based on revised techniques, leading to correction factors similar to the DØ run IIa epoch for both run IIa and all run IIb epochs. The impact of these correction factors on the l+jets channel top mass analyses was also briefly addressed. We reinterpreted the DØ top mass measurements and found that the resulting mass shift is a potential explanation to the inconsistency of the DØ m_t results with those of the ATLAS, CDF and CMS collaborations.

The presented shift in top mass is nevertheless insufficient to completely stabilize the EW vacuum in the context of the SM, should the world average top mass be recalculated. However, the metastability problem depends also on the precise determination of the strong coupling as well as the question of whether or not new physics beyond the SM can be found below the Planck scale.

A natural next step in the research of the calibration methods studied herein would be to implement the Missing-E_{T} Projection Fraction (MPF) method. This would be an alternative to the p_{T}-balance method for studying jet response. Hence, it would provide a way to examine the robustness of the determination of the SPR functions' data-level fit parameters A, B, C. An idealized version of the MPF method is discussed in [56]. It would be desirable to implement the method in a way that does not depend on strict cuts for instance on jet multiplicity. Furthermore, we currently have access to very little DØ MPF data that could be used for fits and determining R^{data} for the MPF method. This would require a full set of MC and detector data points for all run II epochs, similar to what we obtained for the p_{T}-balance method from the DØ analysis notes [41, 40].

Additionally, it would be interesting for the modern LHC experiments to implement the DØ-style calibration methods reconstructed here. Applying several alternative methods

at the same experiment and checking for their consistency is one possible step to be taken on the road to increasing precision at the LHC measurements. Despite our motivation was in the studies of top mass, b-jet identification and calibration is also important in a plethora of other topics. These topics can be found in the context of physics dealing with the EW sector and quarks, practically wherever b-jets are present. The inclusion of additional methods may shed some new light there as well. Following this work, the implementation of the reproduced method has been considered in particular at the CMS experiment. Some key differences to be accounted for are the need for redetermining the SPR parameters and making use of the Particle Flow [72] utilized by CMS.

A publication discussing this project as well as its implications to top mass measurements is currently in preparation. However, it was chosen to limit the scope of this thesis work by focusing on the investigation, reproduction and improvement of the DØ JES method for obtaining flavour-dependent jet energy corrections.

Appendices

Appendix A

DØ response parameters

The responses (4.3), (4.4), (4.5) and (4.6) were calculated using the distinct parameter values used at DØ during both run IIa and run IIb. The parameters for run IIa were extracted from [41] and are presented in tables A.1-A.10. The parameter values for run IIb were obtained from [40] and they are equal for all epochs IIb1, IIb2 and IIb3-4. Therefore we simply refer to these parameters by IIb without further division into different epochs' parameters. We use both the default run IIb SPR and the P20ToP17 corrected parameters, both of which are given in [40]. The run IIb parameters with the P20ToP17 correction are shown in tables A.11-A.20. Powers of ten, e.g. 10^{X}, shall be denoted by eX for ease reading the parameters automatically into an analysis code.

Table A.1: RunIIa parameters for $e^{\pm}$.

$\|\eta\|$ region	$p^{(0)}$	$p^{(1)}$	$p^{(2)}$	$p^{(3)}$	$p^{(4)}$
(0.0, 0.1)	0.935588	0.299488	3.92972	2.85453	2.26345e-05
(0.1, 0.2)	0.935594	0.523257	4.17529	2.71143	1.29605e-05
(0.2, 0.3)	0.928809	0.323032	4.04816	2.60768	0.000105303
(0.3, 0.4)	0.941915	-0.496271	1.07223	10.6921	13.8898
(0.4, 0.5)	0.930113	-0.39318	3.73424	2.57455	1.00012e-05
(0.5, 0.6)	0.935861	4.79903	9.66852	-0.704241	0.437941
(0.6, 0.7)	0.937074	5.68315	11.5458	-0.760942	0.426324
(0.7, 0.8)	0.932906	-0.844413	0.336375	5.67141	12.9282
(0.8, 0.9)	0.935304	-0.884043	0.307479	4.96387	14.4119
(0.9, 1.0)	0.929257	-0.94292	0.328488	4.56276	16.0012
(1.0, 1.1)	0.92018	2.64729	17.6103	-0.978835	0.288707
(1.1, 1.2)	0.919876	5.17597	38.4893	-1.62554	1.29717
(1.2, 1.3)	0.882751	8.89766	46.2002	-0.957796	0.30371
(1.3, 1.4)	0.696293	-1.01785	0.677931	16.1391	27.3143
(1.4, 1.5)	0.861668	21.8462	47.9298	-1.80712	0.923838
(1.5, 1.6)	0.969569	-1.2557	0.657646	19.7537	22.1466
(1.6, 1.7)	0.973023	22.9203	32.2526	-1.4139	0.782359
(1.7, 1.8)	0.975369	-1.58128	0.929667	22.7668	34.5357
(1.8, 1.9)	0.974222	-1.56043	1.09944	21.4196	33.8669
(1.9, 2.0)	0.968064	20.176	35.1173	-1.61511	0.931312
(2.0, 2.1)	0.968559	20.2955	36.1521	-1.6928	1.11028
(2.1, 2.2)	0.961358	18.0882	35.3453	-1.66177	1.0807
(2.2, 2.3)	0.964215	21.028	38.2394	-1.75656	1.13489
(2.3, 2.4)	0.96536	23.868	40.1452	-1.75938	1.18185
(2.4, 2.5)	0.960949	24.5302	39.451	-1.64526	1.13018
(2.5, 2.6)	0.95654	31.7664	38.4315	-1.36663	0.773106
(2.6, 2.7)	0.962981	-1.2424	0.758808	129.643	100
(2.7, 2.8)	0.960675	-0.970845	0.302102	135.711	100
(2.8, 2.9)	0.959324	82.2793	70.2658	-0.981568	0.331058
(2.9, 3.0)	0.956487	34.1563	42.9014	-0.976996	0.297029
(3.0, 3.1)	0.952198	34.8409	39.0397	-1.01014	0.327562
(3.1, 3.2)	0.951817	-1.34833	0.708778	46.2445	44.6503

Table A.2: RunIIa parameters for $K^{\pm}$.

$\|\eta\|$ region	$p^{(0)}$	$p^{(1)}$	$p^{(2)}$
(0.0, 0.1)	0.878605	0.56398	0.62083
(0.1, 0.2)	0.848368	0.560442	0.575974
(0.2, 0.3)	0.873756	0.547791	0.630722
(0.3, 0.4)	0.851994	0.593079	0.556731
(0.4, 0.5)	0.834876	0.60756	0.528241
(0.5, 0.6)	0.814292	0.606957	0.48704
(0.6, 0.7)	0.80218	0.678451	0.430221
(0.7, 0.8)	0.773835	0.753125	0.342543
(0.8, 0.9)	0.803279	0.835347	0.326763
(0.9, 1.0)	0.82612	0.859809	0.413536
(1.0, 1.1)	0.864318	0.89476	0.529982
(1.1, 1.2)	0.943403	0.909157	0.542415
(1.2, 1.3)	0.963529	0.943135	0.489727
(1.3, 1.4)	0.949825	0.908861	0.506901
(1.4, 1.5)	0.803979	0.976789	0.436683
(1.5, 1.6)	0.775056	0.914825	0.474932
(1.6, 1.7)	0.75358	0.972764	0.422509
(1.7, 1.8)	0.74023	0.910044	0.477433
(1.8, 1.9)	0.730468	0.91814	0.444735
(1.9, 2.0)	0.754279	0.926871	0.487408
(2.0, 2.1)	0.732376	0.925419	0.481114
(2.1, 2.2)	0.749241	0.900848	0.553564
(2.2, 2.3)	0.760623	0.91688	0.560446
(2.3, 2.4)	0.741519	0.905937	0.574688
(2.4, 2.5)	0.785588	0.877266	0.646326
(2.5, 2.6)	0.750672	0.891488	0.636655
(2.6, 2.7)	0.75065	0.895206	0.641735
(2.7, 2.8)	0.774122	0.866196	0.691965
(2.8, 2.9)	0.768441	0.886051	0.692597
(2.9, 3.0)	0.827219	0.867423	0.760868
(3.0, 3.1)	0.829429	0.8634	0.774519
(3.1, 3.2)	0.766491	0.908055	0.72269

Table A.3: RunIIa parameters for K^0_L.

$\|\eta\|$ region	$p^{(0)}$	$p^{(1)}$	$p^{(2)}$
(0.0, 0.1)	0.862242	0.656306	0.528689
(0.1, 0.2)	0.835476	0.668958	0.485465
(0.2, 0.3)	0.876279	0.645132	0.591264
(0.3, 0.4)	0.858359	0.659566	0.541698
(0.4, 0.5)	0.866893	0.684522	0.561105
(0.5, 0.6)	0.833966	0.690375	0.505792
(0.6, 0.7)	0.812063	0.716396	0.459975
(0.7, 0.8)	0.817093	0.718477	0.492779
(0.8, 0.9)	0.859993	0.728225	0.52433
(0.9, 1.0)	0.892218	0.765952	0.582846
(1.0, 1.1)	0.900858	0.761251	0.619088
(1.1, 1.2)	1	0.801657	0.654521
(1.2, 1.3)	1	0.859987	0.598765
(1.3, 1.4)	0.987008	0.809512	0.628576
(1.4, 1.5)	0.858787	0.765615	0.629836
(1.5, 1.6)	0.833717	0.720641	0.652349
(1.6, 1.7)	0.816918	0.768191	0.645693
(1.7, 1.8)	0.791421	0.738678	0.639992
(1.8, 1.9)	0.813741	0.732612	0.671606
(1.9, 2.0)	0.846186	0.775951	0.688308
(2.0, 2.1)	0.855849	0.762518	0.732186
(2.1, 2.2)	0.83721	0.784119	0.714172
(2.2, 2.3)	0.851666	0.787604	0.722316
(2.3, 2.4)	0.880135	0.76073	0.776075
(2.4, 2.5)	0.911449	0.794675	0.783164
(2.5, 2.6)	0.885653	0.803007	0.788771
(2.6, 2.7)	0.893456	0.802944	0.790948
(2.7, 2.8)	1	0.784179	0.850331
(2.8, 2.9)	1	0.802552	0.850917
(2.9, 3.0)	1	0.8511	0.843753
(3.0, 3.1)	1	0.855975	0.847773
(3.1, 3.2)	1	0.863116	0.851692

Table A.4: RunIIa parameters for K^0_S.

$\|\eta\|$ region	$p^{(0)}$	$p^{(1)}$	$p^{(2)}$
(0.0, 0.1)	0.836432	0.858121	0.332568
(0.1, 0.2)	0.812314	0.876456	0.2834
(0.2, 0.3)	0.834568	0.877753	0.348576
(0.3, 0.4)	0.830368	0.903593	0.334632
(0.4, 0.5)	0.83148	0.893048	0.354658
(0.5, 0.6)	0.81964	0.911315	0.353765
(0.6, 0.7)	0.812938	0.926256	0.354047
(0.7, 0.8)	0.803059	0.950405	0.367011
(0.8, 0.9)	0.85805	0.972468	0.45448
(0.9, 1.0)	0.888457	0.974774	0.5189
(1.0, 1.1)	0.90037	0.988563	0.570439
(1.1, 1.2)	1	0.987822	0.634154
(1.2, 1.3)	1	1.01552	0.589229
(1.3, 1.4)	1	0.985222	0.628626
(1.4, 1.5)	0.854049	1.01579	0.563481
(1.5, 1.6)	0.80554	1.00768	0.474494
(1.6, 1.7)	0.787491	1.00921	0.493068
(1.7, 1.8)	0.774081	1.02141	0.516892
(1.8, 1.9)	0.787426	1.02104	0.52901
(1.9, 2.0)	0.805527	1.02155	0.567152
(2.0, 2.1)	0.80657	1.0295	0.606783
(2.1, 2.2)	0.819219	1.03225	0.627704
(2.2, 2.3)	0.83602	1.02709	0.649606
(2.3, 2.4)	0.825226	1.02221	0.666746
(2.4, 2.5)	0.855612	1.02152	0.690408
(2.5, 2.6)	0.834501	1.04834	0.697311
(2.6, 2.7)	0.876586	1.02748	0.730831
(2.7, 2.8)	0.878961	1.01887	0.740743
(2.8, 2.9)	0.959859	1.0412	0.788124
(2.9, 3.0)	1	1.03455	0.810736
(3.0, 3.1)	1	1.04715	0.819096
(3.1, 3.2)	1	1.04229	0.827214

Table A.5: RunIIa parameters for Λ.

$\|\eta\|$ region	$p^{(0)}$	$p^{(1)}$	$p^{(2)}$
(0.0, 0.1)	0.79924	2.34464	-1.62568
(0.1, 0.2)	0.787822	2.73343	-1.88518
(0.2, 0.3)	0.791676	2.89465	-1.86125
(0.3, 0.4)	0.791623	2.64124	-1.6772
(0.4, 0.5)	0.785796	2.02675	-1.249
(0.5, 0.6)	0.770667	2.4019	-1.40369
(0.6, 0.7)	0.761966	2.45091	-1.48158
(0.7, 0.8)	0.753289	2.19307	-1.21278
(0.8, 0.9)	0.790039	1.70152	-0.668189
(0.9, 1.0)	0.795449	1.49121	-0.356575
(1.0, 1.1)	0.791992	1.47262	-0.228444
(1.1, 1.2)	0.873834	1.27314	0.156604
(1.2, 1.3)	0.910788	1.33461	0.169067
(1.3, 1.4)	0.905849	1.24061	0.226445
(1.4, 1.5)	0.761155	1.63064	-0.178961
(1.5, 1.6)	0.733871	1.6817	-0.250205
(1.6, 1.7)	0.716157	1.51151	-0.113269
(1.7, 1.8)	0.693255	1.47655	-0.0737748
(1.8, 1.9)	0.685794	1.6507	-0.18217
(1.9, 2.0)	0.695616	1.47537	0.000901184
(2.0, 2.1)	0.683344	1.46485	0.0405993
(2.1, 2.2)	0.68812	1.34041	0.205463
(2.2, 2.3)	0.707206	1.32793	0.274739
(2.3, 2.4)	0.684644	1.2408	0.320727
(2.4, 2.5)	0.703394	1.26224	0.358539
(2.5, 2.6)	0.670546	1.30783	0.355592
(2.6, 2.7)	0.677796	1.25103	0.407835
(2.7, 2.8)	0.689299	1.24209	0.463669
(2.8, 2.9)	0.68385	1.22146	0.502855
(2.9, 3.0)	0.710535	1.24201	0.573796
(3.0, 3.1)	0.695671	1.23061	0.577475
(3.1, 3.2)	0.691886	1.22906	0.580714

Table A.6: RunIIa parameters for $\mu^{\pm}$.

$\|\eta\|$ region	$p^{(0)}$	$p^{(1)}$	$p^{(2)}$	$p^{(3)}$
(0.0, 0.1)	-46088	112488	-0.246325	0.00479363
(0.1, 0.2)	-4.32653e+06	1.06523e+07	-0.227522	0.000480521
(0.2, 0.3)	-1.41049e+07	3.41657e+07	-0.2335	0.000269325
(0.3, 0.4)	-5.53921e+07	1.24982e+08	-0.208941	0.000140011
(0.4, 0.5)	-5.00622e+08	1.06243e+09	-0.184559	4.7686e-05
(0.5, 0.6)	-1.66531e+09	3.16109e+09	-0.0291663	2.50071e-05
(0.6, 0.7)	-3.98643e+09	6.96331e+09	0.091851	1.57807e-05
(0.7, 0.8)	-7.90225e+09	1.32421e+10	0.0869162	1.14906e-05
(0.8, 0.9)	-2.46619e+10	4.07388e+10	0.101604	6.56942e-06
(0.9, 1.0)	-3.54582e+10	5.83861e+10	-0.163937	5.80051e-06
(1.0, 1.1)	-3.54679e+10	5.84087e+10	-0.290361	5.90403e-06
(1.1, 1.2)	-2.92133e+10	4.81581e+10	-0.270259	7.93786e-06
(1.2, 1.3)	-5.93461e+10	9.79281e+10	-0.240782	5.70734e-06
(1.3, 1.4)	-6.15951e+10	9.42571e+10	-0.162647	6.01752e-06
(1.4, 1.5)	-5.67347e+10	8.85446e+10	-0.310621	5.68538e-06
(1.5, 1.6)	-5.91967e+10	9.06419e+10	-0.369599	5.81302e-06
(1.6, 1.7)	-6.71757e+10	8.84234e+10	-0.214369	5.7562e-06
(1.7, 1.8)	-9.36226e+10	1.27399e+11	-0.124105	4.43337e-06
(1.8, 1.9)	-1.40946e+11	1.91021e+11	-0.0587697	3.48696e-06
(1.9, 2.0)	-2.11752e+11	2.81868e+11	-0.0216599	2.87057e-06
(2.0, 2.1)	-2.15894e+11	2.65874e+11	0.155016	2.73231e-06
(2.1, 2.2)	-3.16969e+11	4.43806e+11	-0.187404	2.37977e-06
(2.2, 2.3)	-4.25798e+11	6.33395e+11	-0.382301	2.19153e-06
(2.3, 2.4)	-4.46568e+11	6.10653e+11	-0.231548	2.13824e-06
(2.4, 2.5)	-2.61701e+11	4.37868e+11	-0.570536	2.7226e-06
(2.5, 2.6)	-3.97645e+11	5.42069e+11	-0.306036	2.2692e-06
(2.6, 2.7)	-3.98293e+11	5.54174e+11	-0.401803	2.31219e-06
(2.7, 2.8)	-4.15898e+11	5.497e+11	-0.334709	2.3041e-06
(2.8, 2.9)	-4.0694e+11	5.55049e+11	-0.445784	2.31774e-06
(2.9, 3.0)	-4.26265e+11	5.54927e+11	-0.441344	2.32432e-06
(3.0, 3.1)	-4.16368e+11	5.58457e+11	-0.543729	2.33153e-06
(3.1, 3.2)	-4.35335e+11	5.47426e+11	-0.406186	2.30364e-06

Table A.7: RunIIa parameters for n.

$\|\eta\|$ region	$p^{(0)}$	$p^{(1)}$	$p^{(2)}$
(0.0, 0.1)	0.823733	1.34777	-2.34471
(0.1, 0.2)	0.810994	1.9469	-2.59605
(0.2, 0.3)	0.814421	1.96729	-2.60666
(0.3, 0.4)	0.814585	1.60131	-2.0648
(0.4, 0.5)	0.805828	1.43164	-1.63289
(0.5, 0.6)	0.798472	1.99667	-2.30278
(0.6, 0.7)	0.786109	1.97216	-2.23036
(0.7, 0.8)	0.782195	1.62681	-1.8728
(0.8, 0.9)	0.808764	1.41331	-1.4062
(0.9, 1.0)	0.810269	0.982261	-0.612012
(1.0, 1.1)	0.807408	1.02018	-0.399238
(1.1, 1.2)	0.884288	0.866284	0.254706
(1.2, 1.3)	0.924035	0.881854	0.283914
(1.3, 1.4)	0.911809	0.86341	0.302656
(1.4, 1.5)	0.770269	0.809294	-0.0501709
(1.5, 1.6)	0.752055	0.692966	0.254566
(1.6, 1.7)	0.74108	0.675101	0.376143
(1.7, 1.8)	0.713646	0.698564	0.279139
(1.8, 1.9)	0.726283	0.633088	0.432847
(1.9, 2.0)	0.743482	0.617156	0.509901
(2.0, 2.1)	0.708702	0.811351	0.348887
(2.1, 2.2)	0.730678	0.748061	0.532554
(2.2, 2.3)	0.756626	0.665151	0.615279
(2.3, 2.4)	0.774999	0.586717	0.725742
(2.4, 2.5)	0.827873	0.652261	0.762124
(2.5, 2.6)	0.757672	0.694091	0.699615
(2.6, 2.7)	0.764741	0.681657	0.721356
(2.7, 2.8)	0.95631	0.674357	0.869047
(2.8, 2.9)	0.858459	0.719744	0.818713
(2.9, 3.0)	0.918614	0.79609	0.836333
(3.0, 3.1)	0.94696	0.803586	0.851111
(3.1, 3.2)	0.87036	0.818951	0.826293

Table A.8: RunIIa parameters for γ.

$\lvert\eta\rvert$ region	$p^{(0)}$	$p^{(1)}$	$p^{(2)}$	$p^{(3)}$	$p^{(4)}$	$p^{(5)}$
(0.0, 0.1)	2659	69.3695	18.2673	5.55104	1.60666	-2658.05
(0.1, 0.2)	4969.99	77.2245	19.5899	5.89242	1.62996	-4969.04
(0.2, 0.3)	6939.34	95.1989	23.7115	6.47245	1.74351	-6938.39
(0.3, 0.4)	1950.12	44.3761	12.3565	3.50814	1.03612	-1949.18
(0.4, 0.5)	10333.4	61.5275	15.258	6.1528	1.6034	-10332.4
(0.5, 0.6)	6927.43	203.57	49.6836	8.91212	2.4113	-6926.48
(0.6, 0.7)	1592.98	63.7851	17.9017	5.5391	1.65388	-1592.04
(0.7, 0.8)	4794.94	143.181	36.6187	8.42552	2.32751	-4794
(0.8, 0.9)	3644.49	104.219	27.6207	8.1575	2.27617	-3643.55
(0.9, 1.0)	5178.59	10.7986	2.95173	181.742	46.7111	-5177.65
(1.0, 1.1)	4042.73	14.4874	4.03015	259.813	67.7165	-4041.79
(1.1, 1.2)	3604.84	315.094	85.7567	10.3216	2.84546	-3603.89
(1.2, 1.3)	37.6002	234.059	100	3.96091	1.86673	-36.6722
(1.3, 1.4)	2460.64	361.215	94.2267	6.80365	1.948	-2459.92
(1.4, 1.5)	57.9966	8.5911	3.74904	265.686	100	-57.1113
(1.5, 1.6)	11648	222.579	52.5827	13.1345	3.42327	-11647.1
(1.6, 1.7)	21412.9	375.375	86.9451	16.832	4.22013	-21411.9
(1.7, 1.8)	17701.5	341.764	80.83	17.5891	4.45543	-17700.5
(1.8, 1.9)	495.355	343.642	100	15.6636	5.23266	-494.378
(1.9, 2.0)	4629.89	393.58	100	20.1904	5.55952	-4628.92
(2.0, 2.1)	1930.28	371.382	100	16.535	4.87616	-1929.31
(2.1, 2.2)	4587.63	351.051	90.2009	20.052	5.50727	-4586.67
(2.2, 2.3)	1442.63	361.699	100	17.4052	5.2418	-1441.66
(2.3, 2.4)	12904.9	412.917	99.9999	18.5311	4.78193	-12903.9
(2.4, 2.5)	218.665	314.055	100	15.5644	5.61015	-217.703
(2.5, 2.6)	1229.53	365.168	100	11.1133	3.40395	-1228.57
(2.6, 2.7)	7.94517	217.6	100	2.15107	1.55323	-6.98257
(2.7, 2.8)	4.69568	200.07	100	1.46742	1.35025	-3.7352
(2.8, 2.9)	16.0897	241.687	100	3.18013	1.8244	-15.1299
(2.9, 3.0)	54.9205	275.311	100	6.33247	2.77021	-53.9608
(3.0, 3.1)	118.309	301.5	100	8.11703	3.16106	-117.354
(3.1, 3.2)	578.052	348.417	100	9.2159	3.02302	-577.101

Table A.9: RunIIa parameters for $\pi^{\pm}$.

$\lvert\eta\rvert$ region	$p^{(0)}$	$p^{(1)}$	$p^{(2)}$
(0.0, 0.1)	0.860797	0.632369	0.539393
(0.1, 0.2)	0.850693	0.630273	0.541471
(0.2, 0.3)	0.845489	0.650259	0.518831
(0.3, 0.4)	0.856089	0.649128	0.559122
(0.4, 0.5)	0.839919	0.686964	0.512569
(0.5, 0.6)	0.821092	0.693096	0.473706
(0.6, 0.7)	0.802175	0.719734	0.427311
(0.7, 0.8)	0.780728	0.781769	0.37995
(0.8, 0.9)	0.818153	0.805275	0.418298
(0.9, 1.0)	0.843768	0.840645	0.486545
(1.0, 1.1)	0.864473	0.873748	0.556819
(1.1, 1.2)	0.979511	0.877904	0.62851
(1.2, 1.3)	0.990021	0.88364	0.592402
(1.3, 1.4)	1	0.878883	0.630325
(1.4, 1.5)	0.830045	0.89526	0.550935
(1.5, 1.6)	0.774484	0.882901	0.498146
(1.6, 1.7)	0.758813	0.884565	0.501162
(1.7, 1.8)	0.727154	0.877421	0.451664
(1.8, 1.9)	0.72633	0.870825	0.459533
(1.9, 2.0)	0.750314	0.865985	0.503125
(2.0, 2.1)	0.73146	0.865857	0.501728
(2.1, 2.2)	0.742131	0.872904	0.5473
(2.2, 2.3)	0.764877	0.869004	0.60271
(2.3, 2.4)	0.735219	0.864225	0.577661
(2.4, 2.5)	0.756235	0.880723	0.608848
(2.5, 2.6)	0.730606	0.868549	0.616116
(2.6, 2.7)	0.736399	0.872302	0.627813
(2.7, 2.8)	0.727449	0.872778	0.636553
(2.8, 2.9)	0.720124	0.875514	0.639329
(2.9, 3.0)	0.740443	0.875647	0.687514
(3.0, 3.1)	0.719407	0.87	0.681063
(3.1, 3.2)	0.73195	0.890053	0.707342

Table A.10: RunIIa parameters for p.

$\lvert\eta\rvert$ region	$p^{(0)}$	$p^{(1)}$	$p^{(2)}$
(0.0, 0.1)	0.822506	3.52553	-2.94879
(0.1, 0.2)	0.812893	4.37602	-3.55282
(0.2, 0.3)	0.818323	4.64685	-3.70741
(0.3, 0.4)	0.812804	3.50995	-2.90102
(0.4, 0.5)	0.806158	3.71462	-3.03158
(0.5, 0.6)	0.79913	3.45286	-2.80311
(0.6, 0.7)	0.792804	3.02194	-2.40044
(0.7, 0.8)	0.774489	3.12402	-2.47591
(0.8, 0.9)	0.800952	2.24678	-1.55752
(0.9, 1.0)	0.794129	2.21421	-1.42287
(1.0, 1.1)	0.794018	1.82393	-0.935459
(1.1, 1.2)	0.876406	1.19412	0.0411741
(1.2, 1.3)	0.90948	1.27162	0.0125828
(1.3, 1.4)	0.89152	1.30335	0.0159607
(1.4, 1.5)	0.771733	1.54969	-0.35037
(1.5, 1.6)	0.731166	2.22291	-1.20377
(1.6, 1.7)	0.71722	1.71393	-0.597006
(1.7, 1.8)	0.699545	2.00432	-1.00536
(1.8, 1.9)	0.699556	1.86898	-0.763125
(1.9, 2.0)	0.705317	1.50316	-0.349243
(2.0, 2.1)	0.693087	1.61502	-0.429272
(2.1, 2.2)	0.681487	1.42705	-0.193888
(2.2, 2.3)	0.707124	1.24625	0.174338
(2.3, 2.4)	0.681316	1.2012	0.154039
(2.4, 2.5)	0.7024	1.18246	0.316479
(2.5, 2.6)	0.675002	1.11854	0.345657
(2.6, 2.7)	0.692144	0.975135	0.470717
(2.7, 2.8)	0.685923	1.02506	0.464098
(2.8, 2.9)	0.689911	1.03604	0.521858
(2.9, 3.0)	0.690302	1.07904	0.549674
(3.0, 3.1)	0.69924	0.935002	0.631557
(3.1, 3.2)	0.659514	1.11965	0.533861

Table A.11: RunIIb parameters for $e^{\pm}$.

$\|\eta\|$ region	$p^{(0)}$	$p^{(1)}$	$p^{(2)}$	$p^{(3)}$	$p^{(4)}$
(0.0, 0.1)	0.941208	2.50197	6.53843	-0.573548	0.100483
(0.1, 0.2)	0.94236	6.25898	10.1112	-0.73475	0.258273
(0.2, 0.3)	0.939753	2.02081	6.15205	-0.581558	0.116517
(0.3, 0.4)	0.939355	-0.750865	0.279076	5.12945	9.31557
(0.4, 0.5)	0.931738	-0.598296	0.118428	1.61778	6.3194
(0.5, 0.6)	0.936941	-0.799356	0.265318	5.05695	10.5199
(0.6, 0.7)	0.934814	-0.797671	0.273711	4.49899	10.4788
(0.7, 0.8)	0.932292	-0.845947	0.277627	4.53705	11.6054
(0.8, 0.9)	0.925836	-0.909903	0.314013	4.82553	13.8808
(0.9, 1.0)	0.93131	-0.926018	0.304888	4.76157	17.2427
(1.0, 1.1)	0.9244	-0.970689	0.314403	3.44183	19.5487
(1.1, 1.2)	0.91224	-1.74431	1.28115	6.42197	38.8477
(1.2, 1.3)	0.888362	-1.01607	0.385245	11.0101	50.5366
(1.3, 1.4)	0.692133	7.40003	15.1952	-0.931386	0.455629
(1.4, 1.5)	0.861602	-1.56442	0.614226	20.1242	44.2175
(1.5, 1.6)	0.970896	-1.33225	0.641935	16.563	20.2828
(1.6, 1.7)	0.972432	-1.44716	0.686404	21.1326	31.6004
(1.7, 1.8)	0.974323	-1.6526	0.885681	21.8145	35.0814
(1.8, 1.9)	0.973029	-1.67126	0.85434	20.9955	35.418
(1.9, 2.0)	0.967712	-1.62978	0.865498	16.9791	32.7884
(2.0, 2.1)	0.967451	16.3395	34.3826	-1.65183	0.866231
(2.1, 2.2)	0.957925	-1.76214	0.972695	16.6022	34.885
(2.2, 2.3)	0.964119	-1.71283	0.870999	16.7175	35.8345
(2.3, 2.4)	0.964546	18.3875	36.8262	-1.71251	0.922648
(2.4, 2.5)	0.959418	-1.73343	1.02167	20.8904	38.4167
(2.5, 2.6)	0.956955	30.8041	39.0965	-1.3985	0.696942
(2.6, 2.7)	0.962145	-1.31006	0.684873	127.012	100
(2.7, 2.8)	0.959515	-1.22518	0.615599	129.572	100
(2.8, 2.9)	0.95925	-1.39847	0.733814	123.388	100
(2.9, 3.0)	0.955061	-1.40952	0.693574	36.8121	46.5104
(3.0, 3.1)	0.951913	-1.40711	0.713879	36.6468	41.7348
(3.1, 3.2)	0.947723	33.423	37.2798	-1.34834	0.66137

Table A.12: RunIIb parameters for $K^{\pm}$.

$\lvert\eta\rvert$ region	$p^{(0)}$	$p^{(1)}$	$p^{(2)}$
(0.0, 0.1)	0.822076	0.799632	0.34622
(0.1, 0.2)	0.808049	0.786815	0.334145
(0.2, 0.3)	0.819156	0.798571	0.344681
(0.3, 0.4)	0.817765	0.799823	0.363268
(0.4, 0.5)	0.816417	0.797421	0.378325
(0.5, 0.6)	0.794646	0.814148	0.335414
(0.6, 0.7)	0.786573	0.808343	0.333295
(0.7, 0.8)	0.773154	0.81383	0.365289
(0.8, 0.9)	0.832335	0.840747	0.455703
(0.9, 1.0)	0.855265	0.852727	0.5189
(1.0, 1.1)	0.890293	0.873994	0.597485
(1.1, 1.2)	0.973795	0.882846	0.603278
(1.2, 1.3)	0.994319	0.870969	0.582768
(1.3, 1.4)	0.977562	0.874264	0.584566
(1.4, 1.5)	0.8805	0.893191	0.641269
(1.5, 1.6)	0.808223	0.879459	0.585071
(1.6, 1.7)	0.797291	0.874889	0.599926
(1.7, 1.8)	0.774906	0.881769	0.59243
(1.8, 1.9)	0.780374	0.881232	0.598404
(1.9, 2.0)	0.793127	0.880634	0.606451
(2.0, 2.1)	0.777857	0.886549	0.610169
(2.1, 2.2)	0.773284	0.881373	0.622128
(2.2, 2.3)	0.800675	0.887915	0.649905
(2.3, 2.4)	0.768843	0.904391	0.639293
(2.4, 2.5)	0.807279	0.90516	0.681039
(2.5, 2.6)	0.772658	0.896964	0.68035
(2.6, 2.7)	0.783928	0.900133	0.689819
(2.7, 2.8)	0.795362	0.910776	0.708762
(2.8, 2.9)	0.809461	0.91515	0.733943
(2.9, 3.0)	0.835758	0.922702	0.762291
(3.0, 3.1)	0.82255	0.922035	0.762625
(3.1, 3.2)	0.905189	0.940495	0.810406

Table A.13: RunIIb parameters for K^0_L.

$\lvert\eta\rvert$ region	$p^{(0)}$	$p^{(1)}$	$p^{(2)}$
(0.0, 0.1)	0.847435	0.734348	0.442908
(0.1, 0.2)	0.822632	0.750845	0.383657
(0.2, 0.3)	0.842629	0.752434	0.440905
(0.3, 0.4)	0.838845	0.759176	0.438263
(0.4, 0.5)	0.839197	0.775737	0.449451
(0.5, 0.6)	0.830098	0.765203	0.46619
(0.6, 0.7)	0.806772	0.758731	0.399872
(0.7, 0.8)	0.79673	0.771803	0.412971
(0.8, 0.9)	0.843158	0.789465	0.466238
(0.9, 1.0)	0.861288	0.802967	0.510634
(1.0, 1.1)	0.868608	0.831756	0.54875
(1.1, 1.2)	0.986282	0.837423	0.626934
(1.2, 1.3)	1	0.837634	0.606542
(1.3, 1.4)	0.968125	0.818877	0.611415
(1.4, 1.5)	0.833732	0.836848	0.551034
(1.5, 1.6)	0.793056	0.826622	0.541808
(1.6, 1.7)	0.785809	0.823865	0.565755
(1.7, 1.8)	0.766705	0.827388	0.548159
(1.8, 1.9)	0.77447	0.834569	0.559662
(1.9, 2.0)	0.789832	0.840919	0.587325
(2.0, 2.1)	0.778975	0.847289	0.598336
(2.1, 2.2)	0.775331	0.826051	0.621866
(2.2, 2.3)	0.814237	0.86262	0.656863
(2.3, 2.4)	0.79084	0.832672	0.672785
(2.4, 2.5)	0.8471	0.850205	0.717218
(2.5, 2.6)	0.807963	0.850922	0.713234
(2.6, 2.7)	0.850873	0.842701	0.753984
(2.7, 2.8)	0.861086	0.838132	0.768638
(2.8, 2.9)	0.912877	0.854657	0.803654
(2.9, 3.0)	0.897045	0.893337	0.796133
(3.0, 3.1)	0.852648	0.892716	0.778949
(3.1, 3.2)	0.848007	0.914506	0.778625

Table A.14: RunIIb parameters for K^0_S.

$\|\eta\|$ region	$p^{(0)}$	$p^{(1)}$	$p^{(2)}$
(0.0, 0.1)	0.849074	0.813983	0.428101
(0.1, 0.2)	0.840997	0.821527	0.429602
(0.2, 0.3)	0.848169	0.816542	0.433534
(0.3, 0.4)	0.846863	0.821912	0.438719
(0.4, 0.5)	0.846738	0.825822	0.46527
(0.5, 0.6)	0.832995	0.835638	0.443816
(0.6, 0.7)	0.83065	0.833631	0.469502
(0.7, 0.8)	0.821376	0.845741	0.483188
(0.8, 0.9)	0.878319	0.863574	0.55633
(0.9, 1.0)	0.919514	0.885853	0.614475
(1.0, 1.1)	0.957731	0.901072	0.668224
(1.1, 1.2)	1	0.898372	0.659404
(1.2, 1.3)	1	0.8888	0.638538
(1.3, 1.4)	1	0.906675	0.664877
(1.4, 1.5)	0.942078	0.910886	0.704033
(1.5, 1.6)	0.861265	0.896807	0.641138
(1.6, 1.7)	0.83916	0.894931	0.63526
(1.7, 1.8)	0.851553	0.909335	0.673894
(1.8, 1.9)	0.848346	0.914154	0.670545
(1.9, 2.0)	0.88475	0.925505	0.691777
(2.0, 2.1)	0.886906	0.948698	0.711163
(2.1, 2.2)	0.932801	0.932361	0.75732
(2.2, 2.3)	0.935081	0.970994	0.747878
(2.3, 2.4)	1	0.963662	0.794754
(2.4, 2.5)	1	0.955872	0.796785
(2.5, 2.6)	1	0.959121	0.808335
(2.6, 2.7)	1	0.966835	0.808963
(2.7, 2.8)	1	0.960957	0.813645
(2.8, 2.9)	1	0.958802	0.827472
(2.9, 3.0)	1	0.973901	0.832058
(3.0, 3.1)	1	0.958663	0.853577
(3.1, 3.2)	1	1.00235	0.832544

Table A.15: RunIIb parameters for Λ.

$\|\eta\|$ region	$p^{(0)}$	$p^{(1)}$	$p^{(2)}$
(0.0, 0.1)	0.797926	2.72782	-1.66259
(0.1, 0.2)	0.789137	2.77609	-1.73597
(0.2, 0.3)	0.7933	2.59726	-1.59521
(0.3, 0.4)	0.789276	2.70361	-1.60873
(0.4, 0.5)	0.781929	2.46835	-1.47604
(0.5, 0.6)	0.773542	2.487	-1.42649
(0.6, 0.7)	0.762494	2.5467	-1.43932
(0.7, 0.8)	0.746613	2.47935	-1.3441
(0.8, 0.9)	0.774376	2.08206	-0.992786
(0.9, 1.0)	0.78545	1.87475	-0.679358
(1.0, 1.1)	0.789941	1.56637	-0.272905
(1.1, 1.2)	0.871975	1.32697	0.118855
(1.2, 1.3)	0.896878	1.40192	0.0634329
(1.3, 1.4)	0.891974	1.3543	0.1371
(1.4, 1.5)	0.761789	1.65538	-0.216312
(1.5, 1.6)	0.728356	1.65657	-0.225436
(1.6, 1.7)	0.714133	1.64613	-0.225164
(1.7, 1.8)	0.686727	1.73468	-0.312475
(1.8, 1.9)	0.685593	1.73488	-0.279157
(1.9, 2.0)	0.690862	1.61988	-0.113617
(2.0, 2.1)	0.677435	1.60578	-0.0929344
(2.1, 2.2)	0.678874	1.47547	0.0831716
(2.2, 2.3)	0.699317	1.39671	0.232813
(2.3, 2.4)	0.677591	1.39937	0.23917
(2.4, 2.5)	0.701948	1.29965	0.368007
(2.5, 2.6)	0.670438	1.33469	0.337561
(2.6, 2.7)	0.680618	1.2944	0.400023
(2.7, 2.8)	0.676061	1.28334	0.430201
(2.8, 2.9)	0.687052	1.24476	0.504289
(2.9, 3.0)	0.710137	1.21083	0.582207
(3.0, 3.1)	0.707464	1.20276	0.599489
(3.1, 3.2)	0.723966	1.19201	0.642217

Table A.16: RunIIb parameters for $\mu^{\pm}$.

$\|\eta\|$ region	$p^{(0)}$	$p^{(1)}$	$p^{(2)}$	$p^{(3)}$
(0.0, 0.1)	-845869	2.04671e+06	-0.232835	0.0011105
(0.1, 0.2)	-2.11658e+07	4.99093e+07	-0.227739	0.00022326
(0.2, 0.3)	-1.76033e+07	4.01018e+07	-0.209657	0.000249175
(0.3, 0.4)	-1.85024e+07	4.29062e+07	-0.23602	0.000239652
(0.4, 0.5)	-4.87903e+07	1.03336e+08	-0.169521	0.000150455
(0.5, 0.6)	-3.19686e+08	6.3151e+08	-0.0860243	5.7613e-05
(0.6, 0.7)	-5.53859e+07	9.96671e+07	0.0400128	0.000135378
(0.7, 0.8)	-1.9249e+07	3.31861e+07	0.0442058	0.000231331
(0.8, 0.9)	-1.63326e+09	2.78576e+09	0.0643438	2.51734e-05
(0.9, 1.0)	-2.50201e+09	4.24116e+09	-0.143569	2.10951e-05
(1.0, 1.1)	-2.33262e+07	3.9343e+07	-0.286848	0.000225903
(1.1, 1.2)	-6.38793e+07	1.08056e+08	-0.308361	0.000165769
(1.2, 1.3)	-1.1071e+07	1.83895e+07	-0.202605	0.000412203
(1.3, 1.4)	-1.55281e+07	2.28967e+07	-0.177834	0.000386238
(1.4, 1.5)	-5.40757e+07	7.28137e+07	-0.169126	0.000196251
(1.5, 1.6)	-3.11515e+07	4.19059e+07	-0.262557	0.000267059
(1.6, 1.7)	-29539.2	36952.5	-0.205646	0.00887773
(1.7, 1.8)	-5.58374e+07	6.96855e+07	-0.0837477	0.000189689
(1.8, 1.9)	-5.25795e+07	6.71398e+07	-0.0412191	0.000186807
(1.9, 2.0)	-1.44678e+06	1.91619e+06	-0.0471874	0.00110654
(2.0, 2.1)	-4.50732e+07	5.43792e+07	0.150788	0.000192463
(2.1, 2.2)	-6.65555e+07	8.64078e+07	-0.118355	0.000168429
(2.2, 2.3)	-538.115	920.954	-0.644432	0.0572243
(2.3, 2.4)	-77.2484	131.794	-0.601185	0.14293
(2.4, 2.5)	-38.8381	67.7287	-0.720275	0.207146
(2.5, 2.6)	-46.3054	79.9272	-0.661683	0.182209
(2.6, 2.7)	-47.4294	82.0169	-0.730881	0.184437
(2.7, 2.8)	-30.7187	54.2883	-0.780982	0.226337
(2.8, 2.9)	-24.8646	43.5895	-0.788046	0.251714
(2.9, 3.0)	-20.9977	37.6603	-0.859852	0.271456
(3.0, 3.1)	-18.7364	33.2281	-0.914634	0.289458
(3.1, 3.2)	-15.973	28.6135	-0.883073	0.308064

Table A.17: RunIIb parameters for n.

$\|\eta\|$ region	$p^{(0)}$	$p^{(1)}$	$p^{(2)}$
(0.0, 0.1)	0.819053	1.38601	-1.93665
(0.1, 0.2)	0.810747	1.39458	-2.10612
(0.2, 0.3)	0.815348	1.27177	-1.83763
(0.3, 0.4)	0.811317	1.39204	-1.88061
(0.4, 0.5)	0.804553	1.23179	-1.60141
(0.5, 0.6)	0.795258	1.29914	-1.63037
(0.6, 0.7)	0.787626	1.41637	-1.95149
(0.7, 0.8)	0.771088	1.51912	-2.02873
(0.8, 0.9)	0.798688	1.23725	-1.30099
(0.9, 1.0)	0.802359	1.08887	-0.760233
(1.0, 1.1)	0.79639	0.912882	-0.359655
(1.1, 1.2)	0.884022	0.854086	0.23825
(1.2, 1.3)	0.910801	0.942055	0.168152
(1.3, 1.4)	0.888836	0.976787	0.113484
(1.4, 1.5)	0.769951	1.06522	-0.252263
(1.5, 1.6)	0.733077	1.03031	-0.388315
(1.6, 1.7)	0.722438	0.844154	0.0580221
(1.7, 1.8)	0.699138	1.04491	-0.36198
(1.8, 1.9)	0.705934	0.869743	0.0975191
(1.9, 2.0)	0.709636	0.950412	0.0707458
(2.0, 2.1)	0.704235	0.885838	0.226668
(2.1, 2.2)	0.708308	0.808864	0.382755
(2.2, 2.3)	0.737651	0.747187	0.536891
(2.3, 2.4)	0.721534	0.757522	0.555841
(2.4, 2.5)	0.755283	0.755586	0.62747
(2.5, 2.6)	0.732795	0.756355	0.64439
(2.6, 2.7)	0.750362	0.740121	0.682725
(2.7, 2.8)	0.803146	0.714062	0.766389
(2.8, 2.9)	0.855066	0.76942	0.803788
(2.9, 3.0)	0.806343	0.815401	0.771174
(3.0, 3.1)	0.833238	0.832136	0.794158
(3.1, 3.2)	0.817346	0.851286	0.789252

Table A.18: RunIIb parameters for γ.

$\lvert\eta\rvert$ region	$p^{(0)}$	$p^{(1)}$	$p^{(2)}$	$p^{(3)}$	$p^{(4)}$	$p^{(5)}$
(0.0, 0.1)	3282.62	115.073	29.2108	6.31546	1.81449	-3281.67
(0.1, 0.2)	6201.6	106.114	26.3368	6.12717	1.6771	-6200.65
(0.2, 0.3)	85.5496	2.77048	1.17129	48.4796	17.2251	-84.5962
(0.3, 0.4)	2357.06	73.675	19.653	5.27575	1.54903	-2356.12
(0.4, 0.5)	3933.14	72.9553	19.2005	5.01768	1.4001	-3932.19
(0.5, 0.6)	3684.76	106.854	27.6015	7.239	2.04577	-3683.82
(0.6, 0.7)	3285.06	80.8267	21.4583	7.16739	2.02284	-3284.12
(0.7, 0.8)	3816.65	113.463	29.6299	7.69614	2.15706	-3815.71
(0.8, 0.9)	1217.72	6.2281	1.89986	88.5661	25.5755	-1216.78
(0.9, 1.0)	5631.96	11.8692	3.23216	217.394	55.5197	-5631.01
(1.0, 1.1)	3328.05	12.7623	3.61205	267.308	70.7759	-3327.1
(1.1, 1.2)	3165.55	11.9436	3.34692	350.035	95.242	-3164.6
(1.2, 1.3)	78.2842	5.88953	2.43338	261.536	100	-77.352
(1.3, 1.4)	0.736624	0.405617	4.73105	-0.210415	0.186266	-0.0462887
(1.4, 1.5)	764.368	12.9998	4.11872	339.532	100	-763.486
(1.5, 1.6)	26631.5	12.2794	3.05281	221.215	50.5016	-26630.6
(1.6, 1.7)	16802.3	388.057	90.9661	15.8825	4.06592	-16801.3
(1.7, 1.8)	21255.6	392.649	91.844	19.4421	4.88717	-21254.6
(1.8, 1.9)	19395.3	19.1813	4.83633	364.528	85.9352	-19394.4
(1.9, 2.0)	12515.9	400.626	96.8275	22.7579	5.86896	-12514.9
(2.0, 2.1)	262.573	317.456	100	15.2323	5.43457	-261.601
(2.1, 2.2)	95.556	288.034	100	14.3295	5.8333	-94.5861
(2.2, 2.3)	15.2511	228.277	100	8.64593	5.03099	-14.2834
(2.3, 2.4)	56.0354	9.83588	4.39558	270.748	100	-55.0689
(2.4, 2.5)	231.81	312.63	100	14.6729	5.29025	-230.848
(2.5, 2.6)	16.2379	236.696	100	7.19877	4.03605	-15.2747
(2.6, 2.7)	6.53442	2.39199	1.86335	209.33	100	-5.57295
(2.7, 2.8)	9.21524	223.414	100	2.27665	1.58266	-8.25536
(2.8, 2.9)	16.6893	241.407	100	4.7993	2.66715	-15.7315
(2.9, 3.0)	40.4162	264.11	100	5.269	2.50505	-39.459
(3.0, 3.1)	1610.38	371.594	100	13.4444	4.01312	-1609.43
(3.1, 3.2)	387.21	334.679	100	10.1137	3.46032	-386.257

Table A.19: RunIIb parameters for $\pi^{\pm}$.

$\|\eta\|$ region	$p^{(0)}$	$p^{(1)}$	$p^{(2)}$
(0.0, 0.1)	0.831613	0.713556	0.43525
(0.1, 0.2)	0.825935	0.721598	0.45011
(0.2, 0.3)	0.836083	0.723879	0.467886
(0.3, 0.4)	0.836152	0.726506	0.473628
(0.4, 0.5)	0.834182	0.747289	0.496636
(0.5, 0.6)	0.814052	0.730109	0.465423
(0.6, 0.7)	0.807384	0.732788	0.464089
(0.7, 0.8)	0.790964	0.730379	0.456802
(0.8, 0.9)	0.840868	0.76665	0.514619
(0.9, 1.0)	0.8823	0.794124	0.5868
(1.0, 1.1)	0.919187	0.824455	0.649207
(1.1, 1.2)	1	0.830389	0.665294
(1.2, 1.3)	1	0.820269	0.630529
(1.3, 1.4)	1	0.822843	0.659627
(1.4, 1.5)	0.918494	0.856208	0.699342
(1.5, 1.6)	0.842171	0.833375	0.660859
(1.6, 1.7)	0.818045	0.823923	0.653403
(1.7, 1.8)	0.785572	0.829454	0.627739
(1.8, 1.9)	0.790509	0.824285	0.635093
(1.9, 2.0)	0.778699	0.805378	0.612033
(2.0, 2.1)	0.775646	0.812683	0.632207
(2.1, 2.2)	0.770614	0.815616	0.646852
(2.2, 2.3)	0.795324	0.826311	0.667093
(2.3, 2.4)	0.778466	0.842917	0.675825
(2.4, 2.5)	0.793996	0.836775	0.689344
(2.5, 2.6)	0.76346	0.834997	0.689795
(2.6, 2.7)	0.782275	0.843831	0.706938
(2.7, 2.8)	0.763276	0.840756	0.701997
(2.8, 2.9)	0.779813	0.857181	0.729416
(2.9, 3.0)	0.799652	0.864877	0.755364
(3.0, 3.1)	0.784406	0.870369	0.756288
(3.1, 3.2)	0.786595	0.87281	0.76595

Table A.20: RunIIb parameters for p.

$\|\eta\|$ region	$p^{(0)}$	$p^{(1)}$	$p^{(2)}$
(0.0, 0.1)	0.81782	2.39735	-2.28225
(0.1, 0.2)	0.808423	2.22588	-2.05185
(0.2, 0.3)	0.813395	2.21865	-2.04901
(0.3, 0.4)	0.80822	2.20866	-2.00896
(0.4, 0.5)	0.802207	2.04033	-1.77255
(0.5, 0.6)	0.791311	2.27537	-2.04119
(0.6, 0.7)	0.784237	2.01856	-1.64479
(0.7, 0.8)	0.771821	2.11517	-1.71898
(0.8, 0.9)	0.795281	1.79001	-1.19598
(0.9, 1.0)	0.799708	1.71113	-0.956757
(1.0, 1.1)	0.796793	1.51525	-0.524727
(1.1, 1.2)	0.875361	1.25693	-0.005628
(1.2, 1.3)	0.906721	1.28994	-0.00107515
(1.3, 1.4)	0.888806	1.28602	0.0349906
(1.4, 1.5)	0.770242	1.46238	-0.312063
(1.5, 1.6)	0.733807	1.49584	-0.412866
(1.6, 1.7)	0.716567	1.49825	-0.401074
(1.7, 1.8)	0.698403	1.50674	-0.450542
(1.8, 1.9)	0.697938	1.46829	-0.316187
(1.9, 2.0)	0.707282	1.35866	-0.0968763
(2.0, 2.1)	0.69329	1.33268	-0.0527146
(2.1, 2.2)	0.691605	1.27704	0.113181
(2.2, 2.3)	0.704159	1.22637	0.243061
(2.3, 2.4)	0.684224	1.21717	0.247778
(2.4, 2.5)	0.700408	1.18474	0.344535
(2.5, 2.6)	0.677958	1.16986	0.367125
(2.6, 2.7)	0.683771	1.13358	0.419396
(2.7, 2.8)	0.676823	1.14142	0.438307
(2.8, 2.9)	0.693387	1.10896	0.538945
(2.9, 3.0)	0.698672	1.10115	0.582812
(3.0, 3.1)	0.679426	1.12908	0.567046
(3.1, 3.2)	0.676631	1.11128	0.589528

Table A.21: RunIIb-P20ToP17 parameters for $e^{\pm}$.

$\|\eta\|$ region	$p^{(0)}$	$p^{(1)}$	$p^{(2)}$	$p^{(3)}$	$p^{(4)}$
(0.0, 0.1)	0.941208	2.50197	6.53843	-0.573548	0.100483
(0.1, 0.2)	0.94236	6.25898	10.1112	-0.73475	0.258273
(0.2, 0.3)	0.939753	2.02081	6.15205	-0.581558	0.116517
(0.3, 0.4)	0.939355	-0.750865	0.279076	5.12945	9.31557
(0.4, 0.5)	0.931738	-0.598296	0.118428	1.61778	6.3194
(0.5, 0.6)	0.936941	-0.799356	0.265318	5.05695	10.5199
(0.6, 0.7)	0.934814	-0.797671	0.273711	4.49899	10.4788
(0.7, 0.8)	0.932292	-0.845947	0.277627	4.53705	11.6054
(0.8, 0.9)	0.925836	-0.909903	0.314013	4.82553	13.8808
(0.9, 1.0)	0.93131	-0.926018	0.304888	4.76157	17.2427
(1.0, 1.1)	0.9244	-0.970689	0.314403	3.44183	19.5487
(1.1, 1.2)	0.91224	-1.74431	1.28115	6.42197	38.8477
(1.2, 1.3)	0.888362	-1.01607	0.385245	11.0101	50.5366
(1.3, 1.4)	0.692133	7.40003	15.1952	-0.931386	0.455629
(1.4, 1.5)	0.861602	-1.56442	0.614226	20.1242	44.2175
(1.5, 1.6)	0.970896	-1.33225	0.641935	16.563	20.2828
(1.6, 1.7)	0.972432	-1.44716	0.686404	21.1326	31.6004
(1.7, 1.8)	0.974323	-1.6526	0.885681	21.8145	35.0814
(1.8, 1.9)	0.973029	-1.67126	0.85434	20.9955	35.418
(1.9, 2.0)	0.967712	-1.62978	0.865498	16.9791	32.7884
(2.0, 2.1)	0.967451	16.3395	34.3826	-1.65183	0.866231
(2.1, 2.2)	0.957925	-1.76214	0.972695	16.6022	34.885
(2.2, 2.3)	0.964119	-1.71283	0.870999	16.7175	35.8345
(2.3, 2.4)	0.964546	18.3875	36.8262	-1.71251	0.922648
(2.4, 2.5)	0.959418	-1.73343	1.02167	20.8904	38.4167
(2.5, 2.6)	0.956955	30.8041	39.0965	-1.3985	0.696942
(2.6, 2.7)	0.962145	-1.31006	0.684873	127.012	100
(2.7, 2.8)	0.959515	-1.22518	0.615599	129.572	100
(2.8, 2.9)	0.95925	-1.39847	0.733814	123.388	100
(2.9, 3.0)	0.955061	-1.40952	0.693574	36.8121	46.5104
(3.0, 3.1)	0.951913	-1.40711	0.713879	36.6468	41.7348
(3.1, 3.2)	0.947723	33.423	37.2798	-1.34834	0.66137

Table A.22: RunIIb-P20ToP17 parameters for $K^{\pm}$.

$\|\eta\|$ region	$p^{(0)}$	$p^{(1)}$	$p^{(2)}$
(0.0, 0.1)	0.822076	0.799632	0.34622
(0.1, 0.2)	0.808049	0.786815	0.334145
(0.2, 0.3)	0.819156	0.798571	0.344681
(0.3, 0.4)	0.817765	0.799823	0.363268
(0.4, 0.5)	0.816417	0.797421	0.378325
(0.5, 0.6)	0.794646	0.814148	0.335414
(0.6, 0.7)	0.786573	0.808343	0.333295
(0.7, 0.8)	0.773154	0.81383	0.365289
(0.8, 0.9)	0.832335	0.840747	0.455703
(0.9, 1.0)	0.855265	0.852727	0.5189
(1.0, 1.1)	0.890293	0.873994	0.597485
(1.1, 1.2)	0.973795	0.882846	0.603278
(1.2, 1.3)	0.994319	0.870969	0.582768
(1.3, 1.4)	0.977562	0.874264	0.584566
(1.4, 1.5)	0.8805	0.893191	0.641269
(1.5, 1.6)	0.808223	0.879459	0.585071
(1.6, 1.7)	0.797291	0.874889	0.599926
(1.7, 1.8)	0.774906	0.881769	0.59243
(1.8, 1.9)	0.780374	0.881232	0.598404
(1.9, 2.0)	0.793127	0.880634	0.606451
(2.0, 2.1)	0.777857	0.886549	0.610169
(2.1, 2.2)	0.773284	0.881373	0.622128
(2.2, 2.3)	0.800675	0.887915	0.649905
(2.3, 2.4)	0.768843	0.904391	0.639293
(2.4, 2.5)	0.807279	0.90516	0.681039
(2.5, 2.6)	0.772658	0.896964	0.68035
(2.6, 2.7)	0.783928	0.900133	0.689819
(2.7, 2.8)	0.795362	0.910776	0.708762
(2.8, 2.9)	0.809461	0.91515	0.733943
(2.9, 3.0)	0.835758	0.922702	0.762291
(3.0, 3.1)	0.82255	0.922035	0.762625
(3.1, 3.2)	0.905189	0.940495	0.810406

Table A.23: RunIIb-P20ToP17 parameters for K^0_L.

$\|\eta\|$ region	$p^{(0)}$	$p^{(1)}$	$p^{(2)}$
(0.0, 0.1)	0.847435	0.734348	0.442908
(0.1, 0.2)	0.822632	0.750845	0.383657
(0.2, 0.3)	0.842629	0.752434	0.440905
(0.3, 0.4)	0.838845	0.759176	0.438263
(0.4, 0.5)	0.839197	0.775737	0.449451
(0.5, 0.6)	0.830098	0.765203	0.46619
(0.6, 0.7)	0.806772	0.758731	0.399872
(0.7, 0.8)	0.79673	0.771803	0.412971
(0.8, 0.9)	0.843158	0.789465	0.466238
(0.9, 1.0)	0.861288	0.802967	0.510634
(1.0, 1.1)	0.868608	0.831756	0.54875
(1.1, 1.2)	0.986282	0.837423	0.626934
(1.2, 1.3)	1	0.837634	0.606542
(1.3, 1.4)	0.968125	0.818877	0.611415
(1.4, 1.5)	0.833732	0.836848	0.551034
(1.5, 1.6)	0.793056	0.826622	0.541808
(1.6, 1.7)	0.785809	0.823865	0.565755
(1.7, 1.8)	0.766705	0.827388	0.548159
(1.8, 1.9)	0.77447	0.834569	0.559662
(1.9, 2.0)	0.789832	0.840919	0.587325
(2.0, 2.1)	0.778975	0.847289	0.598336
(2.1, 2.2)	0.775331	0.826051	0.621866
(2.2, 2.3)	0.814237	0.86262	0.656863
(2.3, 2.4)	0.79084	0.832672	0.672785
(2.4, 2.5)	0.8471	0.850205	0.717218
(2.5, 2.6)	0.807963	0.850922	0.713234
(2.6, 2.7)	0.850873	0.842701	0.753984
(2.7, 2.8)	0.861086	0.838132	0.768638
(2.8, 2.9)	0.912877	0.854657	0.803654
(2.9, 3.0)	0.897045	0.893337	0.796133
(3.0, 3.1)	0.852648	0.892716	0.778949
(3.1, 3.2)	0.848007	0.914506	0.778625

Table A.24: RunIIb-P20ToP17 parameters for K^0_S.

$\|\eta\|$ region	$p^{(0)}$	$p^{(1)}$	$p^{(2)}$
(0.0, 0.1)	0.849074	0.813983	0.428101
(0.1, 0.2)	0.840997	0.821527	0.429602
(0.2, 0.3)	0.848169	0.816542	0.433534
(0.3, 0.4)	0.846863	0.821912	0.438719
(0.4, 0.5)	0.846738	0.825822	0.46527
(0.5, 0.6)	0.832995	0.835638	0.443816
(0.6, 0.7)	0.83065	0.833631	0.469502
(0.7, 0.8)	0.821376	0.845741	0.483188
(0.8, 0.9)	0.878319	0.863574	0.55633
(0.9, 1.0)	0.919514	0.885853	0.614475
(1.0, 1.1)	0.957731	0.901072	0.668224
(1.1, 1.2)	1	0.898372	0.659404
(1.2, 1.3)	1	0.8888	0.638538
(1.3, 1.4)	1	0.906675	0.664877
(1.4, 1.5)	0.942078	0.910886	0.704033
(1.5, 1.6)	0.861265	0.896807	0.641138
(1.6, 1.7)	0.83916	0.894931	0.63526
(1.7, 1.8)	0.851553	0.909335	0.673894
(1.8, 1.9)	0.848346	0.914154	0.670545
(1.9, 2.0)	0.88475	0.925505	0.691777
(2.0, 2.1)	0.886906	0.948698	0.711163
(2.1, 2.2)	0.932801	0.932361	0.75732
(2.2, 2.3)	0.935081	0.970994	0.747878
(2.3, 2.4)	1	0.963662	0.794754
(2.4, 2.5)	1	0.955872	0.796785
(2.5, 2.6)	1	0.959121	0.808335
(2.6, 2.7)	1	0.966835	0.808963
(2.7, 2.8)	1	0.960957	0.813645
(2.8, 2.9)	1	0.958802	0.827472
(2.9, 3.0)	1	0.973901	0.832058
(3.0, 3.1)	1	0.958663	0.853577
(3.1, 3.2)	1	1.00235	0.832544

Table A.25: RunIIb-P20ToP17 parameters for Λ.

$\|\eta\|$ region	$p^{(0)}$	$p^{(1)}$	$p^{(2)}$
(0.0, 0.1)	0.797926	2.72782	-1.66259
(0.1, 0.2)	0.789137	2.77609	-1.73597
(0.2, 0.3)	0.7933	2.59726	-1.59521
(0.3, 0.4)	0.789276	2.70361	-1.60873
(0.4, 0.5)	0.781929	2.46835	-1.47604
(0.5, 0.6)	0.773542	2.487	-1.42649
(0.6, 0.7)	0.762494	2.5467	-1.43932
(0.7, 0.8)	0.746613	2.47935	-1.3441
(0.8, 0.9)	0.774376	2.08206	-0.992786
(0.9, 1.0)	0.78545	1.87475	-0.679358
(1.0, 1.1)	0.789941	1.56637	-0.272905
(1.1, 1.2)	0.871975	1.32697	0.118855
(1.2, 1.3)	0.896878	1.40192	0.0634329
(1.3, 1.4)	0.891974	1.3543	0.1371
(1.4, 1.5)	0.761789	1.65538	-0.216312
(1.5, 1.6)	0.728356	1.65657	-0.225436
(1.6, 1.7)	0.714133	1.64613	-0.225164
(1.7, 1.8)	0.686727	1.73468	-0.312475
(1.8, 1.9)	0.685593	1.73488	-0.279157
(1.9, 2.0)	0.690862	1.61988	-0.113617
(2.0, 2.1)	0.677435	1.60578	-0.0929344
(2.1, 2.2)	0.678874	1.47547	0.0831716
(2.2, 2.3)	0.699317	1.39671	0.232813
(2.3, 2.4)	0.677591	1.39937	0.23917
(2.4, 2.5)	0.701948	1.29965	0.368007
(2.5, 2.6)	0.670438	1.33469	0.337561
(2.6, 2.7)	0.680618	1.2944	0.400023
(2.7, 2.8)	0.676061	1.28334	0.430201
(2.8, 2.9)	0.687052	1.24476	0.504289
(2.9, 3.0)	0.710137	1.21083	0.582207
(3.0, 3.1)	0.707464	1.20276	0.599489
(3.1, 3.2)	0.723966	1.19201	0.642217

Table A.26: RunIIb-P20ToP17 parameters for $\mu^{\pm}$.

$\|\eta\|$ region	$p^{(0)}$	$p^{(1)}$	$p^{(2)}$	$p^{(3)}$
(0.0, 0.1)	-845869	2.04671e+06	-0.232835	0.0011105
(0.1, 0.2)	-2.11658e+07	4.99093e+07	-0.227739	0.00022326
(0.2, 0.3)	-1.76033e+07	4.01018e+07	-0.209657	0.000249175
(0.3, 0.4)	-1.85024e+07	4.29062e+07	-0.23602	0.000239652
(0.4, 0.5)	-4.87903e+07	1.03336e+08	-0.169521	0.000150455
(0.5, 0.6)	-3.19686e+08	6.3151e+08	-0.0860243	5.7613e-05
(0.6, 0.7)	-5.53859e+07	9.96671e+07	0.0400128	0.000135378
(0.7, 0.8)	-1.9249e+07	3.31861e+07	0.0442058	0.000231331
(0.8, 0.9)	-1.63326e+09	2.78576e+09	0.0643438	2.51734e-05
(0.9, 1.0)	-2.50201e+09	4.24116e+09	-0.143569	2.10951e-05
(1.0, 1.1)	-2.33262e+07	3.9343e+07	-0.286848	0.000225903
(1.1, 1.2)	-6.38793e+07	1.08056e+08	-0.308361	0.000165769
(1.2, 1.3)	-1.1071e+07	1.83895e+07	-0.202605	0.000412203
(1.3, 1.4)	-1.55281e+07	2.28967e+07	-0.177834	0.000386238
(1.4, 1.5)	-5.40757e+07	7.28137e+07	-0.169126	0.000196251
(1.5, 1.6)	-3.11515e+07	4.19059e+07	-0.262557	0.000267059
(1.6, 1.7)	-29539.2	36952.5	-0.205646	0.00887773
(1.7, 1.8)	-5.58374e+07	6.96855e+07	-0.0837477	0.000189689
(1.8, 1.9)	-5.25795e+07	6.71398e+07	-0.0412191	0.000186807
(1.9, 2.0)	-1.44678e+06	1.91619e+06	-0.0471874	0.00110654
(2.0, 2.1)	-4.50732e+07	5.43792e+07	0.150788	0.000192463
(2.1, 2.2)	-6.65555e+07	8.64078e+07	-0.118355	0.000168429
(2.2, 2.3)	-538.115	920.954	-0.644432	0.0572243
(2.3, 2.4)	-77.2484	131.794	-0.601185	0.14293
(2.4, 2.5)	-38.8381	67.7287	-0.720275	0.207146
(2.5, 2.6)	-46.3054	79.9272	-0.661683	0.182209
(2.6, 2.7)	-47.4294	82.0169	-0.730881	0.184437
(2.7, 2.8)	-30.7187	54.2883	-0.780982	0.226337
(2.8, 2.9)	-24.8646	43.5895	-0.788046	0.251714
(2.9, 3.0)	-20.9977	37.6603	-0.859852	0.271456
(3.0, 3.1)	-18.7364	33.2281	-0.914634	0.289458
(3.1, 3.2)	-15.973	28.6135	-0.883073	0.308064

Table A.27: RunIIb-P20ToP17 parameters for n.

$\|\eta\|$ region	$p^{(0)}$	$p^{(1)}$	$p^{(2)}$
(0.0, 0.1)	0.819053	1.38601	-1.93665
(0.1, 0.2)	0.810747	1.39458	-2.10612
(0.2, 0.3)	0.815348	1.27177	-1.83763
(0.3, 0.4)	0.811317	1.39204	-1.88061
(0.4, 0.5)	0.804553	1.23179	-1.60141
(0.5, 0.6)	0.795258	1.29914	-1.63037
(0.6, 0.7)	0.787626	1.41637	-1.95149
(0.7, 0.8)	0.771088	1.51912	-2.02873
(0.8, 0.9)	0.798688	1.23725	-1.30099
(0.9, 1.0)	0.802359	1.08887	-0.760233
(1.0, 1.1)	0.79639	0.912882	-0.359655
(1.1, 1.2)	0.884022	0.854086	0.23825
(1.2, 1.3)	0.910801	0.942055	0.168152
(1.3, 1.4)	0.888836	0.976787	0.113484
(1.4, 1.5)	0.769951	1.06522	-0.252263
(1.5, 1.6)	0.733077	1.03031	-0.388315
(1.6, 1.7)	0.722438	0.844154	0.0580221
(1.7, 1.8)	0.699138	1.04491	-0.36198
(1.8, 1.9)	0.705934	0.869743	0.0975191
(1.9, 2.0)	0.709636	0.950412	0.0707458
(2.0, 2.1)	0.704235	0.885838	0.226668
(2.1, 2.2)	0.708308	0.808864	0.382755
(2.2, 2.3)	0.737651	0.747187	0.536891
(2.3, 2.4)	0.721534	0.757522	0.555841
(2.4, 2.5)	0.755283	0.755586	0.62747
(2.5, 2.6)	0.732795	0.756355	0.64439
(2.6, 2.7)	0.750362	0.740121	0.682725
(2.7, 2.8)	0.803146	0.714062	0.766389
(2.8, 2.9)	0.855066	0.76942	0.803788
(2.9, 3.0)	0.806343	0.815401	0.771174
(3.0, 3.1)	0.833238	0.832136	0.794158
(3.1, 3.2)	0.817346	0.851286	0.789252

Table A.28: RunIIb-P20ToP17 parameters for γ.

$\lvert\eta\rvert$ region	$p^{(0)}$	$p^{(1)}$	$p^{(2)}$	$p^{(3)}$	$p^{(4)}$	$p^{(5)}$
(0.0, 0.1)	3282.62	115.073	29.2108	6.31546	1.81449	-3281.67
(0.1, 0.2)	6201.6	106.114	26.3368	6.12717	1.6771	-6200.65
(0.2, 0.3)	85.5496	2.77048	1.17129	48.4796	17.2251	-84.5962
(0.3, 0.4)	2357.06	73.675	19.653	5.27575	1.54903	-2356.12
(0.4, 0.5)	3933.14	72.9553	19.2005	5.01768	1.4001	-3932.19
(0.5, 0.6)	3684.76	106.854	27.6015	7.239	2.04577	-3683.82
(0.6, 0.7)	3285.06	80.8267	21.4583	7.16739	2.02284	-3284.12
(0.7, 0.8)	3816.65	113.463	29.6299	7.69614	2.15706	-3815.71
(0.8, 0.9)	1217.72	6.2281	1.89986	88.5661	25.5755	-1216.78
(0.9, 1.0)	5631.96	11.8692	3.23216	217.394	55.5197	-5631.01
(1.0, 1.1)	3328.05	12.7623	3.61205	267.308	70.7759	-3327.1
(1.1, 1.2)	3165.55	11.9436	3.34692	350.035	95.242	-3164.6
(1.2, 1.3)	78.2842	5.88953	2.43338	261.536	100	-77.352
(1.3, 1.4)	0.736624	0.405617	4.73105	-0.210415	0.186266	-0.0462887
(1.4, 1.5)	764.368	12.9998	4.11872	339.532	100	-763.486
(1.5, 1.6)	26631.5	12.2794	3.05281	221.215	50.5016	-26630.6
(1.6, 1.7)	16802.3	388.057	90.9661	15.8825	4.06592	-16801.3
(1.7, 1.8)	21255.6	392.649	91.844	19.4421	4.88717	-21254.6
(1.8, 1.9)	19395.3	19.1813	4.83633	364.528	85.9352	-19394.4
(1.9, 2.0)	12515.9	400.626	96.8275	22.7579	5.86896	-12514.9
(2.0, 2.1)	262.573	317.456	100	15.2323	5.43457	-261.601
(2.1, 2.2)	95.556	288.034	100	14.3295	5.8333	-94.5861
(2.2, 2.3)	15.2511	228.277	100	8.64593	5.03099	-14.2834
(2.3, 2.4)	56.0354	9.83588	4.39558	270.748	100	-55.0689
(2.4, 2.5)	231.81	312.63	100	14.6729	5.29025	-230.848
(2.5, 2.6)	16.2379	236.696	100	7.19877	4.03605	-15.2747
(2.6, 2.7)	6.53442	2.39199	1.86335	209.33	100	-5.57295
(2.7, 2.8)	9.21524	223.414	100	2.27665	1.58266	-8.25536
(2.8, 2.9)	16.6893	241.407	100	4.7993	2.66715	-15.7315
(2.9, 3.0)	40.4162	264.11	100	5.269	2.50505	-39.459
(3.0, 3.1)	1610.38	371.594	100	13.4444	4.01312	-1609.43
(3.1, 3.2)	387.21	334.679	100	10.1137	3.46032	-386.257

Table A.29: RunIIb-P20ToP17 parameters for $\pi^{\pm}$.

$\lvert\eta\rvert$ region	$p^{(0)}$	$p^{(1)}$	$p^{(2)}$
(0.0, 0.1)	0.831613	0.713556	0.43525
(0.1, 0.2)	0.825935	0.721598	0.45011
(0.2, 0.3)	0.836083	0.723879	0.467886
(0.3, 0.4)	0.836152	0.726506	0.473628
(0.4, 0.5)	0.834182	0.747289	0.496636
(0.5, 0.6)	0.814052	0.730109	0.465423
(0.6, 0.7)	0.807384	0.732788	0.464089
(0.7, 0.8)	0.790964	0.730379	0.456802
(0.8, 0.9)	0.840868	0.76665	0.514619
(0.9, 1.0)	0.8823	0.794124	0.5868
(1.0, 1.1)	0.919187	0.824455	0.649207
(1.1, 1.2)	1	0.830389	0.665294
(1.2, 1.3)	1	0.820269	0.630529
(1.3, 1.4)	1	0.822843	0.659627
(1.4, 1.5)	0.918494	0.856208	0.699342
(1.5, 1.6)	0.842171	0.833375	0.660859
(1.6, 1.7)	0.818045	0.823923	0.653403
(1.7, 1.8)	0.785572	0.829454	0.627739
(1.8, 1.9)	0.790509	0.824285	0.635093
(1.9, 2.0)	0.778699	0.805378	0.612033
(2.0, 2.1)	0.775646	0.812683	0.632207
(2.1, 2.2)	0.770614	0.815616	0.646852
(2.2, 2.3)	0.795324	0.826311	0.667093
(2.3, 2.4)	0.778466	0.842917	0.675825
(2.4, 2.5)	0.793996	0.836775	0.689344
(2.5, 2.6)	0.76346	0.834997	0.689795
(2.6, 2.7)	0.782275	0.843831	0.706938
(2.7, 2.8)	0.763276	0.840756	0.701997
(2.8, 2.9)	0.779813	0.857181	0.729416
(2.9, 3.0)	0.799652	0.864877	0.755364
(3.0, 3.1)	0.784406	0.870369	0.756288
(3.1, 3.2)	0.786595	0.87281	0.76595

Table A.30: RunIIb-P20ToP17 parameters for p.

$\lvert\eta\rvert$ region	$p^{(0)}$	$p^{(1)}$	$p^{(2)}$
(0.0, 0.1)	0.81782	2.39735	-2.28225
(0.1, 0.2)	0.808423	2.22588	-2.05185
(0.2, 0.3)	0.813395	2.21865	-2.04901
(0.3, 0.4)	0.80822	2.20866	-2.00896
(0.4, 0.5)	0.802207	2.04033	-1.77255
(0.5, 0.6)	0.791311	2.27537	-2.04119
(0.6, 0.7)	0.784237	2.01856	-1.64479
(0.7, 0.8)	0.771821	2.11517	-1.71898
(0.8, 0.9)	0.795281	1.79001	-1.19598
(0.9, 1.0)	0.799708	1.71113	-0.956757
(1.0, 1.1)	0.796793	1.51525	-0.524727
(1.1, 1.2)	0.875361	1.25693	-0.005628
(1.2, 1.3)	0.906721	1.28994	-0.00107515
(1.3, 1.4)	0.888806	1.28602	0.0349906
(1.4, 1.5)	0.770242	1.46238	-0.312063
(1.5, 1.6)	0.733807	1.49584	-0.412866
(1.6, 1.7)	0.716567	1.49825	-0.401074
(1.7, 1.8)	0.698403	1.50674	-0.450542
(1.8, 1.9)	0.697938	1.46829	-0.316187
(1.9, 2.0)	0.707282	1.35866	-0.0968763
(2.0, 2.1)	0.69329	1.33268	-0.0527146
(2.1, 2.2)	0.691605	1.27704	0.113181
(2.2, 2.3)	0.704159	1.22637	0.243061
(2.3, 2.4)	0.684224	1.21717	0.247778
(2.4, 2.5)	0.700408	1.18474	0.344535
(2.5, 2.6)	0.677958	1.16986	0.367125
(2.6, 2.7)	0.683771	1.13358	0.419396
(2.7, 2.8)	0.676823	1.14142	0.438307
(2.8, 2.9)	0.693387	1.10896	0.538945
(2.9, 3.0)	0.698672	1.10115	0.582812
(3.0, 3.1)	0.679426	1.12908	0.567046
(3.1, 3.2)	0.676631	1.11128	0.589528

Appendix B

Notes on fitting

Here we describe the Gauss-Newton method utilized in the determination of the fit parameters A, B and C for R_h^{data} via the p_{T}-balance method. Our implementation makes use of analytical results for the relevant derivatives. This decreases the amount of function evaluations needed in the 3-dimensional parameter space in comparison to more elementary numerical stencils. Efficiency considerations are needed due to the independent nature of the study requiring all computations to be performed using local resources. The method also motivates the fit parameter uncertainties by clearly linking them with hyperspace curvature.

Let us first recall the ordinary Newton's method in function minimization. Suppose a function $f : \mathbb{R}^k \to \mathbb{R}, k \in \mathbb{N}$ has a minimum at the point $\boldsymbol{x}_n$. The vectors in the fit parameter space shall be denoted by boldface font. We seek to find this point by an iterative algorithm, where the m:th point is obtained from the $m-1$:th by a small step $\delta\boldsymbol{x}_{m-1}$ such that $\boldsymbol{x}_m = \boldsymbol{x}_{m-1} + \delta\boldsymbol{x}_{m-1}$. We may then Taylor expand $f(\boldsymbol{x}_n) = f(\boldsymbol{x}_{n-1} + \delta\boldsymbol{x}_{n-1})$ about the minimum as

$$f(\boldsymbol{x}_{n-1} + \delta\boldsymbol{x}_{n-1}) = f(\boldsymbol{x}_{n-1}) + (\partial_i f(\boldsymbol{x}_{n-1}))\, \delta x^i_{n-1} + \mathcal{O}(2). \tag{B.1}$$

The gradient of f must vanish at the minimum $\boldsymbol{x}_n$, so that $\partial_j f(\boldsymbol{x}_n) = 0$. Dropping the second and higher order terms $\mathcal{O}(2)$ and differentiating both sides of Eq. (B.1), we get

$$0 = \partial_j f(\boldsymbol{x}_{n-1}) + (\partial_j \partial_i f(\boldsymbol{x}_{n-1}))\, \delta x^i_{n-1}, \tag{B.2}$$

where $\partial_j \partial_i f(\boldsymbol{x}) \equiv H_{ji}$ are the elements of the *Hessian matrix*. It's inverse has the components $(H^{-1})_{ji}$ such that $(H^{-1})_{ji} H^{ik} = \delta^k_j$, where δ^k_j is the Kroenecker delta. Solving Eq. (B.2) for the step δx^i_{n-1} results in

$$\delta x^i_{n-1} = -(H^{-1})^{ji} \partial_j f(\boldsymbol{x}_{n-1}).$$

Now that we may find the point $\boldsymbol{x}_n$ from information obtainable at $\boldsymbol{x}_{n-1}$, we construct the iterative formula

$$x^i_n = x^i_{n-1} - (H^{-1})^{ji} \partial_j f(\boldsymbol{x}_{n-1}).$$

B.1 The Gauss-Newton method

In the fitting process, we look at p_{T}-balance profiles. Essentially, they are two-dimensional histograms in $(E', p_{\mathrm{T}}^{\mathrm{probe}}/p_{\mathrm{T}}^{\mathrm{tag}})$-space, divided into bins along the E'-axis. The $p_{\mathrm{T}}^{\mathrm{probe}}/p_{\mathrm{T}}^{\mathrm{tag}}$ value of each E'-bin results from averaging over the values calculated for each event in that particular E'-bin. Let us write the DØ detector data point to be compared to the n:th bin in this space as d_n and its uncertainty as σ_n. Suppose we have N_n^{evt} events in the n:th E'-bin. Our computations are done utilizing ROOT TProfile histograms, which use automatic weighing by the number of events in a bin. Then the square sum

$$\chi^2 = \sum_{n\in E'\text{-bins}} \frac{1}{\sigma_n^2} \left(\left(\frac{1}{N_n^{\mathrm{evt}}} \sum_{k\in\{^{\mathrm{Events}}_{\mathrm{in}\ n}\}} \frac{p_{\mathrm{T}(k)}^{\mathrm{probe}}}{p_{\mathrm{T}(k)}^{\mathrm{tag}}} \right) - d_n \right)^2 \tag{B.3}$$

is a function in the three-dimensional parameter space spanned by the three parameters A, B, C of the hadron data response given in Eq. (4.10). Let us denote the partial derivatives in the Euclidean A, B, C-space by $\partial_i \doteq (\partial_A, \partial_B, \partial_C)$. It was assured in the course of the simulations that the generator level probe direction equals the reconstructed probe direction to a good approximation. As the jet energy estimator E' is found using the photon response for the tag object and generator level probe direction, it is independent of the fit parameters A, B and C. Furthermore, also the E'-binning is left invariant under a change in the fit parameters. Therefore only the term $p_{\mathrm{T}}^{\mathrm{probe}}$ in Eq. (B.3) depends on R_h^{data} and thus on the parameters (A, B, C). Hence we have the following first derivatives

$$\partial_i \chi^2 = \sum_{n\in E'\text{-bins}} \frac{2}{\sigma_n^2} \left(\left(\frac{1}{N_n^{\mathrm{evt}}} \sum_{k\in\{^{\mathrm{Events}}_{\mathrm{in}\ n}\}} \frac{p_{\mathrm{T}(k)}^{\mathrm{probe}}}{p_{\mathrm{T}(k)}^{\mathrm{tag}}} \right) - d_n \right) \left(\frac{1}{N_n^{\mathrm{evt}}} \sum_{k'\in\{^{\mathrm{Events}}_{\mathrm{in}\ n}\}} \frac{\partial_i p_{\mathrm{T}(k')}^{\mathrm{probe}}}{p_{\mathrm{T}(k')}^{\mathrm{tag}}} \right), \tag{B.4}$$

where

$$\begin{aligned}
\partial_i p_{\mathrm{T}(k')}^{\mathrm{probe}} &= \partial_i \sqrt{\left(p_{x(k')}^{\mathrm{probe}}\right)^2 + \left(p_{y(k')}^{\mathrm{probe}}\right)^2} \\
&= \frac{1}{2p_{\mathrm{T}(k')}^{\mathrm{probe}}} \left(2p_{x(k')}^{\mathrm{probe}} \partial_i p_{x(k')}^{\mathrm{probe}} + 2p_{y(k')}^{\mathrm{probe}} \partial_i p_{y(k')}^{\mathrm{probe}} \right) \\
&= \frac{p_{x(k')}^{\mathrm{probe}}}{p_{\mathrm{T}(k')}^{\mathrm{probe}}} \left(\sum_{l\in\{^{\mathrm{Hadrons}}_{\mathrm{in\ jet}\ k'}\}} p_{x(l)}^{\mathrm{gen}} \partial_i R_h^{\mathrm{data}}(E_l) \right) + \frac{p_{y(k')}^{\mathrm{probe}}}{p_{\mathrm{T}(k')}^{\mathrm{probe}}} \left(\sum_{l'\in\{^{\mathrm{Hadrons}}_{\mathrm{in\ jet}\ k'}\}} p_{y(l')}^{\mathrm{gen}} \partial_i R_h^{\mathrm{data}}(E_{l'}) \right).
\end{aligned}$$

Here we need the first derivatives of the hadron data response of Eq. (4.10). They are given by

$$\partial_A R_h^{\mathrm{data}} = -C p_h^{(0)} p_h^{(1)} (4E/3)^{p_h^{(2)}+B-1},$$

$$\begin{aligned}\partial_B R_h^{\text{data}} &= -AC p_h^{(0)} p_h^{(1)} \partial_B (4E/3)^{p_h^{(2)}+B-1} \\ &= -AC p_h^{(0)} p_h^{(1)} (4E/3)^{p_h^{(2)}-1} \partial_B e^{B\ln(4E/3)} \\ &= -AC p_h^{(0)} p_h^{(1)} (4E/3)^{p_h^{(2)}+B-1} \ln(4E/3),\end{aligned}$$

and

$$\partial_C R_h^{\text{data}} = p_h^{(0)} \left(1 - A p_h^{(1)} (4E/3)^{p_h^{(2)}+B-1}\right).$$

The second derivatives of χ^2 give the elements of the Hessian matrix

$$H_{ji} \equiv \partial_j \partial_i \chi^2 = \sum_{n \in E'\text{-bins}} \frac{2}{\sigma_n^2} \left(\frac{1}{N_n^{\text{evt}}} \sum_{k \in \{\substack{\text{Events} \\ \text{in } n}\}} \frac{\partial_j p_{\text{T}(k)}^{\text{probe}}}{p_{\text{T}(k)}^{\text{tag}}} \right) \left(\frac{1}{N_n^{\text{evt}}} \sum_{k' \in \{\substack{\text{Events} \\ \text{in } n}\}} \frac{\partial_i p_{\text{T}(k')}^{\text{probe}}}{p_{\text{T}(k')}^{\text{tag}}} \right) \tag{B.5}$$

$$+ \sum_{n' \in E'\text{-bins}} \frac{2}{\sigma_{n'}^2} \left(\left(\frac{1}{N_n^{\text{evt}}} \sum_{k'' \in \{\substack{\text{Events} \\ \text{in } n'}\}} \frac{p_{\text{T}(k'')}^{\text{probe}}}{p_{\text{T}(k'')}^{\text{tag}}} \right) - d_{n'} \right) \sum_{k''' \in \{\substack{\text{Events} \\ \text{in } n'}\}} \frac{\partial_j \partial_i p_{\text{T}(k''')}^{\text{probe}}}{N_n^{\text{evt}} p_{\text{T}(k''')}^{\text{tag}}}. \tag{B.6}$$

The Gauss-Newton algorithm differs here from the ordinary Newton's method by dropping line (B.6) due to the presence of the second partial derivatives of $p_{\text{T}}^{\text{probe}}$. Hence, the Hessian is approximated only by the line (B.5). Mathematically speaking, this amounts to assuming that the reconstructed probe p_{T} should change sufficiently little with respect to a small change in the fit parameters. From the computational physicist's viewpoint, the demonstration of the validity of such an assumption is left as a practical matter: the algorithm must converge to a good fit result, and its success may be evaluated by overlaying the fit with the detector data. In case the fit fails to converge or only poor agreement is shown, one must look for possible correction terms or resort to alternative algorithms. However, such fallbacks did not occur in the studies reported here.

B.2 Fit convergence and degrees of freedom

As a remark to the above discussion, we calculate the LSQ sum divided by the number of degrees of freedom, χ^2/n_{DOF}, where n_{DOF} is the amount of detector data points to fit to minus the amount of free fit parameters. In our case, C is constrained so there are only two free parameters. The fit is considered converged if either χ^2/n_{DOF} gets below[1] 1 or when step size gets below 10^{-6}, indicating that the fit is not proceeding any further.

[1] technically one should adjust χ^2/n_{DOF} to the vicinity of 1 instead of below, but in practice the steps get progressively smaller as χ^2/n_{DOF} approaches 1.

B.3 Propagating the fit parameter uncertainties

To determine the uncertainties in the parameters A, B and C, we follow the procedure presented in [73]. Having first calculated the Hessian with the resulting fit parameters, we then take its inverse to obtain the covariance matrix. Writing $(H^{-1})_{ij} \equiv \sigma_{ij}$ and $(H^{-1}1)_{ii} \equiv \sigma_i^2$, we propagate the uncertainties in the fit parameter determination to F as

$$\begin{aligned}\sigma_{F,\text{ syst.}} =& \sqrt{(H^{-1})^{ij}(\partial_i F)(\partial_j F)} \\ =& \big(|\partial_A F|^2\sigma_A^2 + |\partial_B F|^2\sigma_B^2 + |\partial_C F|^2\sigma_C^2 \\ &+ (\partial_A F)(\partial_B F)\sigma_{AB} + (\partial_A F)(\partial_C F)\sigma_{AC} + (\partial_B F)(\partial_C F)\sigma_{BC}\big)^{1/2}.\end{aligned}$$

The last three terms inside the square root serve to take into account the correlations between the fit parameters. The partial derivatives of F are given by

$$\partial_k F = \frac{\sum_{i\in\{\text{in jet}}^{\text{Particles}\}} E_i^{\text{gen}} \partial_k R^{\text{data}}(E_i)}{\sum_{j\in\{\text{in jet}}^{\text{Particles}\}} E_j^{\text{gen}} R^{\text{MC}}(E_j)}. \tag{B.7}$$

We take the uncertainty in the fit parameters A, B and C to be the source of systematic uncertainty of F. To obtain the total uncertainty in F, we sum the systematic and statistical uncertainties in quadrature.

Appendix C

Details on probe jet particle composition

Here we give all probe jet composition plots for reference. Fig. C.1 and Fig. C.2 show the particle content of the PYTHIA 6 γ+jet and EM+jet samples. The b-enriched PYTHIA 6 samples' probe compositions are depicted in Fig. C.3 and Fig. C.4. Finally, Fig. C.5 along with Fig. C.6 illustrate the compositions of the HERWIG 7 samples.

For completeness, the particle compositions are given at three levels of reconstruction: at generator level (gen), after applying the R^{MC} SPR responses (MC SPR) and after applying the R^{data} responses (Fit). Notice however that we have included also the neutrinos and muons in these histograms, albeit they are generally dropped from the jets even at gen level calculations. These plots however aim to give a physical picture of the nature of the processes involved in the samples. The strange baryons, for which we had no SPR parametrizations from DØ, contribute to the section entitled *other*. Further information on the fractions of different particle types to the *other* section on a separate panel next to the corresponding general composition plot. The reconstructions are done using the SPR parameters for run IIa, since this is the case in which our results bear the most resemblance to those of DØ out of all the run II epochs considered throughout the thesis.

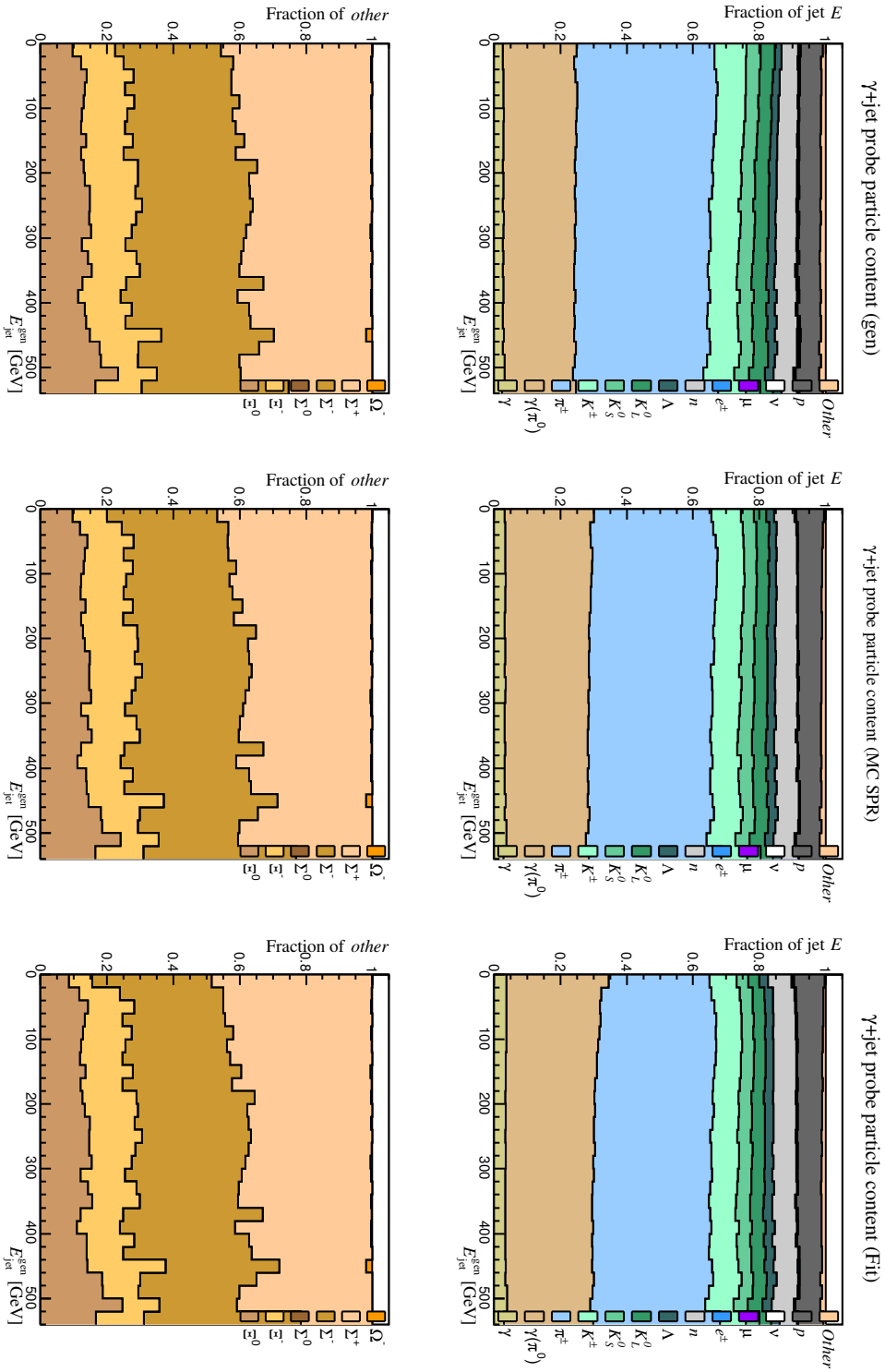

Figure C.1: Probe jet particle contents in the PYTHIA 6 γ+jet sample.

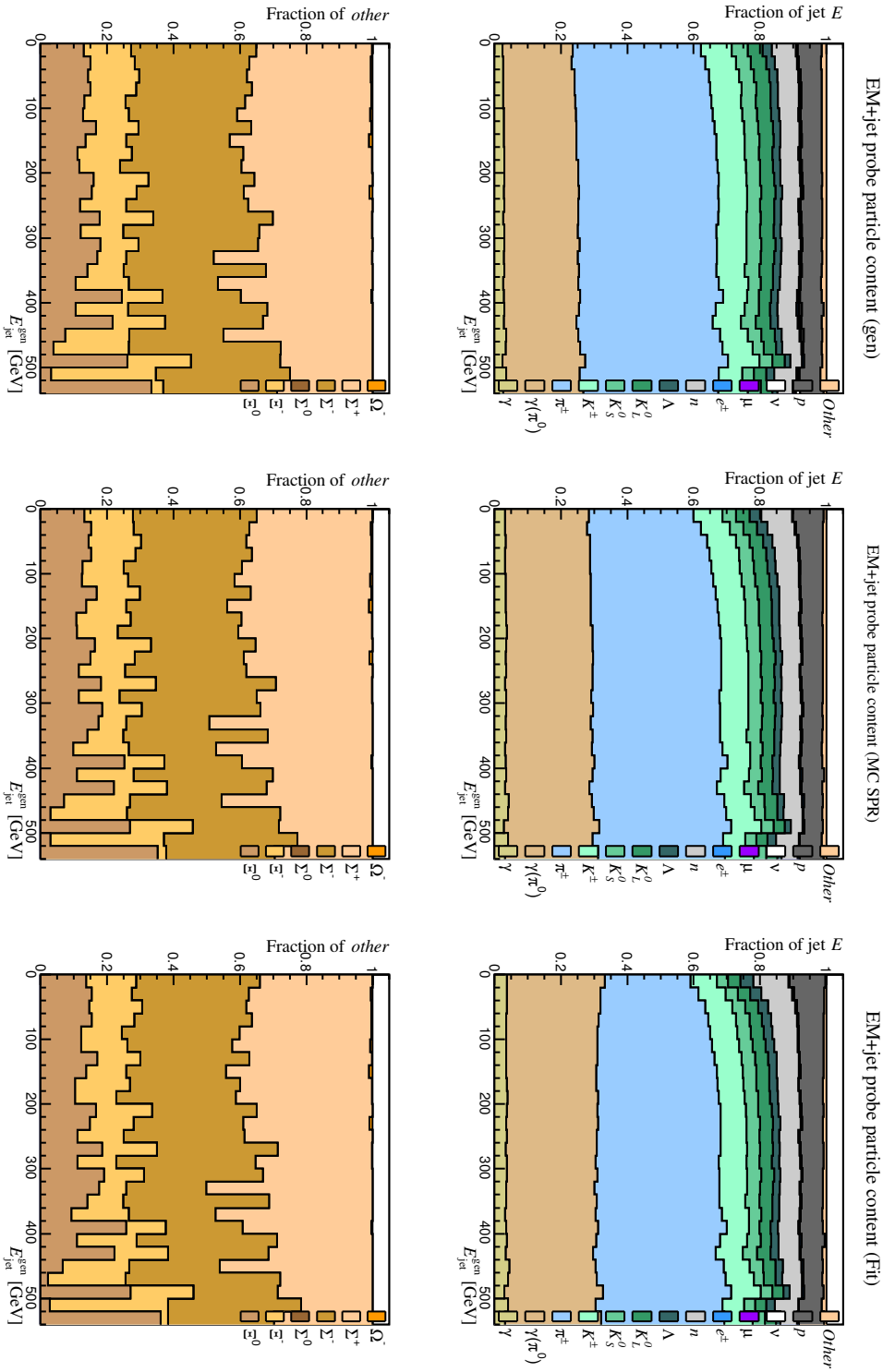

Figure C.2: Probe jet particle contents in the PYTHIA 6 EM+jet sample.

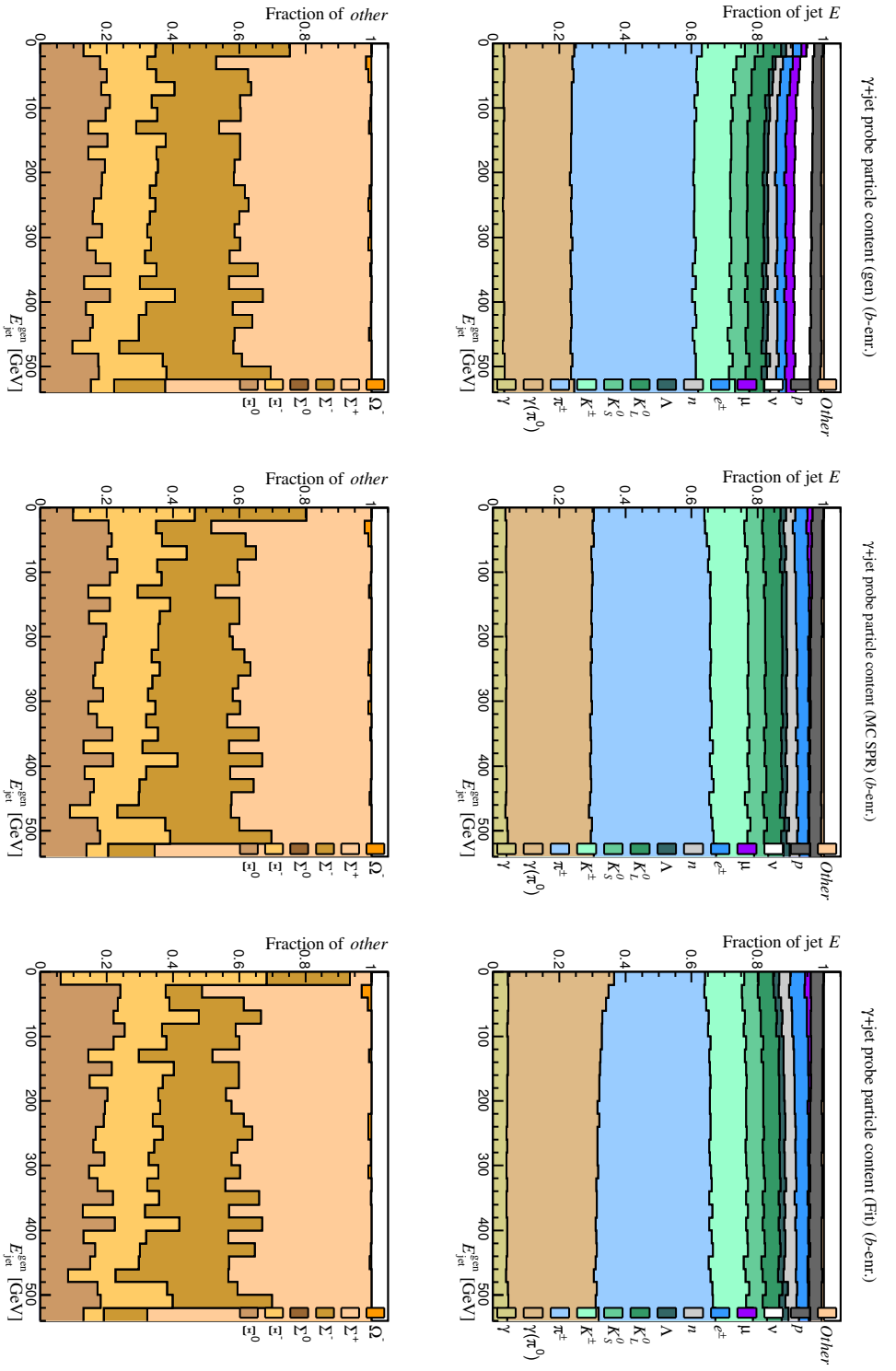

Figure C.3: Probe jet particle contents in the b-enriched PYTHIA 6 γ+jet sample.

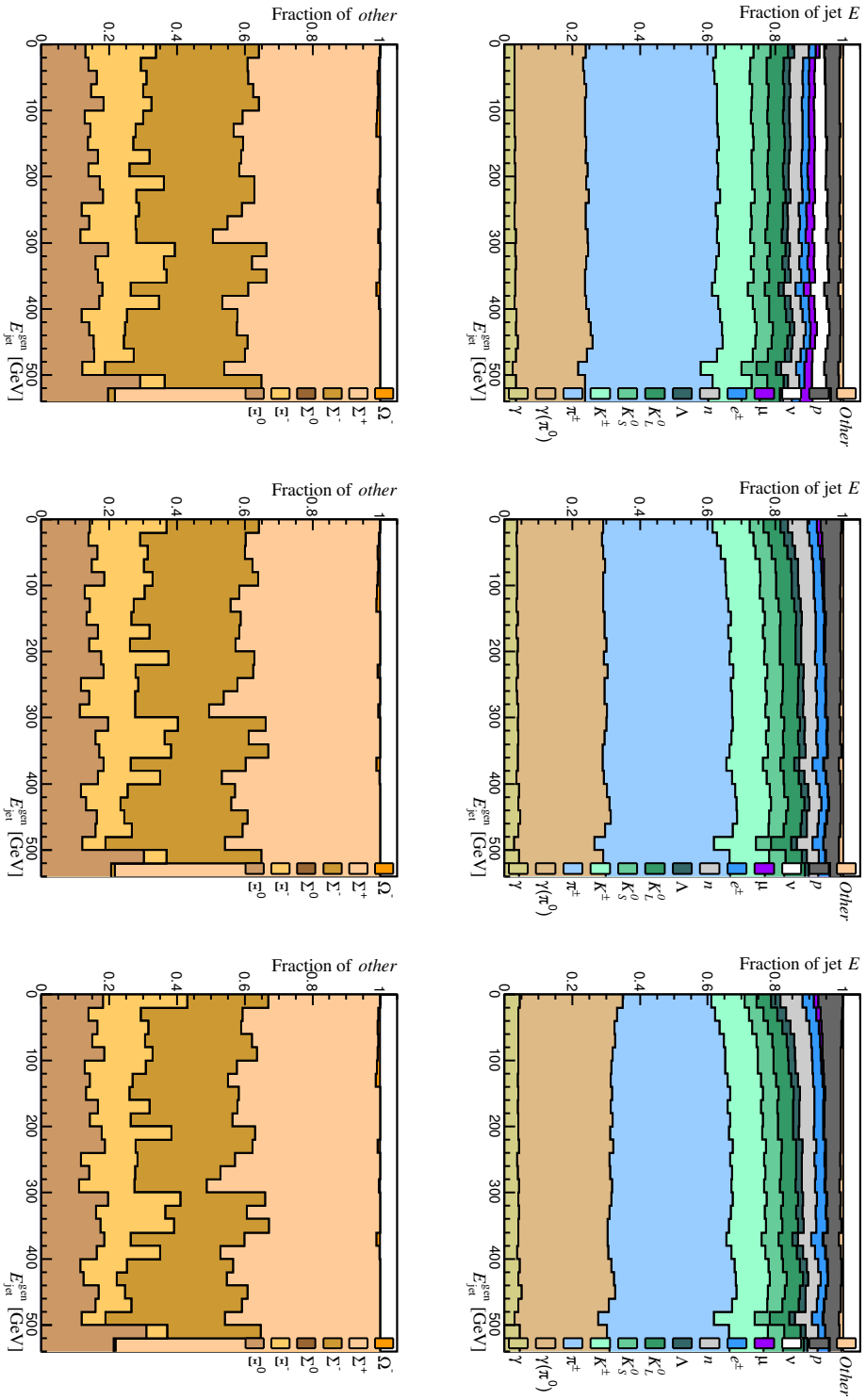

Figure C.4: Probe jet particle contents in the b-enriched PYTHIA 6 EM+jet sample.

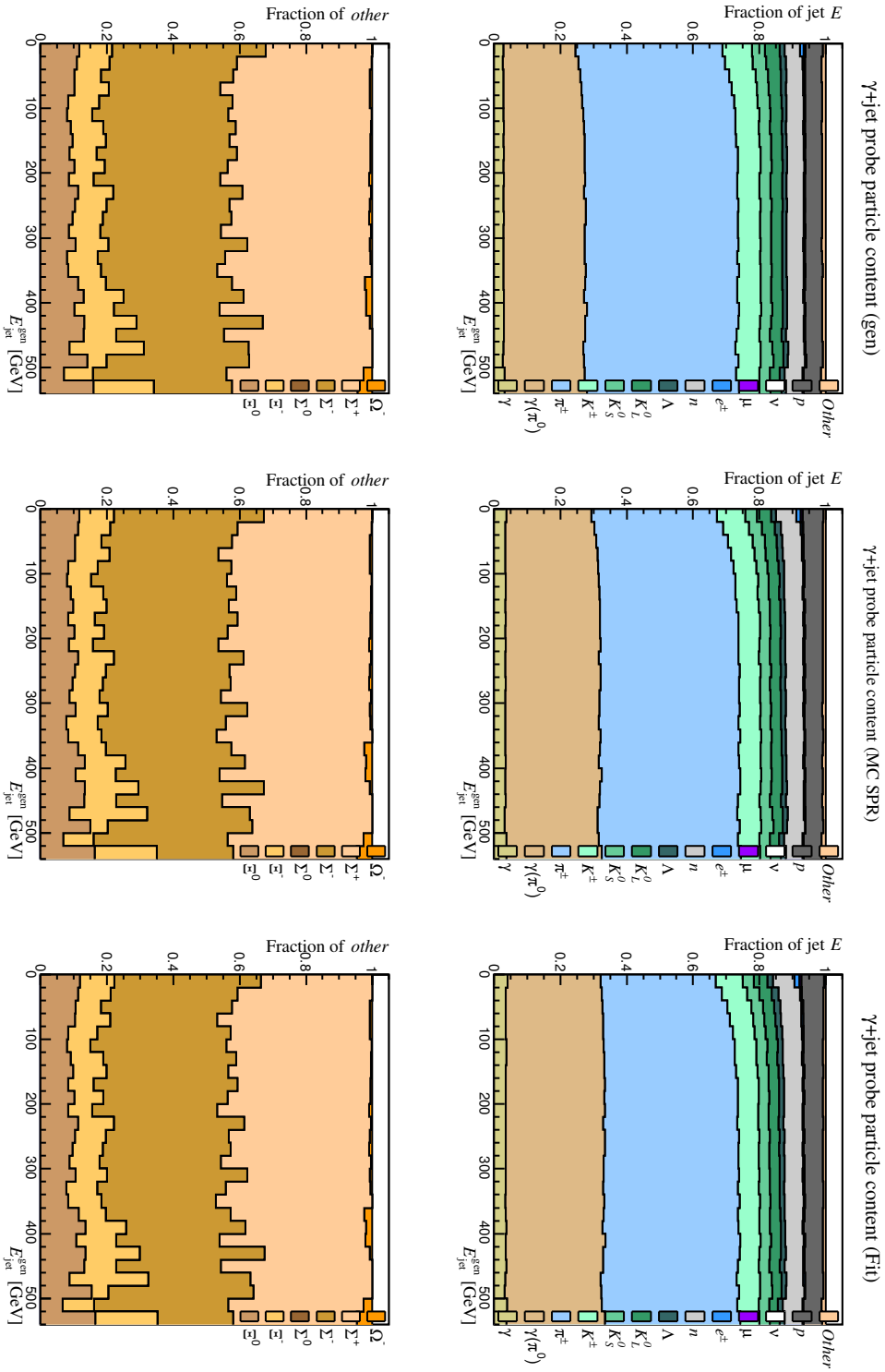

Figure C.5: Probe jet particle contents in the HERWIG 7 γ+jet samples.

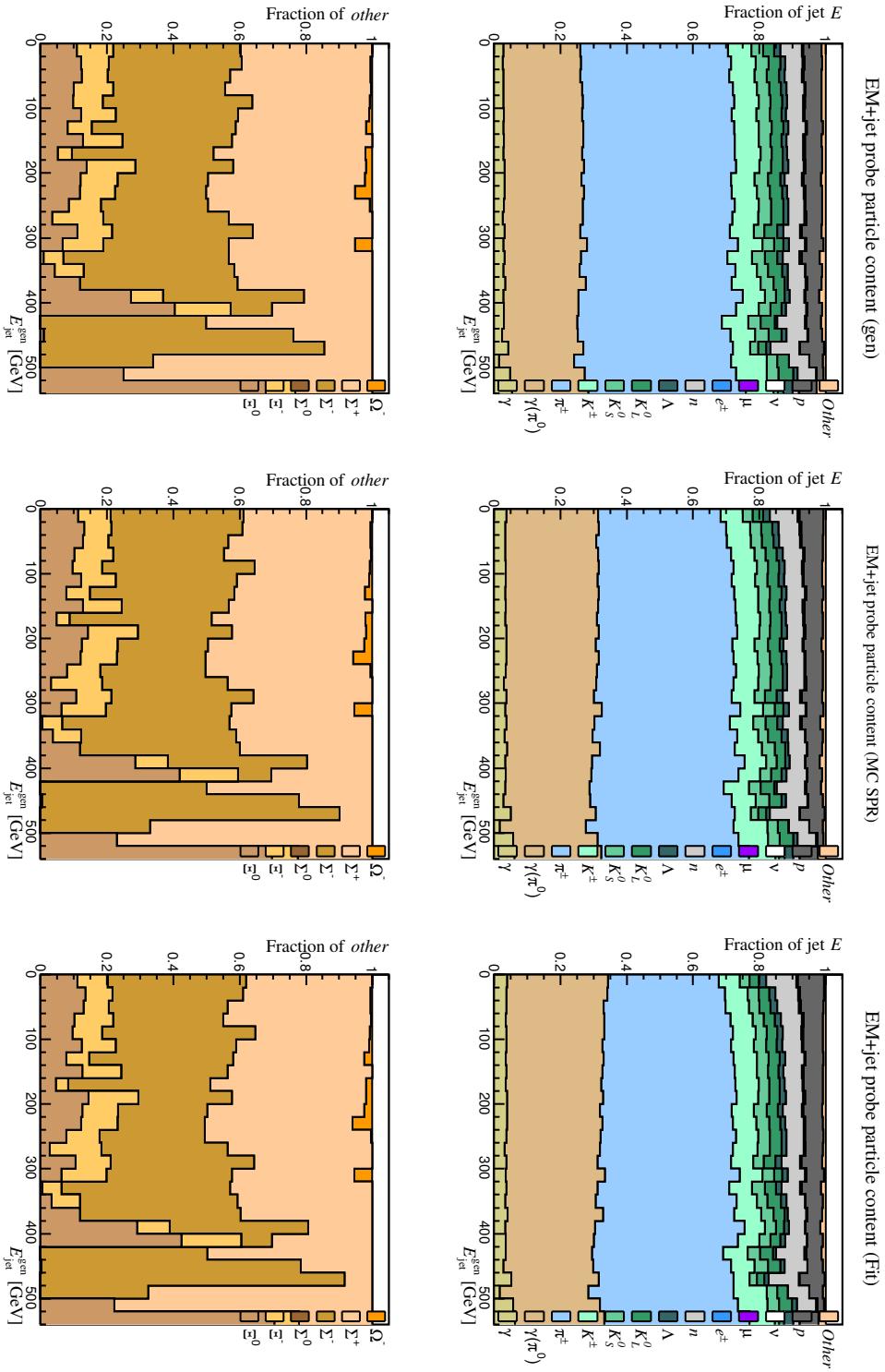

Figure C.6: Probe jet particle contents in the HERWIG 7 EM+jet sample.

Appendix D

Additional p_{T}-balance plots

Here we have included additional comparisons of our PYTHIA 6 and HERWIG 7 MC simulations (histogram lines) and the DØ PYTHIA 6 MC (open circles). and DØ detector data (filled circles) to our MC reconstructed using R^{data} with DØ fit parameters A, B, C given in [40] (filled diamonds). The PYTHIA 6 simulation comparisons are shown for run IIb2 and IIb3-4 in Fig. D.1. Comparisons of the DØ detector data points and our R^{data} reconstructed MC samples using DØ fit parameters A, B, C are shown in Fig. D.2 for runs IIb2 and IIb3-4. Our fits for these runs are shown in Fig. D.3.

Fig. D.4 contains comparisons of our HERWIG 7 MC and the DØ PYTHIA 6. The reader is advised to bear in mind that complete agreement is not expected for the plots comparing two generators. Rather, they serve as a demonstration of the magnitude of the difference between the overall energy scales between the PYTHIA 6 and HERWIG 7 samples. The results of fitting our HERWIG 7 simulations to DØ detector data are portrayed in Fig. D.5.

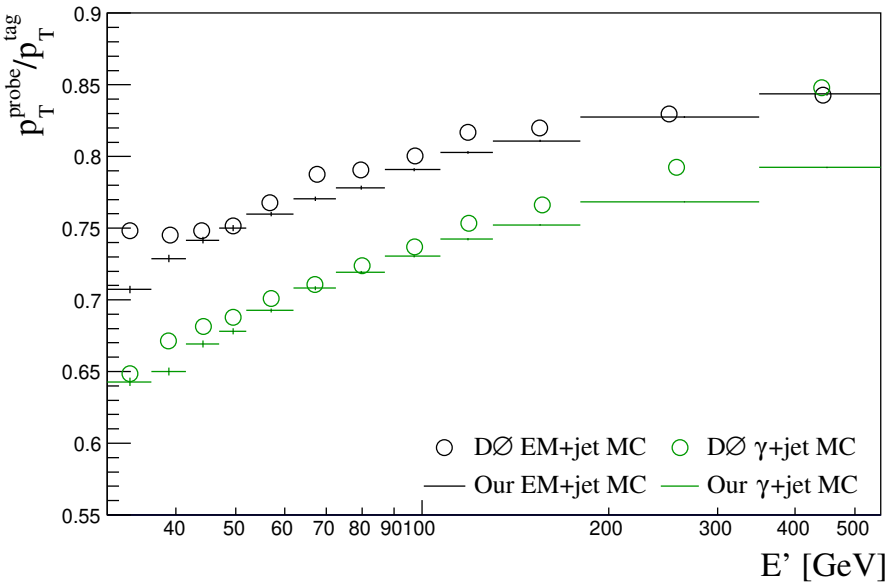

(a) P6 run IIb2

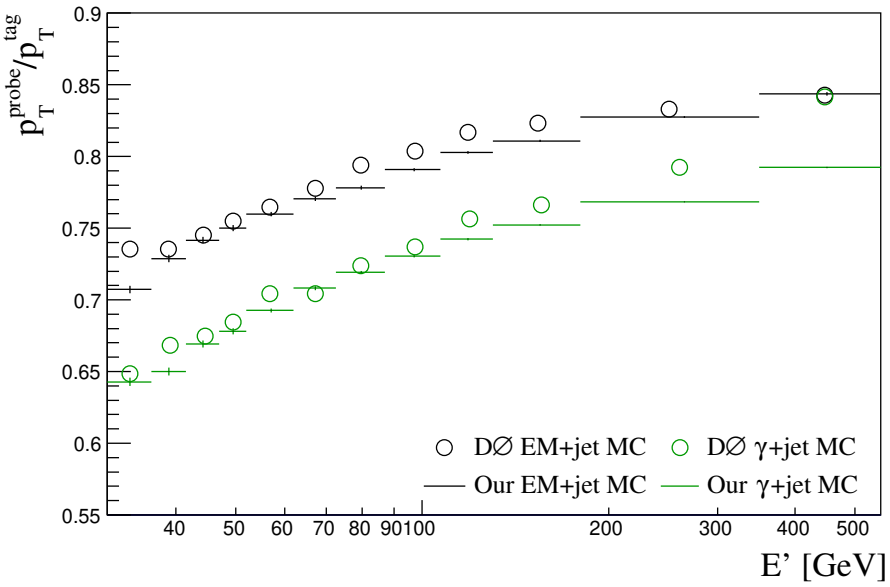

(b) P6 run IIb3-4

Figure D.1: A reproduction of the DØ run IIb3-4 p_T-balance for PYTHIA 6.

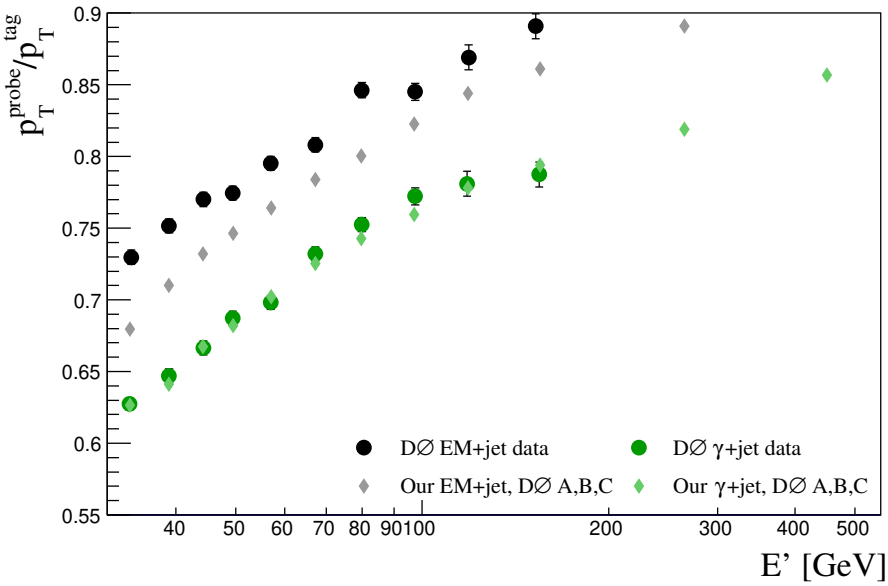

(a) P6 run IIb2

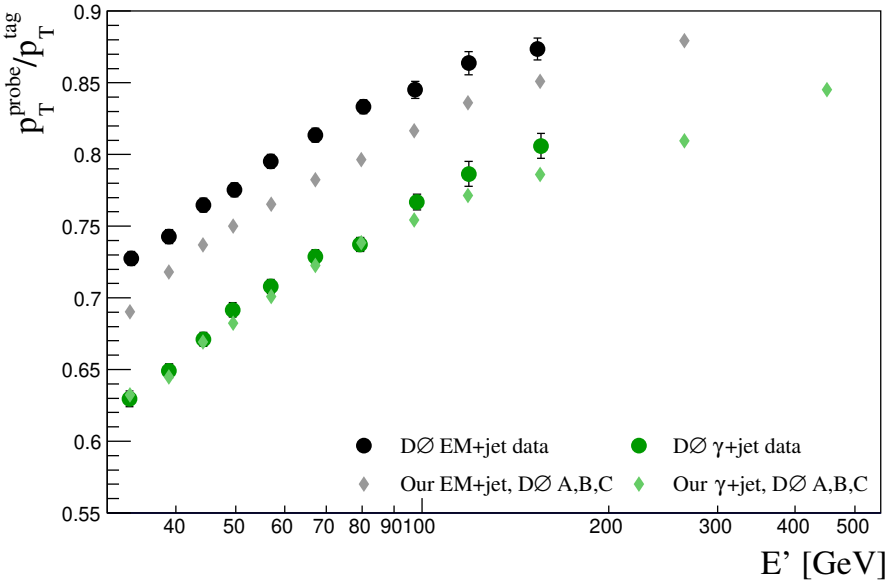

(b) P6 run IIb3-4

Figure D.2: A reproduction of the DØ run IIb3-4 p_T-balance for PYTHIA 6.

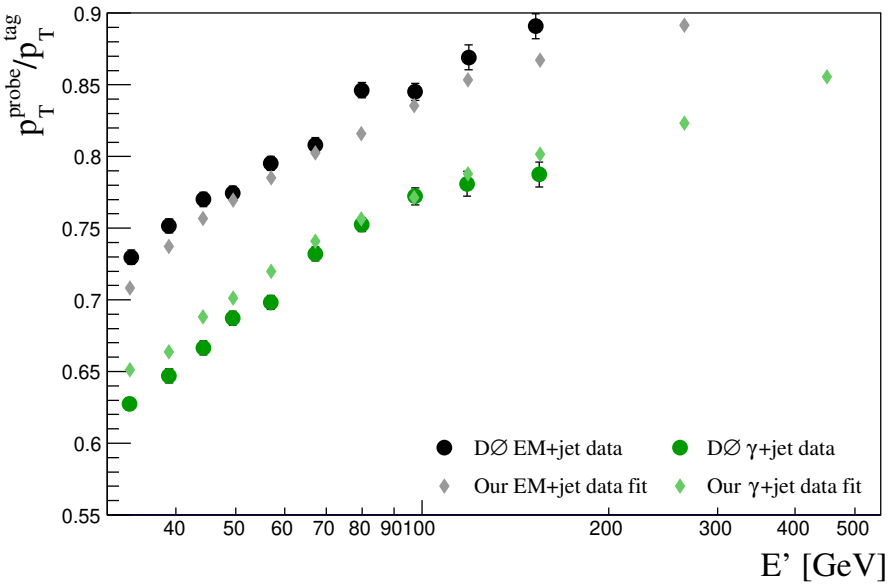

(a) P6 run IIb2

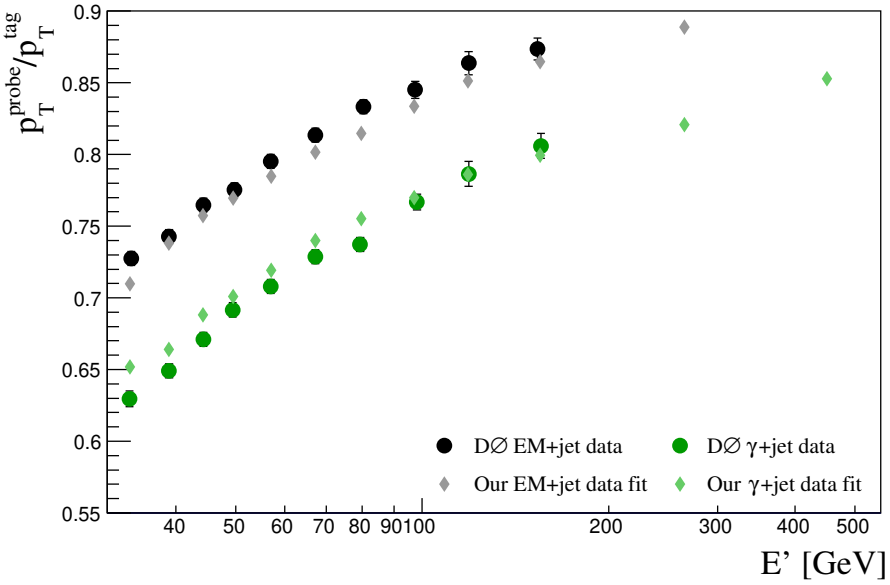

(b) P6 run IIb3-4

Figure D.3: Our PYTHIA 6 p_T-balance fit to DØ detector data.

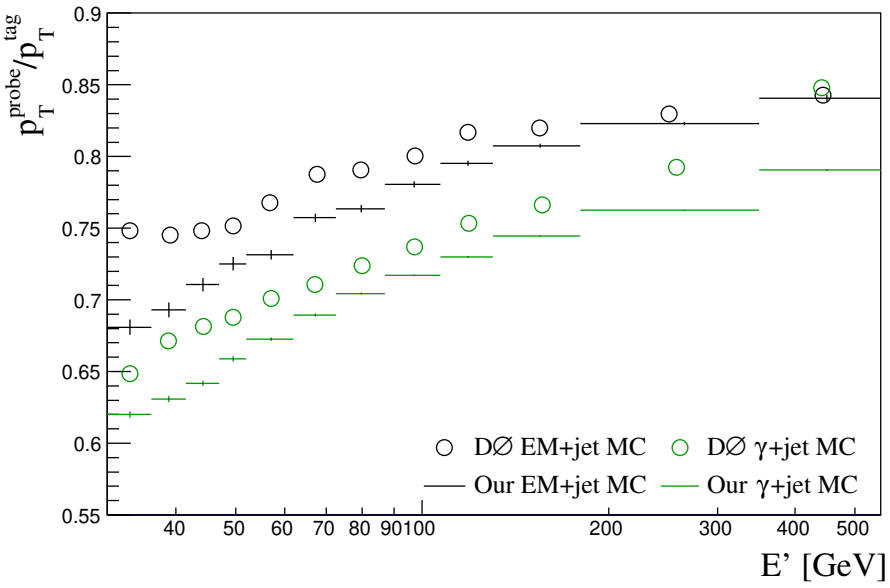

(a) H7 run IIb2

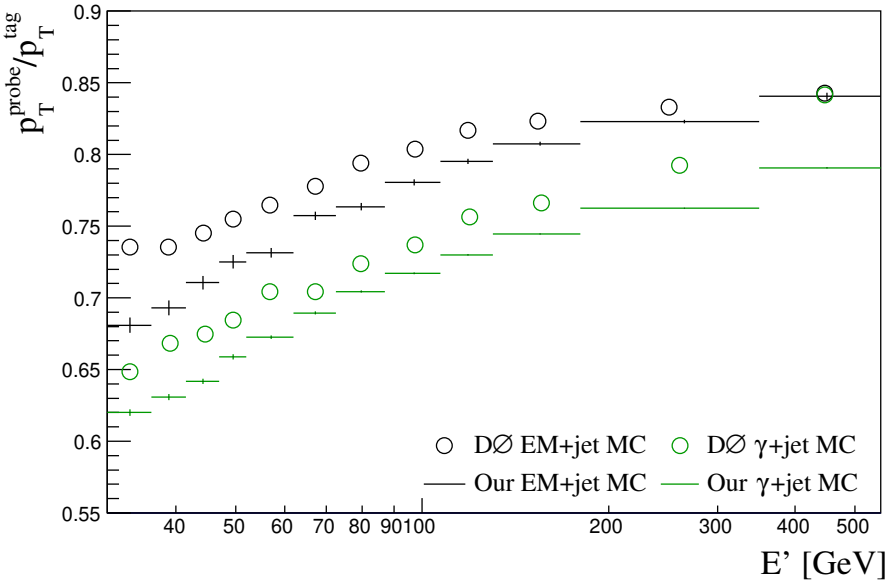

(b) H7 run IIb3-4

Figure D.4: Our HERWIG 7 p_T-balance MC compared to DØ PYTHIA 6 MC.

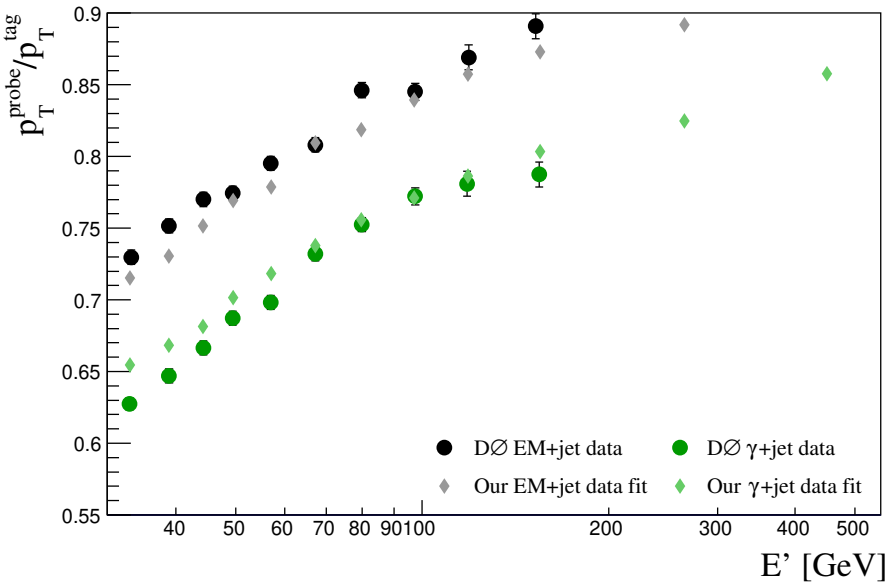

(a) H7 run IIb2

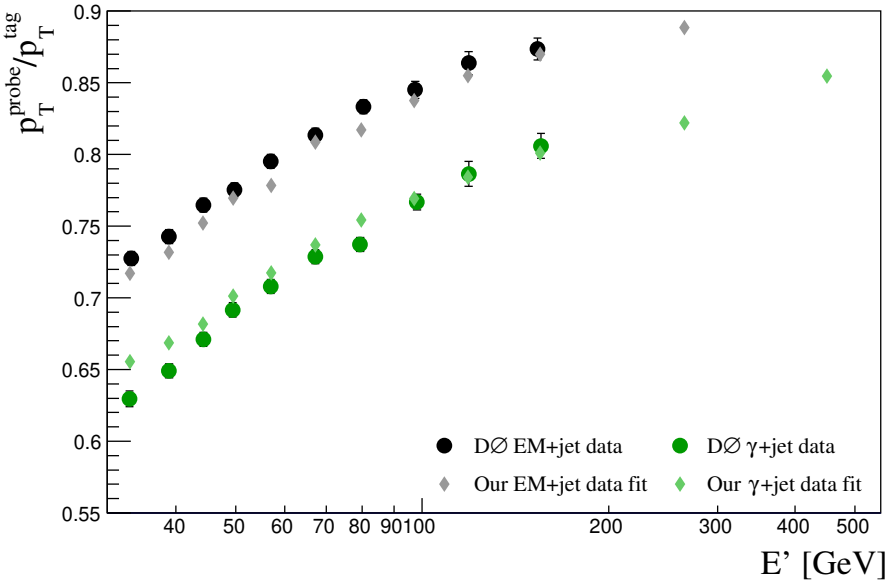

(b) H7 run IIb3-4

Figure D.5: Our HERWIG 7 p_T-balance fit to DØ detector data points.

Appendix E

Additional plots on reproducing the DØ F and F_{corr}

For completeness, we show here the remaining F and F_{corr} plots resulting from using the DØ A, B, C values from [40] in our MC samples. Fig. E.1 illustrates the case of run IIb2, whereas run IIb3-4 is shown in Fig. E.2. The agreement is on par with the run IIb1 comparisons presented in chapter 5. However, for unexplained reasons the DØ run IIb3-4 histograms reported in [40] have more fluctuation and larger bin sizes than the other runs.

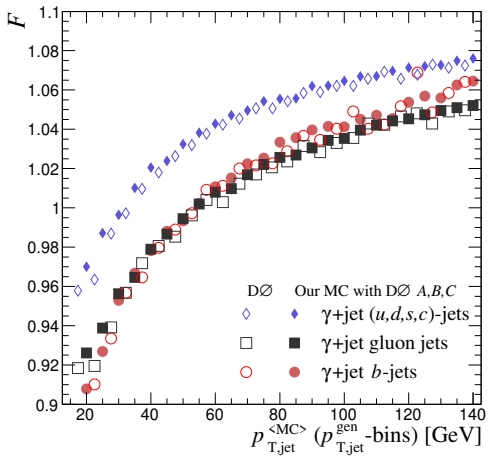

(a) F (IIb2)

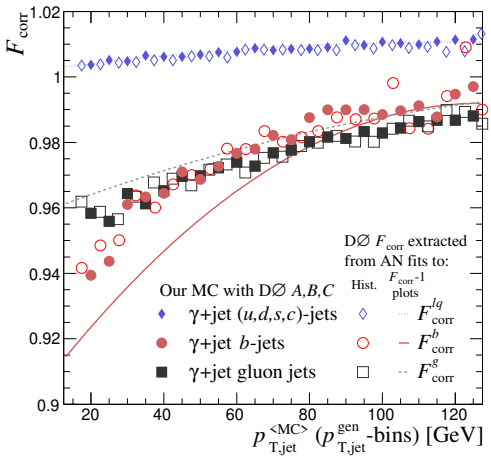

(b) $F_{\text{corr}} = F/\langle F\rangle_{\gamma+\text{jet}}$ (IIb2)

Figure E.1: The correction factors F and F_{corr} for different flavours, obtained by applying DØ fit parameters A, B, C given in [40] to our MC. The open markers are DØ histograms and the curves are the DØ fits, both extracted from [40]. The filled markers are our reproduction.

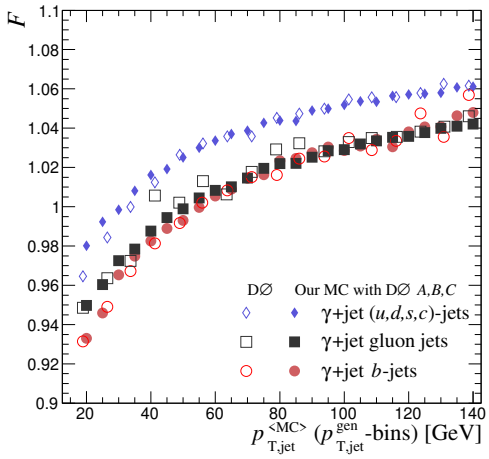

(a) F (IIb3-4)

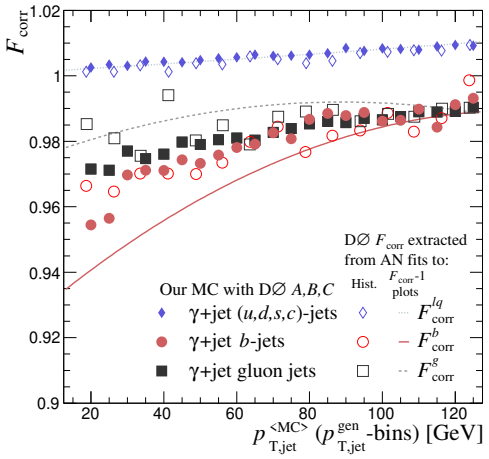

(b) $F_{\text{corr}} = F/\langle F\rangle_{\gamma+\text{jet}}$ (IIb3-4)

Figure E.2: The correction factors F and F_{corr} for different flavours, obtained by applying DØ fit parameters A, B, C given in [40] to our MC. The open markers are DØ histograms and the curves are the DØ fits, both extracted from [40]. The filled markers are our reproduction.

Bibliography

[1] S. Abachi et al. "Observation of the Top Quark". In: *Phys. Rev. Lett.* 74 (14 Apr. 1995), pp. 2632–2637. DOI: 10.1103/PhysRevLett.74.2632. URL: https://link.aps.org/doi/10.1103/PhysRevLett.74.2632.

[2] The CMS collaboration. *Top mass summary*. 2017. URL: https://twiki.cern.ch/twiki/pub/CMSPublic/PhysicsResultsTOPSummaryFigures/topmass_cms.pdf.

[3] Serguei Chatrchyan et al. "Observation of a new boson at a mass of 125 GeV with the CMS experiment at the LHC". In: *Phys. Lett.* B716 (2012), pp. 30–61. DOI: 10.1016/j.physletb.2012.08.021. arXiv: 1207.7235 [hep-ex].

[4] Georges Aad et al. "Observation of a new particle in the search for the Standard Model Higgs boson with the ATLAS detector at the LHC". In: *Phys. Lett.* B716 (2012), pp. 1–29. DOI: 10.1016/j.physletb.2012.08.020. arXiv: 1207.7214 [hep-ex].

[5] A. Andreassen, W. Frost, and M. D. Schwartz. "Scale Invariant Instantons and the Complete Lifetime of the Standard Model". In: *Phys. Rev.* D97.5 (2018), p. 056006. DOI: 10.1103/PhysRevD.97.056006. arXiv: 1707.08124 [hep-ph].

[6] Dario Buttazzo et al. "Investigating the near-criticality of the Higgs boson". In: *JHEP* 12 (2013), p. 089. DOI: 10.1007/JHEP12(2013)089. arXiv: 1307.3536 [hep-ph].

[7] Paolo Nason. "The Top Mass in Hadronic Collisions". In: 2017. arXiv: 1712.02796 [hep-ph]. URL: https://inspirehep.net/record/1642228/files/arXiv:1712.02796.pdf.

[8] M.P. Hobson, G.P. Efstathiou, and A.N. Lasenby. *General Relativity: An Introduction for Physicists*. Cambridge University Press, 2006. ISBN: 9781139447546. URL: https://books.google.fi/books?id=xma1QuTJphYC.

[9] Maxim Perelstein. "Introduction to Collider Physics". In: *Physics of the large and the small, TASI 09, proceedings of the Theoretical Advanced Study Institute in Elementary Particle Physics, Boulder, Colorado, USA, 1-26 June 2009*. 2011, pp. 421–486. DOI: 10.1142/9789814327183_0008. arXiv: 1002.0274 [hep-ph]. URL: http://inspirehep.net/record/844291/files/%20arXiv:1002.0274.pdf.

[10] A. Einstein. "Die Grundlage der allgemeinen Relativitätstheorie". In: *Annalen der Physik* Vierte Folge, Band 49.7 (1916).

[11] M. E. Peskin and D. V. Schroeder. *An Introduction to quantum field theory*. 1995. ISBN: 9780201503975, 0201503972. URL: http://www.slac.stanford.edu/spires/find/%20books/www?cl=QC174.45%3AP4.

[12] I. J. R. Aitchison and A. J. G. Hey. *Gauge theories in particle physics: A practical introduction. Vol. 1: From relativistic quantum mechanics to QED*. 2003. URL: http://www-spires.fnal.gov/spires/find/books/%20www?cl=QC793.3.F5A34::2012.

[13] Matthew D. Schwartz. *Quantum Field Theory and the Standard Model*. Cambridge University Press, 2014. ISBN: 1107034736, 9781107034730. URL: http://www.cambridge.org/us/academic/subjects/physics/theoretical-physics-and-mathematical-physics/quantum-field-theory-and-standard-model.

[14] MissMJ - Own work by uploader. PBS NOVA [1], Fermilab, Office of Science, United States Department of Energy, Particle Data Group, Public Domain. URL: https://commons.wikimedia.org/w/index.php?curid=4286964.

[15] URL: https://commons.wikimedia.org/wiki/File:Elementary_particle_interactions.svg#/media/File:Elementary_particle_interactions.svg.

[16] Roel Aaij et al. "Observation of $J/\psi p$ Resonances Consistent with Pentaquark States in $\Lambda_b^0 \to J/\psi K^- p$ Decays". In: *Phys. Rev. Lett.* 115 (2015), p. 072001. DOI: 10.1103/PhysRevLett.115.072001. arXiv: 1507.03414 [hep-ex].

[17] T. Aaltonen et al. "Observation of the Ω_b^- and Measurement of the Properties of the Ξ_b^- and Ω_b^-". In: *Phys. Rev.* D80 (2009), p. 072003. DOI: 10.1103/PhysRevD.80.072003. arXiv: 0905.3123 [hep-ex].

[18] C. S. Wu et al. "Experimental Test of Parity Conservation in Beta Decay". In: *Phys. Rev.* 105 (1957), pp. 1413–1414. DOI: 10.1103/PhysRev.105.1413.

[19] J. H. Christenson et al. "Evidence for the 2π Decay of the K_2^0 Meson". In: *Phys. Rev. Lett.* 13 (4 July 1964), pp. 138–140. DOI: 10.1103/PhysRevLett.13.138. URL: http://link.aps.org/doi/10.1103/PhysRevLett.13.138.

[20] S. Donnachie et al. "Pomeron physics and QCD". In: *Camb. Monogr. Part. Phys. Nucl. Phys. Cosmol.* 19 (2002), pp. 1–347.

[21] M. Tanabashi et al. "Review of Particle Physics". In: *Phys. Rev.* D98.3 (2018), p. 030001. DOI: 10.1103/PhysRevD.98.030001.

[22] F. Englert and R. Brout. "Broken symmetry and the mass of the gauge vector mesons". In: *Physical Review Letters* 13.9 (Aug. 1964).

[23] P. W. Higgs. "Broken symmetries, massless particles and gauge fields". In: *Physics Letters* 12.2 (Sept. 1964).

[24] A. Andreassen, W. Frost, and M. D. Schwartz. "Consistent Use of Effective Potentials". In: *Phys. Rev.* D91.1 (2015), p. 016009. DOI: 10.1103/PhysRevD.91.016009. arXiv: 1408.0287 [hep-ph].

[25] A. Andreassen, W. Frost, and M. D. Schwartz. "Consistent Use of the Standard Model Effective Potential". In: *Phys. Rev. Lett.* 113.24 (2014), p. 241801. DOI: 10.1103/PhysRevLett.113.241801. arXiv: 1408.0292 [hep-ph].

[26] Sidney Coleman and Erick Weinberg. "Radiative Corrections as the Origin of Spontaneous Symmetry Breaking". In: *Phys. Rev. D* 7 (6 Mar. 1973), pp. 1888–

1910. DOI: 10.1103/PhysRevD.7.1888. URL: https://link.aps.org/doi/10.1103/PhysRevD.7.1888.

[27] S. Alekhin, A. Djouadi, and S. Moch. "The top quark and Higgs boson masses and the stability of the electroweak vacuum". In: *Phys. Lett.* B716 (2012), pp. 214–219. DOI: 10.1016/j.physletb.2012.08.024. arXiv: 1207.0980 [hep-ph].

[28] André H. Hoang, Simon Plätzer, and Daniel Samitz. "On the Cutoff Dependence of the Quark Mass Parameter in Angular Ordered Parton Showers". In: *JHEP* 10 (2018), p. 200. DOI: 10.1007/JHEP10(2018)200. arXiv: 1807.06617 [hep-ph].

[29] T. Aaltonen et al. "Combination of the top-quark mass measurements from the Tevatron collider". In: *Phys. Rev. D* 86 (9 Nov. 2012), p. 092003. DOI: 10.1103/PhysRevD.86.092003. URL: https://link.aps.org/doi/10.1103/PhysRevD.86.092003.

[30] V. M. Abazov et al. "Precise measurement of the top-quark mass from lepton+jets events at D0". In: *Phys. Rev. D* 84 (3 Aug. 2011), p. 032004. DOI: 10.1103/PhysRevD.84.032004. URL: https://link.aps.org/doi/10.1103/PhysRevD.84.032004.

[31] B. Abbott et al. "Direct measurement of the top quark mass at D0". In: *Phys. Rev.* D58 (1998), p. 052001. DOI: 10.1103/PhysRevD.58.052001. arXiv: hep-ex/9801025 [hep-ex].

[32] V. M. et al. Abazov. "Precision measurement of the top-quark mass in lepton+jets final states". In: *Phys. Rev. D* 91 (11 June 2015), p. 112003. DOI: 10.1103/PhysRevD.91.112003. URL: https://link.aps.org/doi/10.1103/PhysRevD.91.112003.

[33] V.M. Abazov et al. "Determination of the pole and $\overline{\text{MS}}$ masses of the top quark from the $t\bar{t}$ cross section". In: *Physics Letters B* 703.4 (2011), pp. 422–427. ISSN: 0370-2693. DOI: https://doi.org/10.1016/j.physletb.2011.08.015. URL: http://www.sciencedirect.com/science/article/pii/S0370269311009373.

[34] V. M. et al. Abazov. "Measurement of the inclusive $t\bar{t}$ production cross section in $p\overline{p}$ collisions at $\sqrt{s} = 1.96$ TeV and determination of the top quark pole mass". In: *Phys. Rev. D* 94 (9 Nov. 2016), p. 092004. DOI: 10.1103/PhysRevD.94.092004. URL: https://link.aps.org/doi/10.1103/PhysRevD.94.092004.

[35] Albert M Sirunyan et al. "Measurement of $\mathrm{t\bar{t}}$ normalised multi-differential cross sections in pp collisions at $\sqrt{s} = 13$ TeV, and simultaneous determination of the strong coupling strength, top quark pole mass, and parton distribution functions". In: *Submitted to: Eur. Phys. J.* (2019). arXiv: 1904.05237 [hep-ex].

[36] Albert M Sirunyan et al. "Measurement of the top quark mass with lepton+jets final states using p p collisions at $\sqrt{s} = 13\,\text{TeV}$". In: *Eur. Phys. J.* C78.11 (2018), p. 891. DOI: 10.1140/epjc/s10052-018-6332-9. arXiv: 1805.01428 [hep-ex].

[37] Jan Kieseler, Katerina Lipka, and Sven-Olaf Moch. "Calibration of the Top-Quark Monte Carlo Mass". In: *Phys. Rev. Lett.* 116.16 (2016), p. 162001. DOI: 10.1103/PhysRevLett.116.162001. arXiv: 1511.00841 [hep-ph].

[38] Mathias Butenschoen et al. “Top Quark Mass Calibration for Monte Carlo Event Generators”. In: *Phys. Rev. Lett.* 117.23 (2016), p. 232001. DOI: 10.1103/PhysRevLett.117.232001. arXiv: 1608.01318 [hep-ph].

[39] *Measuremebt of the top quark mass in the $t\bar{t}$ → lepton+jets channel from $\sqrt{s}$=8 TeV ATLAS data*. Tech. rep. ATLAS-CONF-2017-071. Geneva: CERN, Sept. 2017. URL: http://cds.cern.ch/record/2285809.

[40] K. Augsten and Z. Ye. “Correction For the MC-Data Difference in the Jet Response at DØ for Run IIB”. In: *DØ note 6368* (2013).

[41] S. Atkins et al. “Correction For the MC-Data Difference in the Jet Response at DØ”. In: *DØ note 6143* (2011).

[42] John C. Collins, Davison E. Soper, and George F. Sterman. “Factorization of Hard Processes in QCD”. In: *Adv. Ser. Direct. High Energy Phys.* 5 (1989), pp. 1–91. DOI: 10.1142/9789814503266_0001. arXiv: hep-ph/0409313 [hep-ph].

[43] S. Alekhin et al. “HERAFitter”. In: *Eur. Phys. J.* C75.7 (2015), p. 304. DOI: 10.1140/epjc/s10052-015-3480-z. arXiv: 1410.4412 [hep-ph].

[44] David J. Gross and Frank Wilczek. “Ultraviolet Behavior of Non-Abelian Gauge Theories”. In: *Phys. Rev. Lett.* 30 (26 June 1973), pp. 1343–1346. DOI: 10.1103/PhysRevLett.30.1343. URL: https://link.aps.org/doi/10.1103/PhysRevLett.30.1343.

[45] Torbjörn Sjöstrand. “Colour reconnection and its effects on precise measurements at the LHC”. In: 2013. arXiv: 1310.8073 [hep-ph].

[46] T. Sjostrand, S. Mrenna, and P.Z. Skands. “PYTHIA 6.4 Physics and Manual”. In: *JHEP* 05 (2006), p. 026. DOI: 10.1088/1126-6708/2006/05/026. arXiv: hep-ph/0603175 [hep-ph].

[47] Bo Andersson, G. Gustafson, and Jim Samuelsson. “The Stochastic basis of the Lund model”. In: *QCD and high-energy hadronic interactions. Proceedings, Hadronic Session of the 28th Rencontres de Moriond, Moriond Particle Physics Meeting, Les Arcs, France, March 20-27, 1993*. 1993, pp. 559–572. URL: http://alice.cern.ch/format/showfull?sysnb=0170903.

[48] M. Bahr et al. “Herwig++ Physics and Manual”. In: *Eur. Phys. J.* C58 (2008), pp. 639–707. DOI: 10.1140/epjc/s10052-008-0798-9. arXiv: 0803.0883 [hep-ph].

[49] Johannes Bellm et al. “Herwig 7.0/Herwig++ 3.0 release note”. In: *Eur. Phys. J.* C76.4 (2016), p. 196. DOI: 10.1140/epjc/s10052-016-4018-8. arXiv: 1512.01178 [hep-ph].

[50] Hannu Siikonen. “Jet flavors: From the standard candles to the top quark mass”. G2 Pro gradu, diplomityö. 2016-04-05. URL: http://urn.fi/URN:NBN:fi:aalto-201604201842.

[51] *Schematic figure of the Tevatron accelerator complex*. URL: https://www-d0.fnal.gov/welcome/introduction.htm.

[52] V.M. Abazov et al. “The upgraded DØ detector”. In: *Nuclear Instruments and Methods in Physics Research Section A: Accelerators, Spectrometers, Detectors and Associated Equipment* 565.2 (2006), pp. 463–537. ISSN: 0168-9002. DOI: https:

//doi.org/10.1016/j.nima.2006.05.248. URL: http://www.sciencedirect.com/science/article/pii/S0168900206010357.

[53] S. Abachi et al. "The DØ detector". In: *Nuclear Instruments and Methods in Physics Research Section A: Accelerators, Spectrometers, Detectors and Associated Equipment* 338.2 (1994), pp. 185–253. ISSN: 0168-9002. DOI: https://doi.org/10.1016/0168-9002(94)91312-9. URL: http://www.sciencedirect.com/science/article/pii/0168900294913129.

[54] Gerald C. Blazey et al. "Run II jet physics". In: *QCD and weak boson physics in Run II. Proceedings, Batavia, USA, March 4-6, June 3-4, November 4-6, 1999.* 2000, pp. 47–77. arXiv: hep-ex/0005012 [hep-ex]. URL: http://lss.fnal.gov/cgi-bin/find_paper.pl?conf-00-092.

[55] V. M. Abazov et al. "Measurement of the inclusive jet cross section in $p\bar{p}$ collisions at $\sqrt{s} = 1.96$ TeV". In: *Phys. Rev.* D85 (2012), p. 052006. DOI: 10.1103/PhysRevD.85.052006. arXiv: 1110.3771 [hep-ex].

[56] V. M. Abazov et al. "Jet energy scale determination in the DØ experiment". In: *Nucl. Instrum. Meth.* A763 (2014), pp. 442–475. DOI: 10.1016/j.nima.2014.05.044. arXiv: 1312.6873 [hep-ex].

[57] Matteo Cacciari, Gavin P. Salam, and Gregory Soyez. "FastJet User Manual". In: *Eur. Phys. J.* C72 (2012), p. 1896. DOI: 10.1140/epjc/s10052-012-1896-2. arXiv: 1111.6097 [hep-ph].

[58] Gavin P. Salam. "Towards Jetography". In: *Eur. Phys. J.* C67 (2010), pp. 637–686. DOI: 10.1140/epjc/s10052-010-1314-6. arXiv: 0906.1833 [hep-ph].

[59] Andy Buckley et al. "LHAPDF6: parton density access in the LHC precision era". In: *Eur. Phys. J.* C75 (2015), p. 132. DOI: 10.1140/epjc/s10052-015-3318-8. arXiv: 1412.7420 [hep-ph].

[60] J. Pumplin et al. "New generation of parton distributions with uncertainties from global QCD analysis". In: *JHEP* 07 (2002), p. 012. DOI: 10.1088/1126-6708/2002/07/012. arXiv: hep-ph/0201195 [hep-ph].

[61] Rene Brun and Fons Rademakers. "ROOT - An Object Oriented Data Analysis Framework". In: *Proceedings AIHENP'96 Workshop, Lausanne.* Sept. 1996. URL: http://root.cern.ch/.

[62] T. Mäkelä and H. Siikonen. *Software for sample generation and JES analysis.* URL: https://github.com/makelat/D0_JES_studies.

[63] F. Pandolfi, D. del Re, and Voutilainen M. "Jet Response and Resolution Measurement with Photon+Jet Events". In: *CMS AN -2010/076* (2010).

[64] DØ Collaboration. "Jet Energy Scale Determination at DØ Run II (final p17 version)". In: *DØ note 5382* (2007).

[65] R. Brun et al. "GEANT Detector Description and Simulation Tool". In: (1994). DOI: 10.17181/CERN.MUHF.DMJ1.

[66] L. Landau. "On the energy loss of fast particles by ionization". In: *J. Phys.(USSR)* 8 (1944), pp. 201–205.

[67] Donald E. Groom. "Energy flow in a hadronic cascade: Application to hadron calorimetry". In: *Nuclear Instruments and Methods in Physics Research A* 572.2

(Mar. 2007), pp. 633–653. DOI: 10.1016/j.nima.2006.11.070. arXiv: physics/0605164 [physics.ins-det].

[68] Donald Eugene Groom. "A simplistic view of hadron calorimetry". In: *AIP Conf. Proc.* 896.1 (2007), pp. 137–149. DOI: 10.1063/1.2720464.

[69] C. Buttar et al. "Standard Model Handles and Candles Working Group: Tools and Jets Summary Report". In: *Physics at TeV colliders, La physique du TeV aux collisionneurs, Les Houches 2007 : 11-29 June 2007*. 2008, pp. 121–214. arXiv: 0803.0678 [hep-ph].

[70] The DØ collaboration. "Jet Energy Scale Determination at DØ Run II (final p17 version)". In: *DØ note 5382* (2007).

[71] Ankit Rohatgi. *WebPlotDigitizer*. Version 4.1. ankitrohatgi@hotmail.com, Jan. 2018. URL: https://automeris.io/WebPlotDigitizer.

[72] A.M. Sirunyan et al. "Particle-flow reconstruction and global event description with the CMS detector". In: *Journal of Instrumentation* 12.10 (Oct. 2017), P10003–P10003. DOI: 10.1088/1748-0221/12/10/p10003. URL: https://doi.org/10.1088%2F1748-0221%2F12%2F10%2Fp10003.

[73] F. James. "MINUIT Function Minimization and Error Analysis: Reference Manual Version 94.1". In: (1994).